Magneto-electrical transport through MBE-grown III-V semiconductor nanostructures: from zero- to one-dimensional type of transport

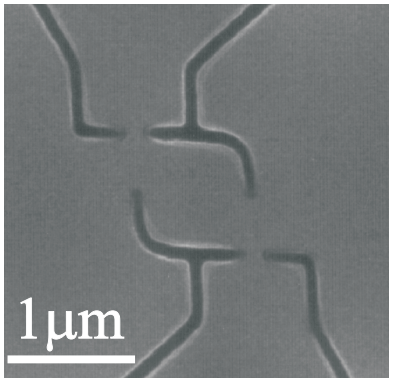

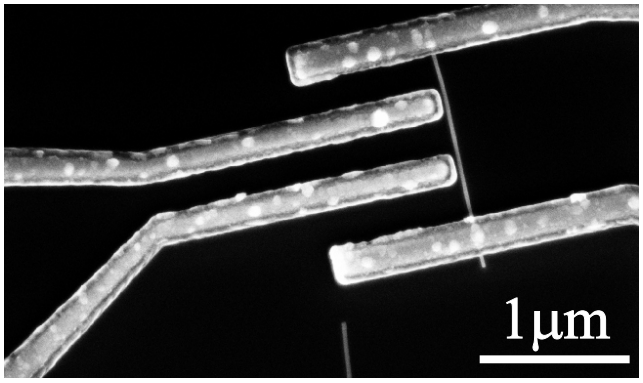

Eleonora Storace

Max-Planck-Institut für Festkörperforschung

Stuttgart, 2009

Magneto-electrical transport through MBE-grown III-V semiconductor nanostructures: from zero- to one-dimensional type of transport

Von der Fakultät Mathematik und Physik der Universität Stuttgart zur Erlangung der Würde eines Doktors der Naturwissenschaften (Dr. rer. nat.) genehmigte Abhandlung

Vorgelegt von

Eleonora Storace

aus Udine, Italien

Hauptberichter:	**Prof. Dr. Klaus von Klitzing**
Mitberichter:	**Prof. Dr. Heinz Schweizer**
Tag der Einreichung:	**20.05.2009**
Tag der mündlichen Prüfung:	**08.07.2009**

Max-Planck-Institut für Festkörperforschung
Stuttgart, 2009

Deutsche Zusammenfassung

Seit der Entwicklung des ersten Transistors 1947 bestand großes Interesse an der technologischen Entwicklung halbleitender Bauelemente und der Untersuchung ihrer physikalischen Eigenschaften. Ein sehr lebendiges Feld innerhalb dieses Forschungsgebietes konzentriert sich auf den elektrischen Transport durch niederdimensionale Strukturen, in denen die räumliche Einschränkung der Bewegungsfreiheit von Ladungsträgern zur Beobachtung einer Vielzahl von quantenmechanischen Phänomenen führt, die interessante Einsichten über die fundamentalen Eigenschaften der untersuchten niederdimensionalen Strukturen erlauben.
In der vorliegenden Arbeit betrachten wir Systeme, die, obwohl normalerweise unter anderen Gesichtspunkten untersucht, fundamentale Ähnlichkeiten in ihren Transporteigenschaften zeigen. Wir beginnen mit der Analyse nulldimensionaler Systeme (Quantenpunkte) und untersuchen, wie elektrischer Transport durch eine quasi-isolierte Insel mit lokalisierten Elektronen – dem Quantenpunkt – stattfinden kann. Durch genaues Einstellen der Tunnelkopplungsstärke zwischen dieser Insel und ihrer Umgebung werden wir dann zeigen, wie es möglich ist, von einem null- zu einem eindimensionalen System überzugehen. Danach wird der umgekehrte Weg untersucht: Ein eindimensionales System (gewachsener Nanodraht) wird elektrisch charakterisiert, der – wie sich zeigt – durch Unordnung in mehrere nulldimensionale Systeme zerfällt.
Die Arbeit ist daher in zwei Teile gegliedert:

I: Elektrischer Transport durch ein Quantenpunktsystem bei hohen Magnetfeldern

Ein Quantenpunkt (engl. 'Quantum Dot, QD') ist ein nulldimensionales System, in welchem Elektronen in alle räumlichen Richtungen eingesperrt sind, so dass quantenmechanische Effekte die auftretende Physik dominieren. Das erste Resultat der kleinen räumlichen Einschränkung ist die Diskretheit des Spektrums der Einteilchenenergien im Quantenpunkt. Da die Elektronen auf kleinem Raum eingeschlossen sind, wird außerdem die Elektron-Elektron-Wechselwirkung wichtig. Ein Quantenpunksystem besteht per Definition aus dem Quantenpunkt selbst, aus zwei Zuleitungen ('Source' und 'Drain'), an die der Quantenpunkt durch Tunnelbarrieren gekoppelt ist, und aus einer oder mehreren 'Gate'-Elektroden, die das elektrostatische Potential des Quantenpunktes kapazitiv beeinflussen. Der elektrische Transport durch das System wird hauptsächlich von der Coulombabstoßung zwischen Elektronen bestimmt und daher passieren Elektronen vorzugsweise eines nach dem ande-

ren das System, – ein Phänomen, das als Einzelelektronentunneln bekannt ist (engl. 'Single Electron Tunneling, SET') bekannt ist.

- In **Kapitel 1** wird der Herstellungsprozeß des in der vorliegenden Arbeit benutzten Quantenpunksystems erklärt und die hauptsächlichen Eigenschaften und Eigenheiten werden herausgestellt. Die Proben, basierend auf einer GaAs/AlGaAs-Heterostruktur, welche ein zweidimensionales Elektronensystem (2DES) enthält, wurden mittels Elektronenstrahllithographie und anschließendem Ätzens von M. Keller während seiner Doktorarbeit am Max-Planck-Institut für Festkörperforschung entwickelt [**?**]. Die Haupteigenschaft eines solchen Systems ist der hohe Grad, mit der im Experiment ein Großteil der Parameter, die den elektrischen Transport bestimmen, kontrolliert werden kann.

- Die grundlegenden Magnetotransporteigenschaften der Struktur werden in **Kapitel 2** diskutiert, mit besonderem Augenmerk auf die Unterscheidung zwischen Einzelelektronentunneln und korreliertem Elektronentunneln. Durch Anlegen von Spannungen an Gateelektroden kann die Anzahl der Elektronen auf der Insel kontrolliert werden, was zu einer Modulation des Stromes durch das System führt, – bekannt in der Literatur als Coulomb-Blockade-Oszillationen (CBO). Durch systematisches Verändern der am System angelegten Spannungen, sowie der Tunnelkopplung zwischen Zuleitungen und Quantenpunkt können mehrere Regime im Transport erforscht werden. Man erhält grundlegende Informationen über das Quantenpunksystem, wie z.B. die Einzelelektronen-Ladeenergie.
  Im letzten Schritt der Charakterisierung wird ein externes Magnetfeld an das System angelegt und die damit einhergehenden Veränderungen der internen Elektronenkonfiguration auf dem Quantenpunkt werden diskutiert. Das dem Quantenpunkt zugrundeliegende zweidimensionale System wird aufgeteilt in alternierende kompressible und inkompressible Bereiche, welche metallische bzw. isolierende Eigenschaften aufweisen, was zu einer 'Quantenpunkt-im-Quantenpunkt'-Struktur führt.

- In **Kapitel 3** wird bei konstantem Magnetfeld gezeigt, wie eine bemerkenswert hohe Variabilität in den elektronischen Eigenschaften des Quantenpunktsystems besteht. Die oben genannte 'Quantenpunkt-im-Quantenpunkt'-Struktur konnte durch Verändern der Tunnelkopplung zwischen Insel und Zuleitungen, sowie der Anzahl von kompressiblen und inkompressiblen Bereichen modifiziert werden. Hier wird gezeigt, wie man von einem lokalisierten, nulldimensionalen System zu einer Konfiguration mit einem direkten eindimensionalen Kanal zwischen

den Zuleitungen umschalten kann. Die lokale Elektronenspinpolarisation wird ebenfalls diskutiert.

Das Erreichte kann wie folgt zusammengefasst werden: In Abhängigkeit vom Magnetfeld konnten zwei unterschiedliche Landau-Level-Füllfaktoren (LL) im zugrundeliegenden 2DES eingestellt werden. Für $\nu_{\mathrm{2DES}} = 2$ umläuft ein kompressibler Rand die Zuleitungen und schließt ein inkompressibles Innere mit Füllfaktor 2 ein. Aufgrund elektrostatischer Verarmung ist die Elektronenkonzentration im Quantenpunkt vermutlich niedriger, so dass in dessen Zentrum $\nu < \nu_{\mathrm{2DES}}$ ist.
Wenn die Kopplung zwischen Zuleitungen und Insel durch Verändern der Gatespannungen erhöht wird, überlappen die äußeren kompressiblen Ränder der Zuleitungen und des Quantenpunktes: Transport findet im inkompressiblen Inneren statt, wo ein spinpolarisierter Strom fließt, getrieben von der elektrochemischen Potentialdifferenz zwischen den kompressiblen Rändern im Quantenpunktbereich, was zu einem Leitwert von beinahe e^2/h führt. Für $\nu_{\mathrm{2DES}} = 4$ wurde aus den Messungen auf ein inselförmiges metallisches Inneres im Quantenpunkt geschlossen, d. h. dort befindet sich ein kompressibler Bereich mit lokalem Füllfaktor $2 < \nu < 4$. Im Falle starker Tunnelkopplung wird ein Leitwert von $2e^2/h$ erreicht, die Anwesenheit des kompressiblen Quantenpunktinneren führt jedoch zur Beobachtung tiefer und scharfer Minima im Leitwert, welche wir der Rückstreuung von Elektronen über das kompressible Quantenpunktinnere von einem kompressiblen Rand zum anderen kompressiblen Rand mit entgegengesetzter Chiralität (beide kommen sich im Quantenpunktbereich sehr nahe) zuschreiben.

II: Magnetotransport in durch Molekularstrahlepitaxie gewachsenen III-V-Nanodrahtsystemen

Mit dem Ziel noch kleinere und kompaktere Strukturen zu erreichen, kombinieren wir im zweiten Teil der Arbeit die Vorteile von 'top-down'- und 'bottom-up'-Ansatz im Herstellungsprozess in einer einzigen Struktur: Halbleiter-III-As-Nanodrähte (engl. 'Nanowires, NW'), gewachsen mit Molekularstrahlepitaxie (engl. 'Molecular Beam Epitaxy, MBE'), werden mit Source- und Drain-Kontakten, sowie mit weiteren lokal elektrostatisch ankoppelnder Metallelektroden (Gates) versehen. Aufgrund der Flexibilität in der Kontrolle der Chemie von Nanodrähten werden diese höchstwahrscheinlich grundlegend für viele Arten von Nanostrukturen sein.

- In **Kapitel 4** wird die für unsere Drähte benutzte Dampf-Flüssigkeit-Festkörper-Wachstumstechnik (engl. 'Vapor-Liquid-Solid, VLS') allge-

mein diskutiert, die speziell von uns gemessenen Drähte werden vorgestellt und der Kontaktierungsprozess beschrieben. Zwei verschiedene NW-Systeme wurden untersucht: Indium-Arsenid- sowie Berylliumdotierte Gallium-Arsenid-NW-Systeme.

- Das erste System wird in **Kapitel 5** behandelt, speziell die magnetoelektrische Charakterisierung. Aufgrund seiner intrinsischen Eigenschaften ist InAs ein vielversprechender Kandidat für die Realisierung von beispielsweise spintronischen Bauteilen, basierend auf der aktiven Manipulation des Spin-Freiheitsgrades in Festkörpersystemen. Das Problem einer effizienteren Kontrolle des Systems wird diskutiert und verschiedene Lösungen werden vorgeschlagen und erörtert. Hier wird gezeigt, wie wir extrem kleine NW-Systeme definieren und charakterisieren konnten: Es wurde beobachtet, dass in 20 nm dicken Drähten der elektrische Transport bei tiefen Temperaturen von Coulomb-Blockade-Effekten dominiert wird. Bei hinreichend kleinem Abstand zwischen Source- und Drain-Elektrode (100 nm) verhalten sich die Nanodrähte wie einzelne Quantenpunkte mit Ladeenergien von 10 meV und vergleichbarem Einteilchen-Niveauabständen.

- Im letzten Kapitel werden Be-dotierte GaAs NW-Systeme vorgestellt und die Möglichkeit, solche Systeme als verdünnt magnetische Halbleiter zu benutzen, wird diskutiert. Die grundlegende Idee dieses Forschungsfeldes ist die Möglichkeit, magnetische Elemente in nichtmagnetische Halbleiter einzubringen. In einem solchen Material werden die magnetischen Eigenschaften von Spin-Austausch-Wechselwirkungen zwischen magnetischen Ionen und freien Löchern bestimmt. Magnetotransportmessungen als Funktion der Temperatur hoben unterschiedliche Transportregime hervor, die von uns als mit unterschiedlichen Streumechanismen zusammenhängend interpretiert wurden: Phononenstreuung für hohe T, Streuung an Unordnung für mittlere T sowie schwache Antilokalisierung für Temperaturen unter 60 K, welche von einem starken positiven Magnetowiderstand nahegelegt wird.

Die hier vorgestellten Arbeiten zeigen, dass prinzipiell InAs-NW-Systeme mit einer Vielzahl von rückseitigen und seitlichen Gates definiert werden können, was auf eine vollständige elektrostatische Kontrolle des Drahtes abzielt. Außerdem wurden Systeme mit Drähten kürzer als 100 nm und dünner als 20 nm charakterisiert, – unseres Wissens die kleinsten NW-Systeme, von denen über elektrische Charakterisierungsmessungen berichtet wurde. Aufgrund der durchgeführten magneto-elektrischen Charakterisierung erwiesen

sich MBE-gewachsene InAs-NW-Systeme als passende Kandidaten für weitere Entwicklung von Halbleitertransistoren und spintronischen Bauteilen. Angesichts des kleinen Durchmessers des Nanodrahtes hat jedoch die Anwesenheit von Unordnung im Nanodraht großen Einfluss auf den Transport durch den Nanodraht, was zu Streuung in der Verlässlichkeit der Bauteile führen würde. Auch wenn einerseits gezeigt wurde, dass alle benötigten Schritte zur Herstellung eines qualitativ hochwertigen und vollständig kontrollierbaren Bauteils machbar sind, so ist doch andererseits die Unregelmäßigkeit in der Qualität der Drähte noch ein offenes Problem. Schließlich wird auch Magnetotransport durch Beryllium-dotierte GaAs-NW-Systeme diskutiert. Verschiedene Fälle wurden betrachtet, abhängig von der Stärke der Be-Dotierung, von dem für das Wachstum der NW benutzten Metall (Au oder Mn), und von der Art der Kontakte (normale Metalle mit Cr/Au oder ferromagnetische Metalle mit Ni). Wir sahen, dass, je nach Temperatur, der Transport von Phononenstreuung, Unordnungsstreuung oder schwacher Antilokalisierung bestimmt werden kann. Obwohl gezeigt wurde, dass Mn-Ionen in der Tat im GaAs-NW verdünnt verteilt sind, müssen wir schlussfolgern, dass höchstwahrscheinlich ihre Konzentration nicht groß genug ist zur Bildung eines verdünnt magnetischen Halbleiters.

From the development of the first transistor in 1947, great interest has been directed towards the technological development of semiconducting devices and the investigation of their physical properties. A very vital field within this topic focuses on the electrical transport through low-dimensional structures, where the quantum confinement of charge carriers leads to the observation of a wide variety of phenomena that, in their turn, can give an interesting insight on the fundamental properties of the structures under examination.
In the present thesis, attention will be drawn on systems that, even if commonly studied from different points of view, present some fundamental similarities in their transport properties. We will start analyzing zero-dimensional systems, focusing on how electrons localized onto an island can take part in the transport through the whole system; by precisely tuning the tunnel coupling strength between this island and its surroundings, we will then show how it is possible to move from a zero- to a one-dimensional system. Afterwards, the inverse path will be studied: a one-dimensional system is electrically characterized, proving itself to split up due to disorder into several zero-dimensional structures.
The thesis is therefore structured in two Parts:

I: Electrical transport through a quantum dot system at high magnetic fields

A quantum dot (QD) is a zero-dimensional system, where the potential is confining electrons in all the spatial directions in such a way that quantum mechanical effects become predominant in the physics occurring in the system. The first result of the confinement is the discreteness of the single-particle energy spectrum inside the QD. Moreover, since the electrons are trapped in a small space, the electron-electron interaction becomes important. By definition, a QD system is composed by the QD itself, by a source and a drain lead to which the QD is coupled via tunnel barriers and by one or more gate electrodes to which the QD is capacitively coupled. The electrical transport through the system is mainly determined by the Coulomb repulsion and therefore the electrons can pass through predominantly via

"one-by-one" tunneling, a phenomenon known as Single-Electron-Tunneling (SET).

- In **Chapter 1** the fabrication process of the QD system used in the present work is explained, pointing out its main characteristics and peculiarities. Based on a GaAs/AlGaAs heterostructure containing a two-dimensional electron system (2DES), It is an in-plane etched structure, developed by M. Keller during his PhD work at the Max Planck Institute for Solid State Research [1]. The main property of such a device is the high degree of in-situ tunability for all the parameters that control the electrical transport through it.

- The basic magnetotransport properties of the device are then discussed in **Chapter 2**, highlighting the differences between the single-electron tunneling (SET) and the correlated tunneling. By applying a voltage to the gate electrodes, the number of electrons present on the island can be controlled, leading to a modulation of the current flowing through the system, known in literature as Coulomb Blockade Oscillations (CBOs). By systematically varying the bias voltage through the system and the coupling between leads and QD, several transport regimes can be explored, allowing access to fundamental information about the QD system, like, for example, its charging energy.
  In the last step of the characterization, a magnetic field is applied externally to the system and the modifications that it brings to the internal electron configuration of the the QD are discussed. The two-dimensional system at the basis of the QD system is divided into alternating metal-like and insulating-like regions (called, respectively, compressible and incompressible regions), leading to the formation of a "dot-in-dot" structure. An inner compressible region can form a dot coupled only capacitively to its surroundings, while transport occurs mainly through an outer compressible ring.

- In **Chapter 3**, while keeping constant the applied magnetic field, it is shown how it is possible to tune our system through a remarkably high range of different internal electron configurations. The "dot-in-dot" structure aforementioned could be modified acting on the coupling between leads and island and on the number of compressible and incompressible regions in the system. It is here demonstrated how to switch from a localized zero-dimensional system to a configuration where a direct one-dimensional channel is formed between the leads. The local spin polarization of the system is also discussed.

The achievements can be summarized in the following way: Depending on the applied magnetic field, two different Landau level (LL) filling factors for the 2DES at the basis of the QD system could be obtained. For $\nu_{2\mathrm{DES}} = 2$, a compressible border runs along the whole leads structure, encircling an incompressible bulk where the filling factor is equal to 2. Due to electrostatic depletion, electron concentration is presumingly lower in the dot region, i.e. we have in the dot center $\nu < \nu_{2\mathrm{DES}}$.
Whenever the coupling between leads and island is increased by tuning the voltages applied to the gates, the outer compressible borders of leads and dot overlap: transport takes place within the inner bulk region, where a spin-polarized current flows, leading to a conductance value of almost e^2/h. For $\nu_{2\mathrm{DES}} = 4$, the presence on the island of a compressible inner dot has been detected from the measurements, i.e. in the dot center we have a compressible region with a local filling factor $2 < \nu < 4$. In the strong coupling regime the conductance value of $2e^2/h$ is reached, however the presence of this compressible dot leads to the observation of deep and sharp minima in the differential conductance, that have been related by us to backscattering of charges between the compressible borders with opposite chirality running there close to each other.

II: Magnetotransport in Molecular Beam Epitaxy grown III-V nanowire systems

In the aim of reaching even smaller sized and more compact devices, in the second Part of this thesis we propose to combine in a single device the best of both the top-down and the bottom-up fabrication approaches: semiconductor III-As nanowires (NWs) grown via Molecular Beam Epitaxy (MBE) technique are processed adding source and drain contacts and several types of electrostatically coupled gates. The flexibility in tailoring the chemistry of NWs will most likely make them the building blocks of several kinds of nanosized devices.

- In **Chapter 4** the Vapor-Liquid-Solid (VLS) growth technique used to obtain our wires will be discussed in general and then the specific wires measured by us will be presented and their contacting process described. Two different NW systems have been studied: Indium Arsenide and Beryllium doped Gallium Arsenide NW systems.

- The first one is addressed in **Chapter 5**, focusing on its magneto-electrical characterization. Because of its intrinsic properties, InAs is a very promising candidate for the realization, for example, of spintronic devices, based on the active manipulation of the spin degree of freedom

in solid-state systems. The issue of a more efficient degree of tunability and control over the system is discussed and different solutions are proposed and explored. It is here shown how we succeeded in defining and characterizing extremely small NW systems: We observed that in 20-nm thick wires low-temperature electron transport is dominated by Coulomb Blockade effect. For sufficiently small separation between the source and the drain electrodes (100 nm), the nanowires behave as single quantum dots with typical charging energies of 10 meV and comparable level spacing.

- In the last Chapter, Be-doped GaAs NW systems are presented, discussing the feasibility of using such devices in the frame of dilute magnetic semiconductor technologies. The idea at the basis of this research field is the possibility of introducing magnetic elements into non magnetic semiconductors. In such a material, the magnetic properties are driven by the spin-exchange interactions between the magnetic ions and the free holes. Magnetotransport measurements as a function of temperature highlighted several transport regimes, interpreted by us as related to different scattering mechanisms: phonon scattering for high T, impurity scattering for intermediated T, and weak anti-localization for temperatures below 60 K, as indicated by a pronounced positive magnetoresistance.

The work here presented proved that InAs NW systems can in principle be defined adding a large variety of back and lateral gates, aiming towards a full tunability of the electrostatics of the wires. Further, systems with wire channels shorter than 100 nm and thinner than 20 nm have also been obtained and characterized, to our knowledge the smallest NW system of which measurements have been reported. From the magnetoelectrical characterization carried out by us, MBE grown InAs NW systems proved themselves to be suitable candidates for further development of semiconductor transistors and of spintronic devices. Given the small diameter of the NW, though, the presence of an even small imperfection could have a strong impact on the overall transport through the wire system, leading to spread in the reliability of the devices. If, on one side, all the key ingredients for fabricating a high quality and fully tunable device have been demonstrated to be feasible, on the other side, the inconsistency of the performances of the wires is still an open issue.
Finally, magnetotransport through Beryllium doped Gallium Arsenide NW systems is also discussed. Different cases have been considered, depending on the level of Be doping, on the metal used to grow the NWs (either Au or Mn)

and on the type of contacts (normal metals, with Cr/Au, or ferromagnetic metals, with Ni). We could see that, depending on the temperature range, the transport can be dominated by phonon scattering, impurity scattering or weak anti-localization. Even if it has been demonstrated that Mn ions are indeed present diluted along the GaAs NW, we have to conclude that, most likely, their concentration is not high enough to lead to the formation of a diluted magnetic semiconductor.

Contents

Symbols **ix**

I Electrical transport through a QD system at high magnetic fields **1**

1 Introduction **3**
- 1.1 Quantum dot systems . . . 3
- 1.2 Quantum dot system formed from a two-dimensional electron system . . . 5
  - 1.2.1 Some examples for defining quantum dot systems . . . 5
  - 1.2.2 The base: a two-dimensional electron system in a GaAs/AlGaAs heterostructure . . . 8
  - 1.2.3 Forming the quantum dot system . . . 11
  - 1.2.4 Constrains from the sample design to the measurements conditions . . . 12

2 Magnetotransport through the QD system **15**
- 2.1 Tuning the tunnel barriers . . . 16
- 2.2 Coulomb Blockade Oscillations: Electrostatic model . . . 16
- 2.3 Coulomb Blockade Oscillations in the $V_{g1} - V_{g2}$ plane . . . 21
- 2.4 Conductance as a function of the source-drain and the gate voltages . . . 26
- 2.5 Features indicating the presence of the quantum dot . . . 28
- 2.6 Internal electronic structure of the QD for $B \neq 0$ . . . 40

3 Magnetotransport from weak to strong coupling **49**
- 3.1 The filling factor ν_{2DES} of the 2DES forming the QD system . 49
- 3.2 Antidot quantum systems . . . 51
- 3.3 Coulomb Blockade Oscillations at filling factor $\nu_{2DES} = 2$ . . . 54
- 3.4 Coulomb Blockade Oscillations at filling factor $\nu_{2DES} = 4$ . . . 56

3.5 Conclusion 66

II Magnetotransport in MBE-grown III-V NWs 69

4 Preparation of nanowire systems 71
4.1 The growth of nanowires: the vapor-liquid-solid growth method 71
4.2 Contacting the nanowire systems 77

5 Indium Arsenide nanowire systems 81
5.1 Motivation 81
5.2 Magneto-electrical characterization of a typical NW sample . . 82
5.2.1 Statistics of the wire resistance versus the design parameters 82
5.2.2 Magnetotransport at base temperature 85
5.3 Increasing tunability of the NW system 91
5.4 Scaling down the geometry of the NW systems 94
5.5 Conclusion and Outlook 97

6 Beryllium doped Gallium Arsenide nanowire systems 101
6.1 Motivation 101
6.2 Sample preparation and measurement setup 103
6.3 Magnetotransport measurements 105
6.3.1 Low Beryllium doping level 105
6.3.2 High Beryllium doping level 106
6.4 Conclusion 112

Appendices 117

A Experimental Setup 119

B Additional measurements of charge stability diagrams on the quantum dot system 123

C Contacting process for the nanowire systems 127

D Additional measurements on Au-GaAs nanowire systems 131

Abbreviations and symbols

Abbreviations

2DES	Two-Dimensional Electron System
b.e.p.	beam-equivalent pressure
CBOs	Coulomb Blockade Oscillations
DMS	Diluted Magnetic Semiconductor
EBL	Electron Beam Lithography
MBE	Molecular Beam Epitaxy
PMMA	Polymethylmetacrylat
QD	Quantum Dot
QHE	Quantum Hall Effect
QPC	Quantum Point Contact
SEM	Scanning Electron Microscope
SET	Single-Electron Tunneling
HRTEM	High Resolution Transmission Electron Microscope
UHV	Ultra High Vacuum

Symbols

B	Magnetic field
$C_i, \quad i = \{\mathrm{S,D,G}\}$	The capacitance of i^{th} electrode to the island
C_Σ	Total capacitance between the island and the rest of the system
ε_F	Fermi energy
ε_i	Single particle energies in a quantum dot
ϵ	dielectric constant
E	Electric field
$E_\mathrm{C} = e^2/2C_\Sigma$	Charging energy
g	Landé g-factor
G	Conductance
I	Current
k_B	Boltzmann constant
l	Angular quantum number
λ_F	Fermi wavelength
m^*_eff	Effective mass
μ	Electron mobility
μ^ch	Chemical potential
μ^elch	Electrochemical potential

ν	Filling factor
ν_{2DES}	Filling factor of the 2DES
R_{2t}	Two-terminal resistance
R_{4t}	Four-terminal resistance
ρ_{sheet}	Electron sheet density
V_{sd}	Source - drain voltage
V_{bg}	Back-gate voltage
$V_{\mathrm{g}i}$	Voltage applied to the i-th gate

Physical constants

e	Elementary charge
$-e$	Electron charge
ϵ_0	Dielectric constant of vacuum
h	Planck constant
k_{B}	Boltzmann constant
m_{e}	Mass of electron
μ_{B}	Bohr magneton
Φ_0	Magnetic flux quantum

Part I

Electrical transport through a QD system at high magnetic fields

Chapter 1

Introduction

The quantum confinement of charge carriers, under different degrees of freedom, manifests itself through a variety of specific and interesting phenomena. In electrical transport, the measurement of these phenomena is a valuable tool which can be used to identify and quantify various transport mechanisms. Generally, a mixture of different phenomena in one sample can be observed simultaneously due to the sample geometry, etching profile or gating method etc.. By carefully designing the sample and controlling the measurement parameters, complex two-, one- and zero-dimensional systems can be characterized and subsequently tuned to conditions where novel behavior is observed. This Chapter defines the quantum dot systems and explains how they can be fabricated using a two-dimensional-electron-system. A review of the different approaches to the device design discussed in literature is given, before some design limitations are explained.

1.1 Quantum dot systems

Let us introduce here the Fermi wavelength $\lambda_F = \frac{h}{\sqrt{2m^*_{\text{eff}}\varepsilon_F}}$ of a Fermi gas in a conductor; it is the deBroglie wavelength for an electron at the Fermi level with kinetic energy ε_F and effective mass m^*_{eff} determined by the material in

which it propagates. When the size of the bulk material becomes comparable with λ_F, the spatial confinement affects the Fermi gas system and quantum mechanical effects also become predominant in the physics occurring in the system.
Let us consider a system where the bulk is reduced in one of its spatial dimension, obtaining a two-dimensional system (i.e. a **quantum well**). In this case the most startling result was the observation of the Quantum Hall Effect (QHE) in 1980, that takes place when a high magnetic field is applied perpendicularly to the 2DES at a temperature of a few Kelvin. Following a classical treatment, the Drude formula would predict a linear behavior of the Hall resistance, R_H, as a function of the magnetic field. However, a step-like behavior was measured, that could be explained only taking into account quantization effect in the model. Moreover, the behavior of R_H was shown to be completely independent by any material geometry and to be related only to fundamental physical constants [2, 3].
Further reduction of the dimensionality of the system allows us to investigate one-dimensional systems (i.e. **quantum wires**). In the same way as the previous case, it is also here impossible to explain the measured transport characteristic simply considering classical effects. By including quantum mechanical effects in the theory, one can in fact see that, for example, the conductance is quantized in $\frac{2e^2}{h}$ times the number of 'wave modes' (1D subbands) of the propagating electrons.
Finally, one can consider a zero-dimensional system, also known as a **quantum dot (QD)**, where the confinement is in all the spatial directions. The typical size of such a system is on the order of λ_F (in the case of GaAs, for example, this means a few hundred nanometers), leading to a strong influence of quantum mechanics. The first result of this confinement is the discreteness of the energy spectrum. Moreover, inside a QD, dozens of electrons are trapped so closely with respect of each other that, adding an electron to the system, the electron-electron interaction is no longer negligible. For this reason, the transport through a QD is mainly determined by the Coulomb repulsion. The electrons can then pass through the system only via 'one-by-one' tunnelling. This phenomenon, known as single-electron-tunnelling, is strong evidence of the quantization of the charge and it will be further analyzed and discussed in the following chapters.

To do transport, one needs not only the QD but also the leads, like in the sketch shown in Fig. 1.1. The whole system, denoted as QD system, is then composed of

- the QD itself,

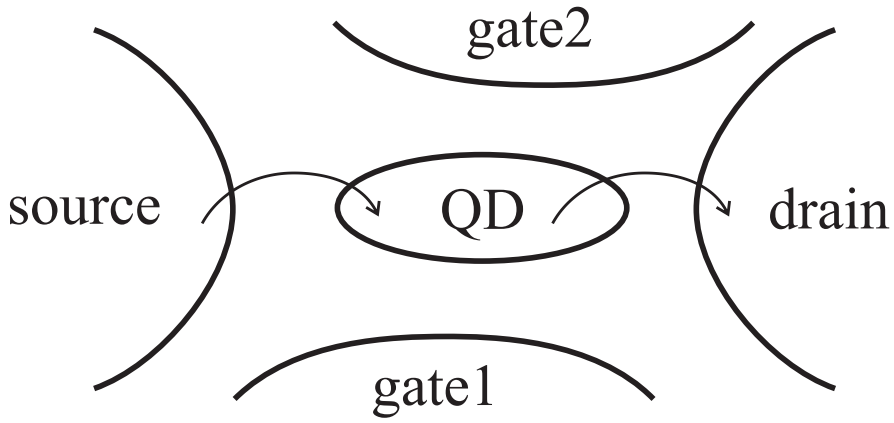

Figure 1.1: Sketch of a quantum dot system: The quantum dot is weakly tunnel-coupled to the source and drain leads and capacitively coupled to the gate electrodes. The electron exchange takes place via the tunnel barriers and the gate electrodes are used in order to tune the electrostatic potential of the quantum dot.

- a source and a drain lead to which the QD is coupled via tunnel barriers, and
- one or more gate electrodes to which the QD is capacitively coupled.

1.2 Quantum dot system formed from a two-dimensional electron system

1.2.1 Some examples for defining quantum dot systems

There are different ways to define QDs system for electrical transport measurements. Examples are the following:

- III-V semiconductor materials, which are grown layer by layer to a heterostructure containing a two-dimensional electron system (2DES) where the motion of the charges is completely restricted to a plane, are further structured by using conventional semiconductor processing technologies, like electron beam and optical lithography, etching and metallization [1], [4]. This is denoted as top-down approach.
- A bottom-up approach represents the self-formation of QDs during epitaxial growth of lattice-mismatched semiconductor materials [5].

- Another challenging approach is by contacting a single molecule, for instance a single carbon nanotube, with metal electrodes [6].

In the work presented in this Part of the thesis, the first kind of approach was chosen because of its wide variability in tuning parameters.
Starting from a III-V semiconductor heterostructure, in the last decade there has been used mainly two different kind of QD systems, which one can distinguish by the way in which the transport occurs, either perpendicular or parallel to the plane of the layers of the heterostructure.

Vertical and lateral quantum dot systems

A vertical dot system [7] is based on a heterostructure with, for example, the following layer sequence: doped-GaAs, $Al_{1-x}Ga_xAs$, $In_{1-x}Ga_xAs$, $Al_{1-x}Ga_xAs$ and doped-GaAs. Due to the difference in the conduction band minimum between the two materials, a potential landscape is found for the electrons as depicted in Fig. 1.2b. The highly doped GaAs layers are separated by AlGaAs layers, acting as thin insulators. Since the AlGaAs layers are thin, electrons can tunnel through them, entering or leaving the InGaAs layer. As shown in Fig. 1.2a, etching the heterostructure, a pillar remains, which is then metallized forming the side-gate and the source and drain leads. Acting on the gate, the dot inside the pillar can be reduced in size until only really few electrons ($\lesssim 10$) remain inside. Since the dot has the shape of a circular disk, the vertical structure has a high degree of symmetry; moreover, the confining potential is parabolic and it screens the electron-electron interaction. This fact allows the analysis of atomic-like properties like shell structure and Hund's rules [7].

A lateral dot system is formed by dividing the 2DES, present either at the interface of a GaAs/AlGaAs heterojunction or in a quantum well, into different regions that act as source, drain and gates electrodes. For dividing a 2DES there are two different methods:

- As can be seen in Fig. 1.2c, metal gate electrodes are deposited on the surface of the heterostructure. Since the 2DES is close to the surface, by applying a negative voltage to the gates, the electrons below the gates are depleted, isolating the different regions. This technique is denoted as split-gate technique.

- In Fig. 1.2d, the 2DES is instead divided by etching grooves into the heterostructure. Due to surface charges, along each groove an electrostatic depletion occurs, pushing the electron system further away. Such

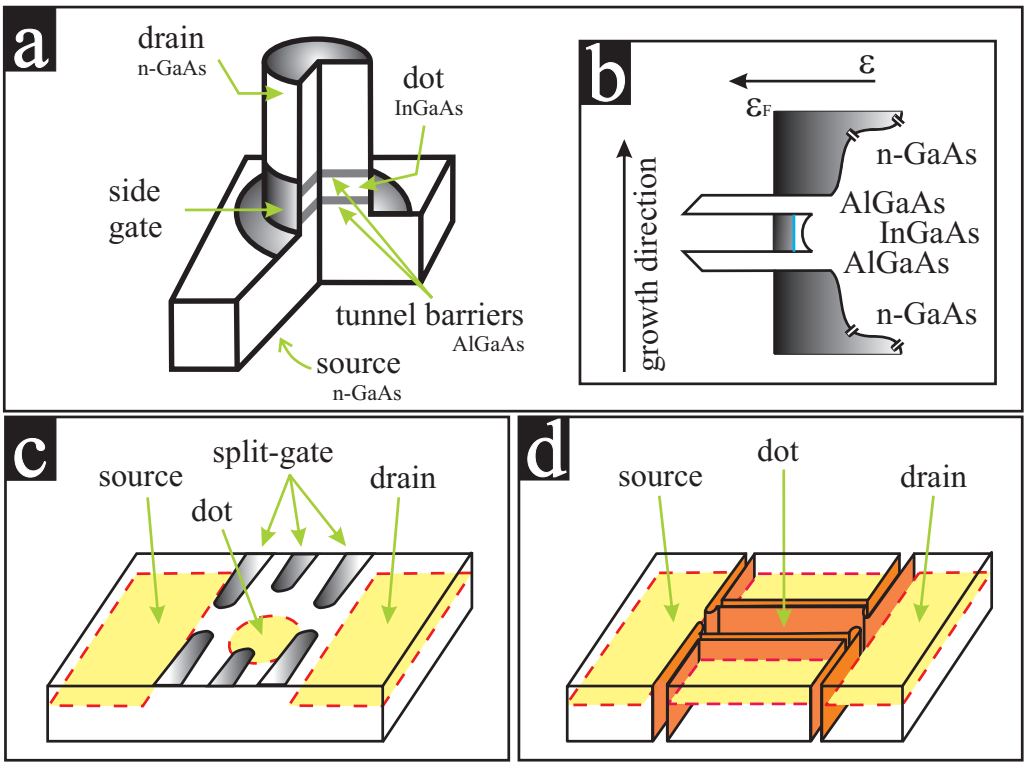

Figure 1.2: Based on a III-V semiconductor heterostructure there are two common approaches to define a QD system: vertical quantum dot system, where the transport takes place perpendicular to the layers (a), with an energy diagram like the one sketched in (b), and lateral quantum dot systems, where instead the transport is in a parallel plane of the layers. This last kind of system can be a split-gate (c) or an in-plane gate structure (d).

an arrangement is denoted as in-plane gate structure because now parts of the 2DES can be used as gates.

The main difference between vertical and lateral QD system is how the tunnel barriers between the QD and its leads are formed. In the first case they are defined by the grown layers, fixed with high barrier energy and short barrier length. In contrast, in the second structure they are formed by electrostatic depletion, that can make them usually in-situ tunable; however, in this case the barrier energy is small and the barrier length is large. Lateral QD systems contain from usually few dozens up to hundreds of electrons. However, in special designed structures, single-electron charging have been demonstrated showing that only few electrons (even only one) were confined in such lateral QD [8].

The sample used in the present thesis is based on the in-plane gate technique; it was defined through reactive ion etching by Matthias Keller during his PhD work [1]. In Fig. 1.3b a Scanning Electron Microscope image of the QD system is shown. As one can see, the pattern of the etched grooves defines the different parts of the system: source, drain, QD and two additional lateral gates. The tunnel barriers are defined by electrostatic depletion and can be tuned acting on gate 1 and 2 (Fig. 1.3c).

In the following sections some ideas and details about making this kind of sample are given.

1.2.2 The base: a two-dimensional electron system in a GaAs/AlGaAs heterostructure

The sample is based on a modulation-doped heterostructure containing a 2DES at the interface of a GaAs/$Al_{0.33}Ga_{0.67}As$ junction.

Modulation-doped heterojunction

A heterojunction is defined as an interface between two different materials; in the present case the materials considered are GaAs and AlGaAs. They have been chosen due to the following reasons:

- Because of their comparable lattice constants there is almost no lattice mismatch between these crystals, i.e. a pseudomorphic interface with no or just small stress is obtained.

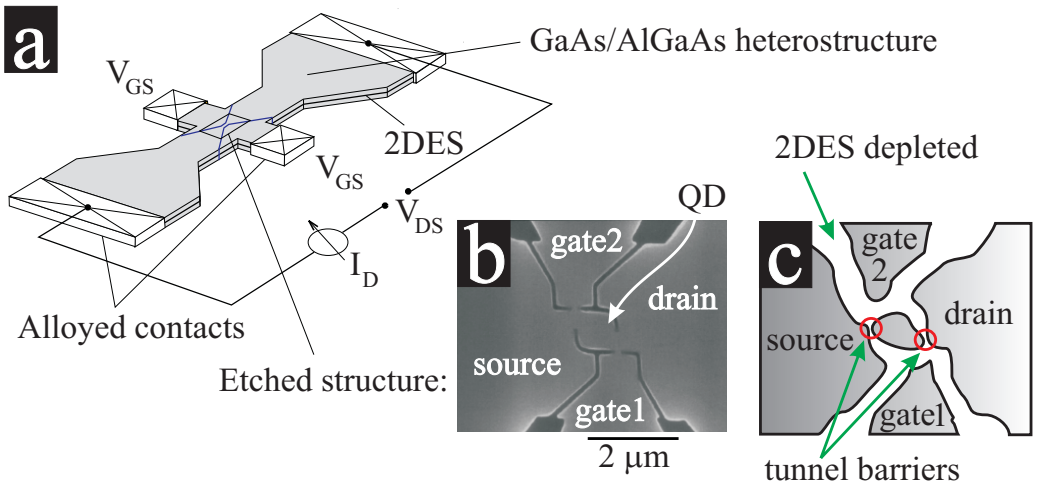

Figure 1.3: The QD system used in our measurements. (a) A sketch of the Hall bar highlighting the regions of the alloyed metal contacting the 2DES. (b) SEM-image of the system showing the etched grooves. (c) Electrostatic depletion around the etched grooves dividing the 2DES into the diverse regions. The tunnel barriers are formed at the marked constrictions.

- Electrons in the conduction band of GaAs possess a small effective mass: $m^*_{\mathrm{eff}}(\mathrm{GaAs}) = 0.067 m_0$, where m_0 is the free electron mass. The Fermi wavelength is given by

$$\lambda_{\mathrm{F}} = \frac{h}{\sqrt{2 m^*_{\mathrm{eff}} \varepsilon_{\mathrm{F}}}} . \tag{1.1}$$

  Since a typical ε_{F} is about 10 meV, λ_{F} is about 50 nm. To define a QD, the electrons have to be confined in all the spatial directions to this order.

The technique commonly used to define a heterostructure is Molecular Beam Epitaxy (MBE). Using this technique it is possible to change the composition of the crystal layer by layer, achieving atomic precision: the growth is epitaxial because the grown layers follows the crystallographic structure of the surface.

The complete layer sequence of the heterostructure is shown on the left side of Fig. 1.4. In the following the attention will be focused only on the active region directly involved in the formation of the 2DES. For this region

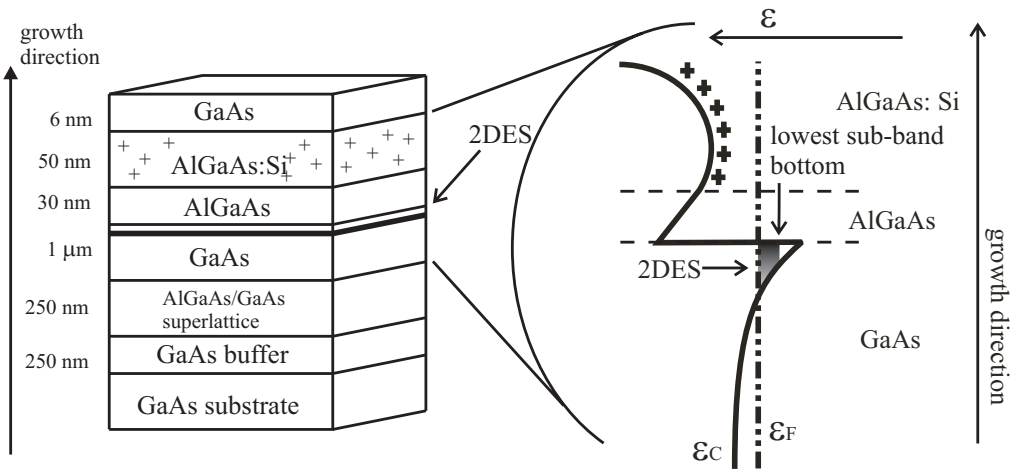

Figure 1.4: On the left side: Layer sequence of the modulation-doped GaAs/$Al_{0.33}Ga_{0.67}As$ heterostructure used in the experiments; please note that the layers thickness are not shown to scale. The thickness of the 2DES is about 10 nm. On the right side: Sketch of the energy position of the conduction band minimum ε_C through the layers. The Fermi level is denoted as ε_F. The plus signs indicate the energetic position of the holes left behind by the electrons accumulated in the 2DES.

a sketch of the conduction band energy bottom as a function of the growth direction is shown in the right side of Fig. 1.4.

When GaAs and AlGaAs are put together, an offset in the conduction band bottom is formed. Doping AlGaAs with Si as donors, electrons from the donors find energetically favorable levels in the GaAs conduction band. However, since they are still attracted by the positive charge of the ionized Si donors, they accumulate close to the GaAs/AlGaAs interface. As the result, the electrons feel a triangular shaped confining potential perpendicular to the layers' planes. Since the confining potential is so strong, the electrons are restricted to a thickness of a few tens of nanometers, which is comparable to the Fermi wavelength of the electron system. Therefore the eigenvalues of this confined electrons can be expressed as

$$\varepsilon(\vec{k}) = \varepsilon_{z,i} + \frac{(\hbar\vec{k_{||}})^2}{2m^*_{\text{eff}}}\,, \tag{1.2}$$

where $\varepsilon_{z,i}$ with $i = \{0, 1, 2, ...\}$ are the eigenvalues due to the triangular-like potential and the second term comes from the fact that the electrons are still free to move in the plane parallel to the interface ($\vec{k_{||}}$ is the component

of the wave vector $\vec{k}$ parallel to the interfaces). When the Fermi level lies between $\varepsilon_{z,0}$ and $\varepsilon_{z,1}$, a 2DES is obtained.

Contacting the two-dimensional electron system

Afterwards the heterostructure is shaped to a Hall bar mesa using optical lithography and wet etching. A sketch of the contacted structure is given in Fig. 1.3a. The main steps of the process are the following:

- Optical lithography is used to define a photoresist pattern on the surface of the heterostructure; certain areas are protected, others remain uncovered.

- The wet etching technique is used in order to etch the uncovered area: a solution of deionized H_2O, H_2O_2 (30%) and H_2SO_4 (96%) with a volume proportion of 1000:8:1 is attaching the uncovered surface, chemical reactions take place at the surface and the final products are transported away from the surface.

- Finally the leads are contacted: metal pads of gold/germanium/nickel were deposited on the selected parts of the surface; after heating the sample, the metal melts, the underlying surface is dissolved and an alloy is formed, contacting the metal to the 2DES.

A more detailed description of the preparation procedure can be found in Matthias Keller PhD thesis [1].
Having contacted the 2DES, it can be characterized by magneto-resistance measurements [9]. One can then obtain the electron sheet density ρ_{sheet} and the electron mobility μ_e. In this case, at the temperature of 4.2 Kelvin, the parameters are $\rho_{\text{sheet}} = 2.3 \times 10^{15}\,\text{m}^{-2}$ and $\mu_e = 86\,\text{m}^2/\text{Vs}$.

1.2.3 Forming the quantum dot system

A further dimensional reduction in order to obtain the 0D system has to follow. From the previous discussion, it requires to confine the electrons laterally in a region of the size of $\lambda_{\text{F}} \approx 50$ nm. This is achievable by using Electron Beam Lithography.
This lithographic process is divided in different steps. At first the sample is spin-coated by a PMMA resist; afterwards with an electron beam it is possible to write a certain pattern into the resist. After having removed the exposed resist, the uncovered surface of the sample is subjected to reactive

ion etching. This is a kind of dry etching, where the surface is bombarded with ions, that, through mechanical and chemical reactions, take away part of the surface of the sample. The main characteristic of the ion etching is that the ion beam is not isotropic, therefore for a small window one can etch rather deep, giving as result a sharp definition of the borders. Since the etch depth goes slightly below the 2DES, finally the etched grooves are dividing the 2DES and the QD system is formed.

1.2.4 Constrains from the sample design to the measurements conditions

Knowing the spatial dimensions and the main parameters of our sample, we can now look at the requirements for being able to observe single-electron charging effects.

Temperature

Opening the tunnel barriers between source and drain, charges will move through the QD system. Since the QD forms a capacitor with respect to the electrodes, a charging energy $E_C = \dfrac{e^2}{2C_\Sigma}$, where C_Σ is the total capacitance of the island, is needed to move the charge in or out of the QD. This consideration gives a first order of magnitude for the temperature that has to be used in the experiments: The thermal energy in fact should not exceed the charging energy,

$$\frac{e^2}{2C_\Sigma} \gg k_\mathrm{B}T\,. \tag{1.3}$$

To satisfy this relation, one can tune either the capacitance or the temperature. At first, since the capacitance of the island is proportional to its spatial extension ($C = 8\epsilon_0\epsilon R_0$, where the QD is approximated as a flat disk with radius R_0 and counter electrodes at infinity), the charging energy will be inverse proportional to the size of the QD. This means that decreasing the size of the dot one can observe charging effects even at quite high temperature. In the present situation, the dimension of the sample are already defined, implying that one can only reduce the temperature. In the case of the GaAs (dielectric constant $\epsilon = 13.6$) in a sample like ours with a diameter of about 400 nm, the charging energy is about 0.42 meV. Therefore charge-quantization effects can be then seen at a temperature much below 4 Kelvin; these values are easily reached in a ^{3}He $-^4$He-dilution-refrigerator.

Current

An other constrain that has to be taken into account is the finite lifetime τ of an additional electron charge in the QD. In fact, due to the Heisenberg uncertain relation, the energy E_C attributed to the charge state is uncertain to $\Delta\varepsilon \approx h/\tau$. This brings us to the requirement that the mean lifetime of the additional electron charge has to be larger than

$$\tau \gg \frac{h}{2E_C}\,. \tag{1.4}$$

In order to satisfy this condition, a weak tunnel coupling between dot and leads is needed. The measurable current will be then in the order of

$$I < \frac{e}{\tau} \ll E_C \frac{2e}{h}\,. \tag{1.5}$$

For $E_C \approx 0.4$ meV, this relation implies a current level of less than the order of 0.3 nA.

In conclusion:

These conditions and requirements have of course to be taken into account for our experimental set-up:
The experiments presented here were conducted in a $^3\mathrm{He} - {}^4\mathrm{He}$ dilution refrigerator with a base temperature below 20 mK (an Oxford Kelvinox$^{\mathrm{TLM}}$ 400). The differential conductance is measured by a two-terminal lock-in technique (EG&G Princeton Applied Research, model 5210) by applying an ac modulation of $1\mu\mathrm{V_{p-p}}$ at a frequency of 11.5 Hz, superimposed to the dc bias voltage V_{sd} (for more experimental details, see Appendix A).

Chapter 2

Magnetotransport properties of the quantum dot system

Referring to measurements taken for characterizing the sample, in this chapter the basic magnetotransport properties of the QD system are illustrated. The main property is the quantization of the charge inside the dot due to the single-electron charging energy. It is pointed out how this affects the electron tunneling through the system.
In the first part, electrical transport without an applied magnetic field is described, considering two different regimes:

- Tunneling of single charges, characterized by Coulomb Blockade, when no current can flow through the quantum dot, and Single-Electron-Tunneling, when an electron from the leads can move through the dot.

- Correlated tunneling, where electron transport from source to drain involves many electrons simultaneously (virtual intermediate charge state of the quantum dot).

In the second part then, it is described how the presence of an externally applied magnetic field affects the internal electronic configuration of the island and, in its turn, the whole transport through the system.

2.1 Tuning the tunnel barriers

Applying a voltage to the gates, the size of the electrostatic depletion generated at the level of the 2DES can be varied, modifying then the transparency of the tunnel barriers. In order to allow electrons to enter and to leave the QD, both barriers have to be thin and energetically shallow enough to make tunneling through them possible.
As shown in Fig. 2.1, four different regions can be identified in the parameter space of the two voltages controlling the tunnel barriers. Along the source-gate1 voltage (V_{g1}) axis the plane is divided in two half-planes by a borderline: on one side the tunnel barrier depending on gate1 is open, on the other side it is closed. The same behavior is sketched for the source-gate2 voltage (V_{g2}) axis controlling the other barrier. In the region in which the two half-planes corresponding to open barriers are overlapping, transport between source and drain can be detected. In the figure the area around the crossing point of the borderlines is highlighted; in this region the barriers are not yet fully opened and therefore, between source and drain, a dot is found quasi-isolated by the tunnel barriers. Electrons can tunnel from the source to the drain only one-by-one and the charge inside the dot is quantized. As described in the following, indeed, in this region of the $V_{\mathrm{g1}} - V_{\mathrm{g2}}$ plane single-electron tunneling is found.

2.2 Coulomb Blockade Oscillations: Electrostatic model

In Fig. 2.2 the conductance is shown as a function of the voltages applied to the two lateral gates, describing the line drawn in the insert. The dc bias voltage V_{sd} at the sample is approximately zero. To measure the conductance, a modulation amplitude of $V^{\mathrm{ac}} = 1\,\mu\mathrm{V}$ is applied; since, at $T \simeq 30$ mK, $eV^{\mathrm{ac}} < k_{\mathrm{B}}T$, a linear transport regime is here considered.
As one can see in the figure, the transport is characterized by a series of peaks alternated by zero-conductance regions, a phenomenon known as Coulomb-Blockade Oscillations (CBO). This behavior can be understood in a simple electrostatic model.

Electrostatic model

Let us consider a system composed of

- a metal island, i.e. a conductor completely surrounded by an insulator,

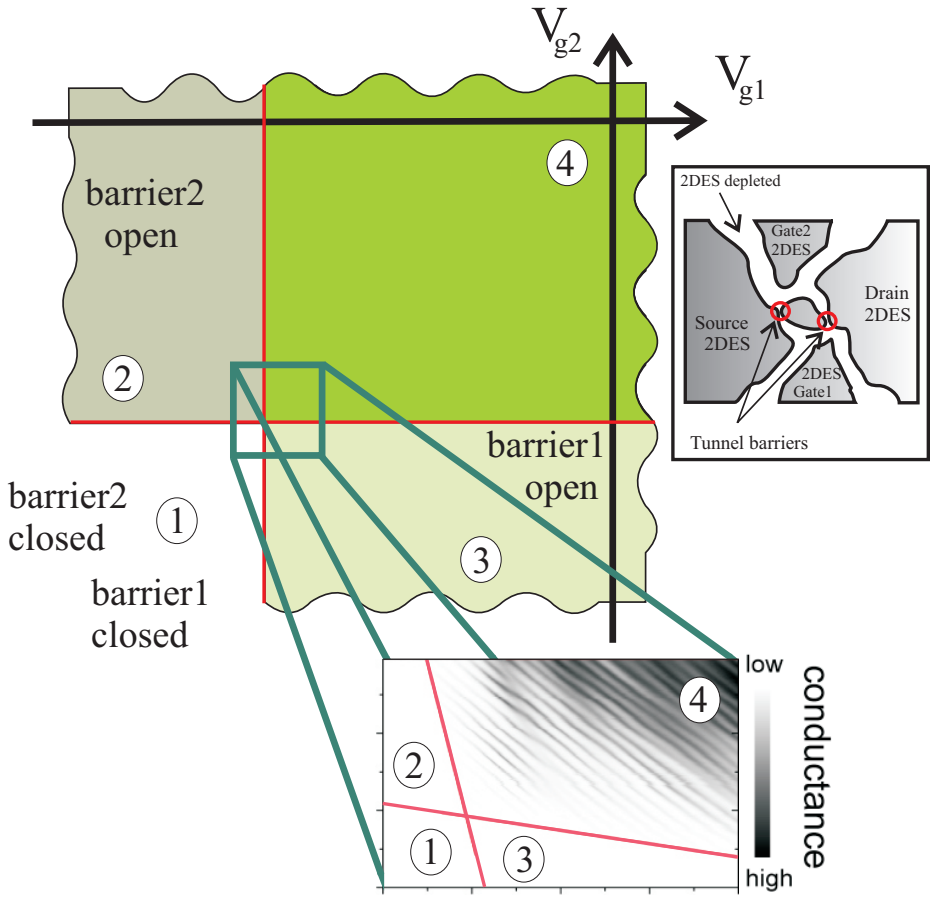

Figure 2.1: Schematic diagram of the $V_{g1}-V_{g2}$ plane showing four regions: in (1) both tunnel barriers are closed and no electrons can tunnel through the system, in (2) the tunnel barrier controlled by V_{g1} is open and electrons can tunnel between source and dot, in (3) the tunnel barrier controlled by V_{g2} is open and electrons can tunnel between dot and drain, and in (4) both tunnel barriers are open and transport through the system is allowed. In the upper insert a sketch of the electrostatic depletion is shown, where the tunnel barriers are marked by circles. In the lower insert a plot of the measured conductance as function of the gate voltages around the crossing region is shown. The borderlines for opening the tunnel barriers are also sketched; they show a finite slope, since, due to the structure of the QD system, a voltage applied to a gate affects both barriers.

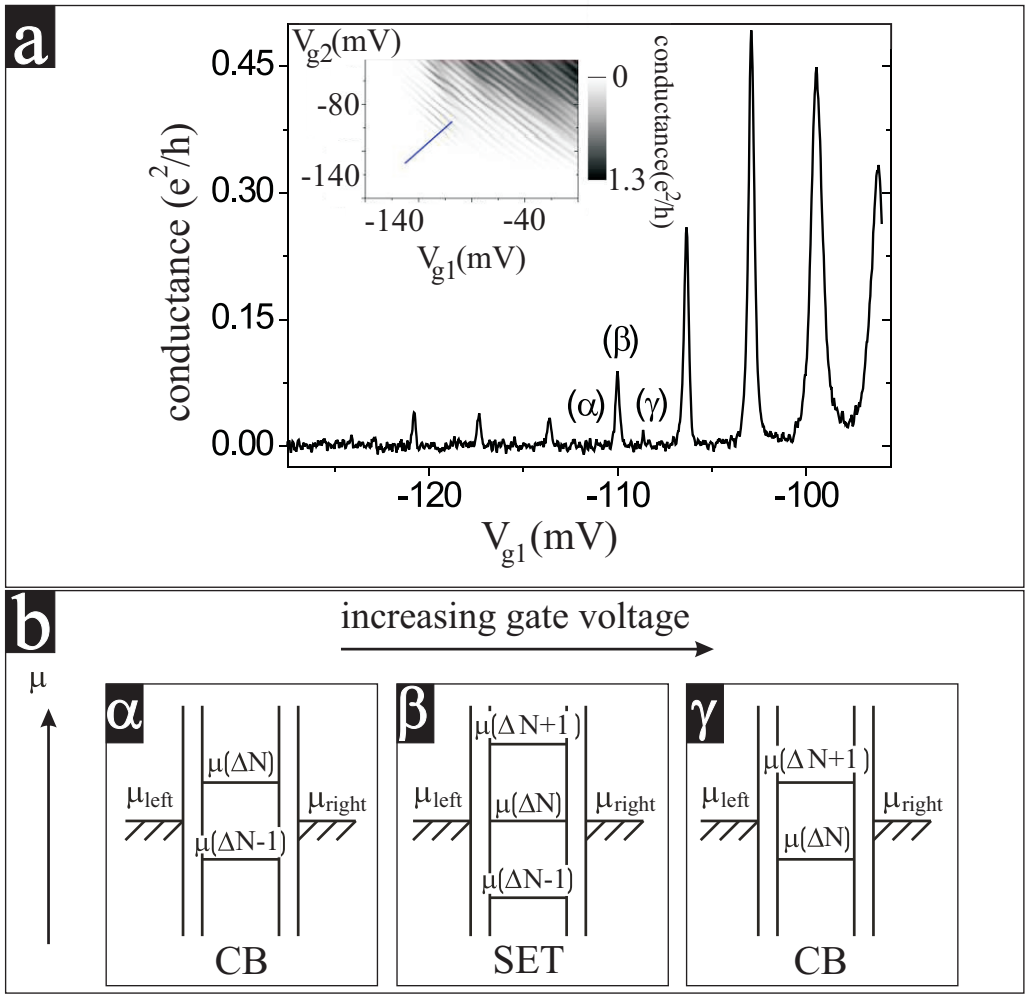

Figure 2.2: (a) Coulomb-Blockade Oscillations in a weakly coupled regime; the tunnel barriers are just starting to open allowing electrons to pass through the system. In the insert, the $V_{g1} - V_{g2}$ plane from which the CBO trace was chosen. (b) Energy schemes for distinct gate voltage values marked by $(\alpha)(\beta)(\gamma)$ in (a) where either Coulomb Blockade (CB) or Single Electron Tunnelling (SET) occur.

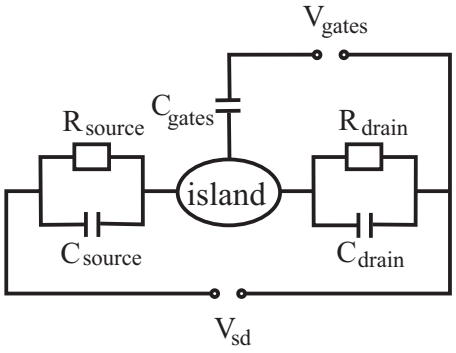

Figure 2.3: Capacitance circuit diagram modeling the electrostatics of the metal island system.

- electrically contacted metal electrodes (source and drain electrodes), weakly coupled to the island through tunnel barriers, and

- gate electrodes only capacitively coupled to the island.

Since a tunnel junction can be seen as a tunnel-resistance in parallel to a capacitance, the whole metal island system can be modelled with a circuit diagram like the one shown in Fig. 2.3. A capacitor is then formed between the island and the electrodes in its surrounding and an electron has to overcome a charging energy $E_C = \frac{e^2}{2C_\Sigma}$ in order to enter the island, where C_Σ is the total capacitance between the island and its surrounding.

More precisely, as pointed out by Beenakker in [10], the electrostatic potential difference between island and source electrode can be written as

$$\phi(Q, \{V_i\}) = \left(\frac{Q}{C_\Sigma} + \phi_{\text{ext}}(\{V_i\}) \right) , \tag{2.1}$$

where $Q = -\Delta N e$ is the total charge on the island when ΔN electrons beyond neutrality are trapped. The contribution of the voltages applied to the surrounding electrodes is included by ϕ_{ext} and, as can be deduced from the circuit in Fig. 2.3, it is equivalent to $\sum_i \frac{C_i}{C_\Sigma} V_i$.
Integrating Q from 0 to $-\Delta N e$, the electrostatic energy of the ΔN electrons transferred to the island is obtained as

$$U(\Delta N, \{V_i\}) = \frac{(-\Delta N e)^2}{2C_\Sigma} - \Delta N e \sum_i \frac{C_i}{C_\Sigma} V_i \, . \tag{2.2}$$

When an electron moves from the source to the island where $(\Delta N - 1)$ electrons are already trapped, it sees an energy difference $\Delta E_{\mathrm{s}\to\mathrm{i}}$ between source and island of,

$$\begin{aligned} \Delta E_{\mathrm{s}\to\mathrm{i}}(\Delta N, \{V_i\}) &= U(\Delta N, \{V_i\}) - U(\Delta N - 1, \{V_i\}) \\ &= \left(\Delta N - \tfrac{1}{2}\right) \frac{e^2}{C_\Sigma} - e \sum_i \frac{C_i}{C_\Sigma} V_i \,. \end{aligned} \tag{2.3}$$

For fixed gate voltages, $\Delta E_{\mathrm{s}\to\mathrm{i}}$ is drawn for increasing ΔN values in the energy scheme in Fig. 2.2 at the site of the quantum dot as energy levels

$$\mu(\Delta N, \{V_i\}) = \mu_{\mathrm{s}} + \Delta E_{\mathrm{s}\to\mathrm{i}}(\Delta N, \{V_i\}) \,, \tag{2.4}$$

where μ_{s} is the electrochemical potential (Fermi level) of the source. An equidistant ladder of energy levels which shift linearly with the gate voltages with respect to μ_{s} is obtained. Depending on $V_{\mathrm{g}i}$ (with $i = \{1, 2\}$) and on the number ΔN of additional electrons already present in the island, the electrostatic energy difference between source and island $\Delta E_{\mathrm{s}\to\mathrm{i}}(\Delta N)$ can be higher, equal or lower than zero. In the first case an energy barrier is found and the system is in a CB regime with $(\Delta N + 1)$ electrons trapped, in the second case, where the barrier is zero, the electrons can fluctuate between ΔN and $(\Delta N + 1)$ (i.e., single-electron tunneling is possible).
Setting (2.3) to zero, one can easily calculate the position in $V_{\mathrm{g}i}$ where the conductance peak occur,

$$V_{\mathrm{g}i}(\Delta N) = \left(\Delta N - \tfrac{1}{2}\right) \frac{e}{C_{\mathrm{g}i}} \,. \tag{2.5}$$

Moreover, the periodicity of the CBO , i.e. the distance between two consecutive peaks in the gate voltage axis, is given by

$$\Delta V_{\mathrm{g}i} = \frac{e}{C_{\mathrm{g}i}} \,. \tag{2.6}$$

Keeping instead the values of the gate voltages fixed at zero, in order to charge the island with the ΔN^{th} electron, the electrostatic energy difference between source and island is

$$\Delta E_{\mathrm{s}\to\mathrm{i}} = \frac{e^2}{2C_\Sigma} \,. \tag{2.7}$$

As sketched in Fig. 2.4, the distance between two consecutive energy level in the island is always equal to two times the charging energy. In this case the barrier that has to be overcome in order to enter or leave the island is maximum and is equal to the charging energy.

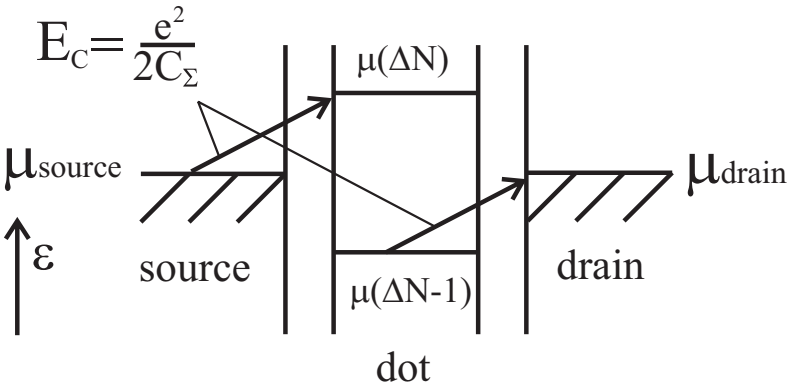

Figure 2.4: Energy scheme of a metal island system describing the single-electron transport. When the source-drain and the gates voltages are zero, as shown here, the ΔN^{th} electron entering the island or the $(\Delta N - 1)^{th}$ electron leaving have to overcome an energy barrier equal to the charging energy E_C.

2.3 Coulomb Blockade Oscillations in the $V_{g1}-V_{g2}$ plane

One can extract more information about the QD plotting the conductance as a function of both lateral gate voltages, like in Fig. 2.5.
Since the applied gate voltages also affect the electrostatic potential of the island, the number of trapped electrons ΔN for the linear-response regime is given by [11]

$$\Delta N(V_{sd} = 0; V_{g1}, V_{g2}) = \text{int}\left(\frac{C_{g1}V_{g1}}{e} + \frac{C_{g2}V_{g2}}{e} - \left(\frac{Q^*}{e} - \tfrac{1}{2}\right)\right), \qquad (2.8)$$

where

$$Q^* = Q^*(V_{sd} = 0, V_{g1} = 0, V_{g2} = 0) = -\sum_{\substack{j=1 \\ j\neq\{g1,g2,d\}}}^{M} C_j V_j + Q_{ion}\,. \qquad (2.9)$$

The index j refers to the additional gate electrodes electrostatically coupling to the island via C_j beside gate1 and gate2. The effect of charged impurities in the surroundings are also taken into account via Q_{ion}. In the zoom in of the measurement of Fig. 2.5, the borderlines between two adjacent charge states of the island are highlighted. From (2.6), along the V_{g1} axis, the distance

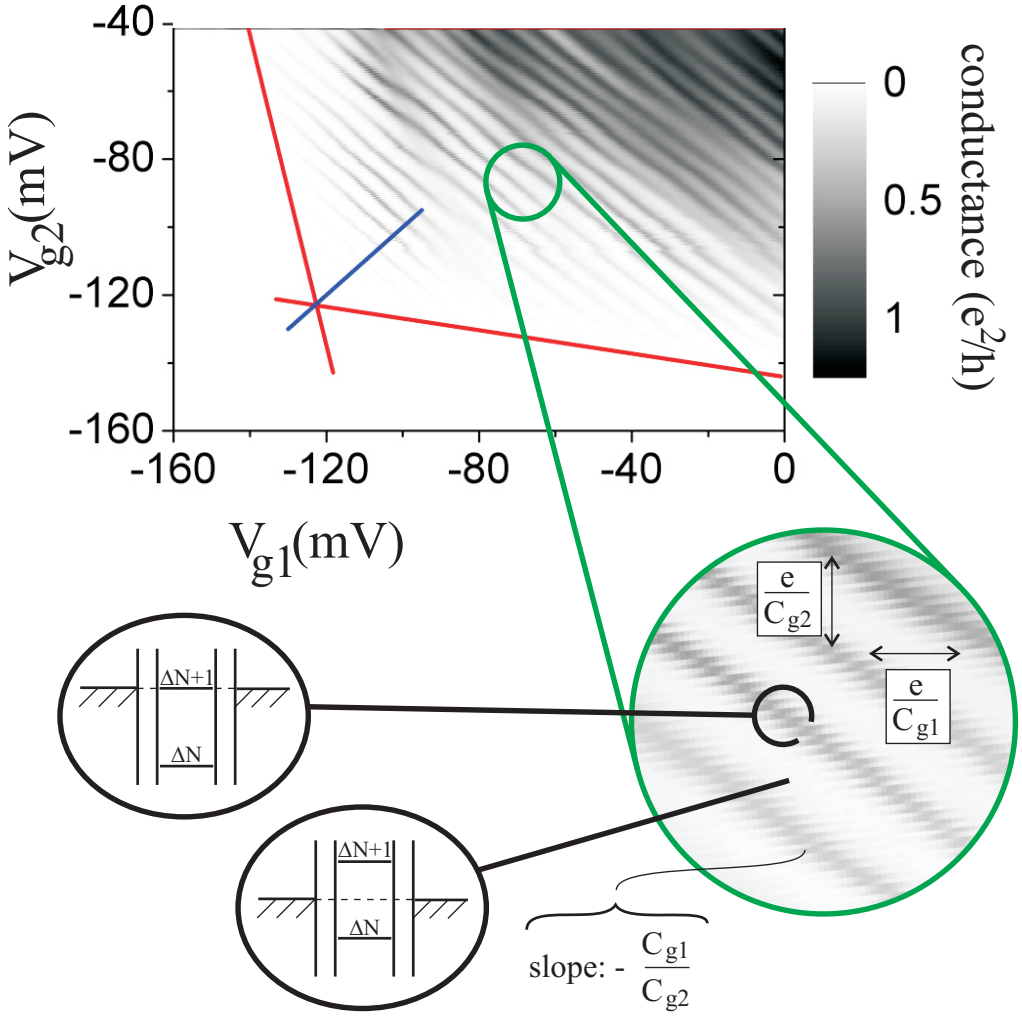

Figure 2.5: Conductance in grey scale plotted as a function of both lateral gate voltages; the bias voltage V_{sd} is nearly zero and the ac modulation is 1 μV in rms of amplitude. A zoom in is also shown together with energy schemes referring to two points in the $V_{g1} - V_{g2}$ plane indicating CB and SET conditions. A small hysteresis in the position of the Coulomb peaks can be noticed here; it is due to the way in which the measurements were taken, sweeping in one direction the voltage on V_{g1} while keeping the value of V_{g2} fixed and then sweeping it back in the opposite direction for the next value of V_{g2}, following a meander pattern.

between two adjacent borderlines is given by $\Delta V_{g1} = e/C_{g1}$ and, along the other axis, by $\Delta V_{g2} = e/C_{g2}$. The slope of these borderlines is

$$\frac{\partial V_{g1}}{\partial V_{g2}} = -\frac{C_{g2}}{C_{g1}}\,. \tag{2.10}$$

From this relation, one can see that sweeping the gate voltages parallel to a borderline will keep the energetic barriers for recharging the dot equal. Choosing instead a path that crosses the lines, a series of periodic CBO will be observed.
For our measurements it is wishful to open the barriers symmetrically while measuring a CBO trace in the $V_{g1} - V_{g2}$ plane. The best trace for doing so is presumably a line diagonal to the borderlines defining the opening of the tunnel barriers and going through the crossing point of these borderlines. In Fig. 2.5 this trace is marked and has been chosen also for Fig. 2.2.

Plotting the conductance in the $V_{g1} - V_{g2}$ plane also allows to obtain valuable information about the quality of the dot formed inside the island.
Fig. 2.6 gives some examples of Coulomb-Blockade Oscillations showing a modulation in their amplitude which we attribute to intrinsic static potential fluctuations due to disorder. This behavior was already discussed in detail in [1] and [12], where these modulations were phenomenologically divided in four categories:

I: The conductance modulations are found with their minima shifting parallel to one of the borderlines marking in the $V_{g1} - V_{g2}$ plane the opening of the tunnel barriers (Fig. 2.6-I).

II: The position of the Coulomb peak does not follow a straight line in the $V_{g1} - V_{g2}$ plane but presents instead a jump or a break (Fig. 2.6-II).

III: The conductance modulation is lying diagonally to both borderlines marking the opening of the tunnel barriers (Fig. 2.6-III).

IV: The CBO show an irregular modulation pattern in the $V_{g1} - V_{g2}$ plane (Fig. 2.6-IV).

These modulations have been explained by the following physical considerations.

Case I: This defect is linked to the formation of smaller QDs in the tunnel barrier regions. The origin of these smaller dots comes from intrinsic potential fluctuations in the system. When the distance of the Fermi

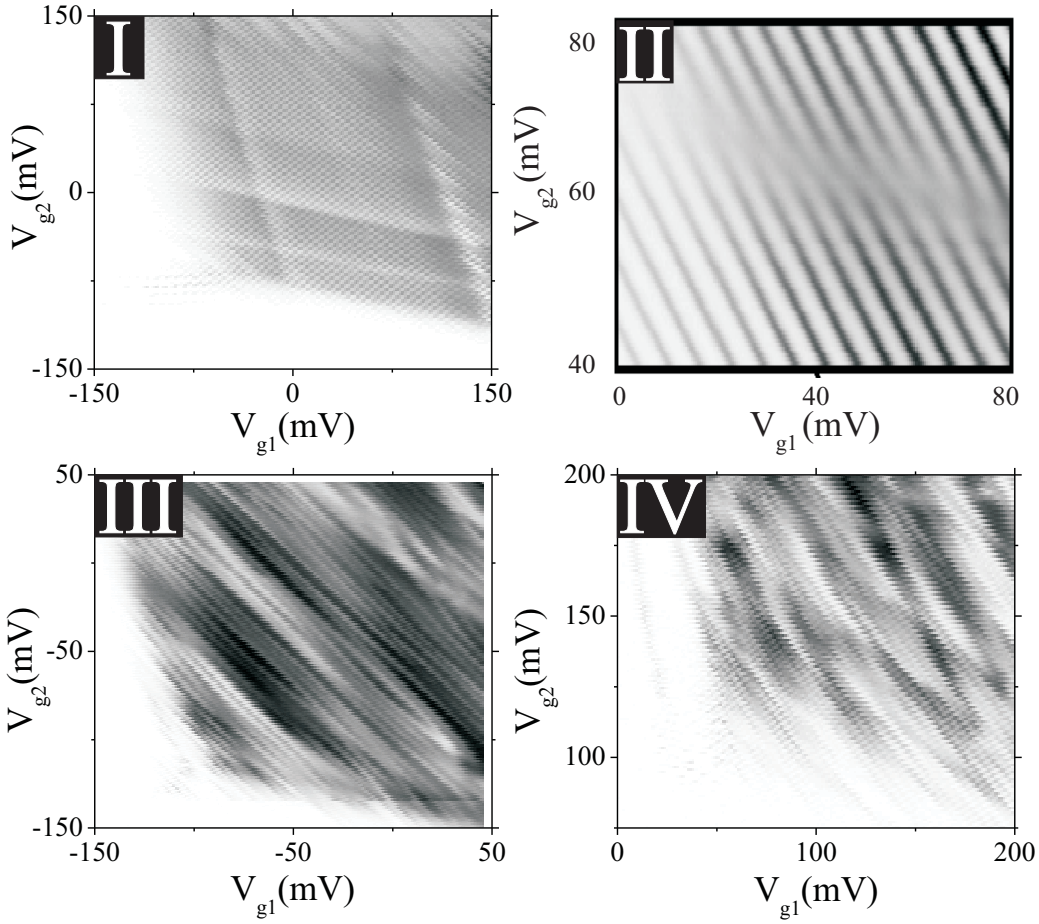

Figure 2.6: Amplitude modulations of the Coulomb Blockade Oscillations for four different disordered QD systems.

energy from the top of the potential barriers is bigger than the amplitude of the fluctuations, an effective barrier is still present. When instead the static fluctuations are large and create other suitable minima in which the electrons can be confined, smaller dots are formed. The overall conductance is affected by all the dots in series: this means that before reaching the intentional dot from the lead, the electrons have also to go through the other dots. If these dots are strongly tunnel-coupled to a lead and small, they lead to the amplitude modulations shown in Fig. 2.6-I.

Case II: The second type of modulations on Fig. 2.6-II are due to an impurity in the vicinity of the island. For certain values of the gate voltages, this impurity can be charged, affecting the position of the Coulomb peak in the main dot. As the result, the affected CP line shifts in the $V_{g1} - V_{g2}$ plane, showing a jump with respect to the extrapolated position.

Case III: In the third type of modulation, the additional QD, as the ones described for Case I, is electrostatically coupled to both gate electrodes, so that the minimum of the modulation shifts diagonally to both borderlines marking the opening of the tunnel barriers.

Case IV: In the last type the previous cases are combined, so that the observed modulation has no clear pattern.

The point then is to understand what causes these potential fluctuations. They can have the following intrinsic origins:

- distribution of charged donors in the doped AlGaAs layer,
- presence of impurities in the layers embedded during the MBE process,
- interface roughness between the AlGaAs and the GaAs layers, and
- defects of the lattice.

On the other hand, the origin can also be in the sample preparation process:

- roughness of the etched surfaces,
- photo- and electron-beam-resist residuals on the surface, and
- lattice defects caused by the etching process.

Finally, even several cooling-down process can create different intrinsic potential landscape by freezing in certain impurity charge configuration.
After the sample is made, warming-up and cooling-down cycles are the only way to find a suitable sample, when possible.

During our experimental studies, over 80 samples have been measured and characterized; a significant majority of them showed an electrical transport dominated by modulations in the CBOs amplitude due to disorder in the system and were therefore inadequate for our purposes, since we needed dots that could preserve their good quality over very wide parameters ranges. A smooth potential profile in the QD system proved itself to be an essential requirement in our experiments.

2.4 Conductance as a function of the source-drain and the gate voltages

In the non-linear transport regime, a dc voltage is applied between the leads. Applying V_{sd}, the Fermi energy levels of both sides shift against each other. An energy window is then opened and, as long as an energy level at the site of the dot, $\mu(\Delta N)$, falls within this window, at least single-electron tunneling is possible.
A typical measurement is shown in Fig. 2.7; here the gate voltages are swept following the same trace of the previous data in the linear regime. From the plot one can see that applying a finite source-drain voltage the Coulomb-Blockade regions are reduced and transport occurs over a broadener region. The diamond-like shape of the different regions can be explained within the electrostatic theory given in Section 2.2. As will be shown in the following, from this kind of measurements one can extract important information about the transport parameters of the system, like for example the single-electron charging energy E_C.
Following the scheme given in [11], the positive V_{sd} case is considered first. Taking into account also a finite V_{sd}, the electrostatic charging energy felt by an electron moving from the source to the island is expressed as

$$\Delta E_{\mathrm{s}\to\mathrm{i}}(\Delta N+1, V_{\mathrm{g}}, V_{\mathrm{sd}}) = \left(\Delta N+\tfrac{1}{2}\right)\frac{e^2}{C_\Sigma} - e\,\frac{C_{\mathrm{g}}}{C_\Sigma}\,V_{\mathrm{g}} - e\,\frac{C_{\mathrm{d}}}{C_\Sigma}\,V_{\mathrm{sd}}\,. \quad (2.11)$$

To allow the electrons to enter the island, the energy difference between source and island has to be less than zero. Therefore, the threshold gate

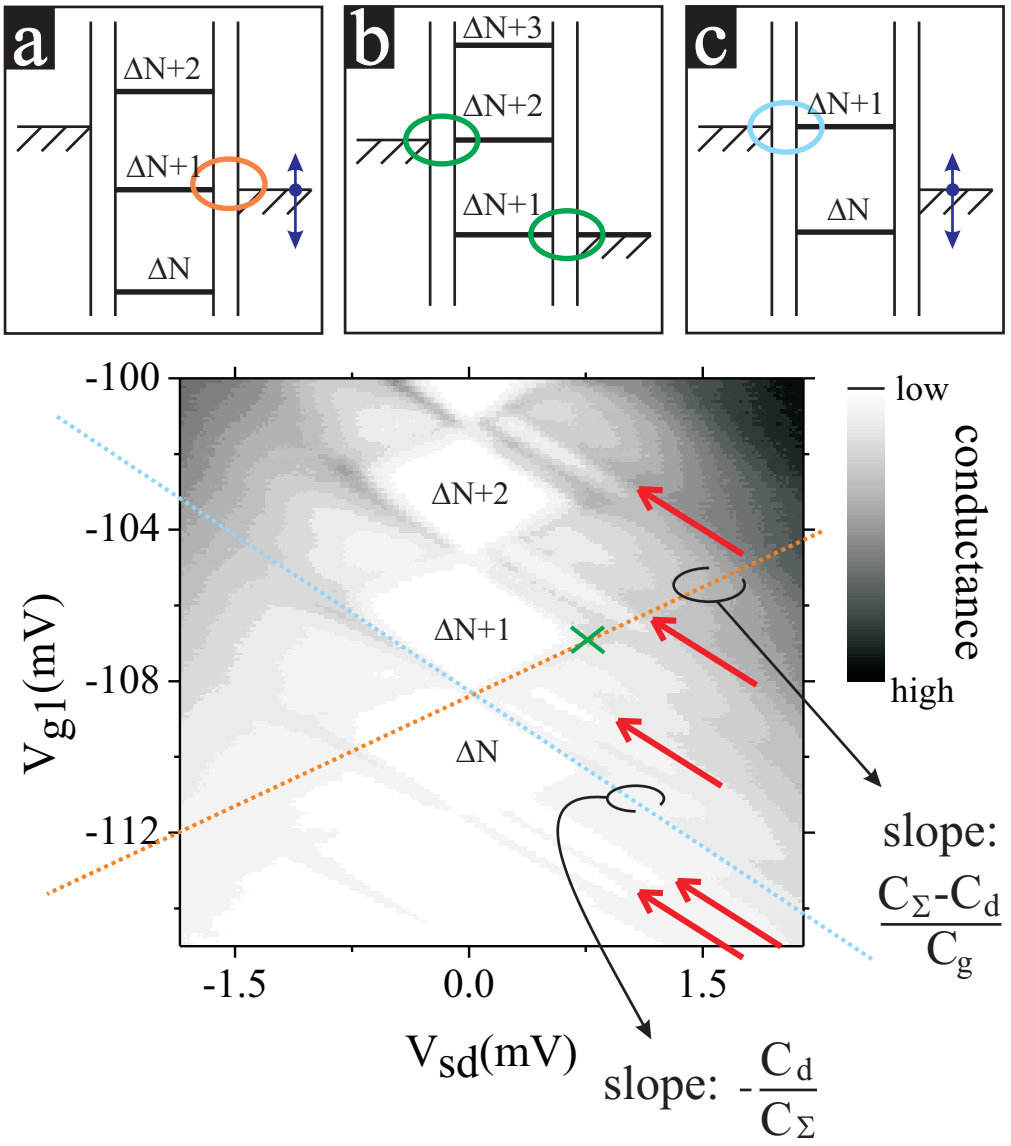

Figure 2.7: Differential conductance measured as a function of the source-drain and of the gate voltages. The intensity of the conductance is plotted in the grey scale and in the white regions the transport is not allowed (CB). Energy schemes are given for the part marked on the measurements.

voltage value is define by $\Delta E_{\mathrm{s}\to\mathrm{i}} = 0$, leading to

$$V_{\mathrm{g}} = \frac{1}{C_{\mathrm{g}}}\left(\Delta N + \tfrac{1}{2}\right) e - \frac{C_{\mathrm{d}}}{C_{\mathrm{g}}} V_{\mathrm{sd}} \,. \tag{2.12}$$

The electrostatic energy needed by an electron that would like to move from the island to the drain instead is

$$\Delta E(\Delta N + 1, V_{\mathrm{g}}, V_{\mathrm{sd}}) = \left(\Delta N + \tfrac{1}{2}\right) \frac{e^2}{C_\Sigma} - e\,\frac{C_{\mathrm{g}}}{C_\Sigma} V_{\mathrm{g}} - e\left(1 - \frac{C_{\mathrm{d}}}{C_\Sigma}\right) V_{\mathrm{sd}} \,. \tag{2.13}$$

The respectively threshold gate voltage value is obtained for

$$V_{\mathrm{g}} = \frac{1}{C_{\mathrm{g}}}\left(\Delta N + \tfrac{1}{2}\right) e - \frac{C_\Sigma - C_{\mathrm{d}}}{C_{\mathrm{g}}} V_{\mathrm{sd}} \,. \tag{2.14}$$

A similar discussion can be made for negative V_{sd}, obtaining the same dependence for V_{g}. Varying ΔN in the formulae (2.12) and (2.14), a set of parallel borderlines come out, forming the diamond-shaped pattern seen in Fig. 2.7. In this figure, there are also energy schemes for certain points in the $V_{\mathrm{g1}} - V_{\mathrm{sd}}$ plane, referred to the situations described before. The one in the middle (b) shows a particular situation: keeping V_{g} fixed and increasing V_{sd}, after the point indicated in the figure with a cross, the Coulomb-Blockade effect is overcome for any values of V_{sd}. This means that the bias source-drain voltage is big enough to include always at least one $\mu(\Delta N)$ and thus single-electron tunneling is always possible. Taking into account that the size of the energy window for (b) is eV_{sd}, the threshold in the source-drain voltage is given by

$$V_{\mathrm{sd}}^{\mathrm{threshold}} = \frac{e}{C_\Sigma} = \frac{2E_C}{e} \,. \tag{2.15}$$

Extracting from the data the value of $V_{\mathrm{sd}}^{\mathrm{threshold}}$ the charging energy of the system can be calculated. Here it is $E_C \approx 0.52$ meV.

2.5 Features indicating the presence of the quantum dot

Up to here, the electrical transport properties were discussed for the case of a metal island. In the present thesis the sample is a quantum dot, as will become clear from the following discussion. However, pointing out some differences, the main results of the electrostatic theory are still applicable.

In a metal island in fact the energy spectrum is a continuum, like in the usual conduction band of a bulk metal.
Instead, in a semiconductor material like the one used here, the electron density in the conduction band is lower, so that the kinetic energy of the electrons at the Fermi level is also lower, resulting in a bigger Fermi wavelength, described by (1.1). The single-particle eigenenergy spectrum is now a discrete one. This has then to be incorporated into the ladder scheme discussed up to here for presenting the single-electron tunneling in a metal system. For doing so, it requires the quantum-mechanical treatment of N interacting electrons in the given confining potential on the QD site. To describe transport, now we have to plot as energy levels on the QD site

$$\mu(N, \{V_i\}) = E(N, l = 0; \{V_i\}) - E(N - 1, l = 0; \{V_i\}) \,, \tag{2.16}$$

where $E(N, l = 0; \{V_i\})$ is the total ground-state energy of the interacting N-electrons system confined in the quantum dot for given voltages $\{V_i\}$.

Furthermore, as it will be more detailed discusses in the following, by tuning the coupling between island and leads, a variety of different phenomena arises from the measurements, giving fundamental insights on the internal configuration of the system under examination: For small coupling regimes, transport through excited states of the quantum dot can be observed, for intermediate coupling regimes, higher-order tunneling events through the system can occur, denoted as correlated tunneling. Particular cases of correlated tunneling are the cotunneling (i.e. correlated tunneling of two electrons/holes) and the the Kondo effect. Finally, for strong coupling regimes, when the QD systems is close to became an open channel that moves from the source to the drain leads, the Fano effect can also be observed.

Additional single-electron transport channels by excited states

In Fig. 2.7 some more structures are observed, as highlighted by the red arrows: Inside the SET regions some additional peaks in the differential conductance come out, indicating a step-like increase in the current flowing from the source to the drain. The position of these peaks is shifted parallel to a borderline between CB and SET regions. Thus there are more transport channels in the system becoming available in the SET regime. This fact is explained by the presence of excited states; an electron can tunnel from source to drain using either the ground or excited states of the QD [11].
In Fig. 2.8 different energy schemes are shown; the V_{sd} is kept at a fixed

value (different from zero) and (V_{g1}, V_{g2}) are swept as marked by the line in the sketch of the charge stability diagram, shifting therefore the electrostatic potential of the dot.

- In Fig. 2.8a, the system is in the Coulomb Blockade regime and transport is not allowed.

- In Fig. 2.8b, by increasing the gate voltages, $\mu(N)$ is aligned to the electrochemical potential of the source; the system is in the single-electron tunneling regime. This is the transition with the lowest possible energy.

- By increasing further the gate voltages, also a transition to an excited state of the N-electrons system is possible, as indicated in Fig. 2.8c. The required energy for doing so is

$$\mu^*(N, \{V_i\}) = E(N, l; \{V_i\}) - E(N-1, l=0; \{V_i\}) \,, \qquad (2.17)$$

  where $E(N, l; \{V_i\})$ is the total energy of the excited state $|N, l\rangle$. This gives an additional energy level in the energy scheme for describing transport (see dashed lines in the figure). At the point (c) in the parameters space of V_g vs. V_{sd}, the system is in the single-electron regime and electrons can enter into the dot either at an energy level $\mu(N)$ or $\mu^*(N)$, but these two channels cannot be used at the same time. Therefore this additional channel makes the conductance increase because of a higher probability of an electron entering into the dot.

Not particularly highlighted in Fig. 2.7 but still frequently observed, transport via excited states can occur also whenever an additional channel for electrons to leave the QD is opened in resonance to the drain lead. In this case the increased conductance line will be running parallel to the $\mu(N) = \mu_{drain}$ borderline.
The spacing between this additional differential conductance peaks is therefore a measure of the excitation energy with a constant number of electrons on the dot.
Moreover, this kind of measurements is a direct proof that a quantum dot is really formed inside the system, otherwise would be not possible to resolve excited states. In the case of a metal island in fact there would be a dense excitation spectrum and the probability of single-electron tunneling would be continuously increasing with V_{sd}.

Cotunneling

In the description of the basic electrical transport properties of a QD system carried out so far, the island has been considered as weakly coupled to source

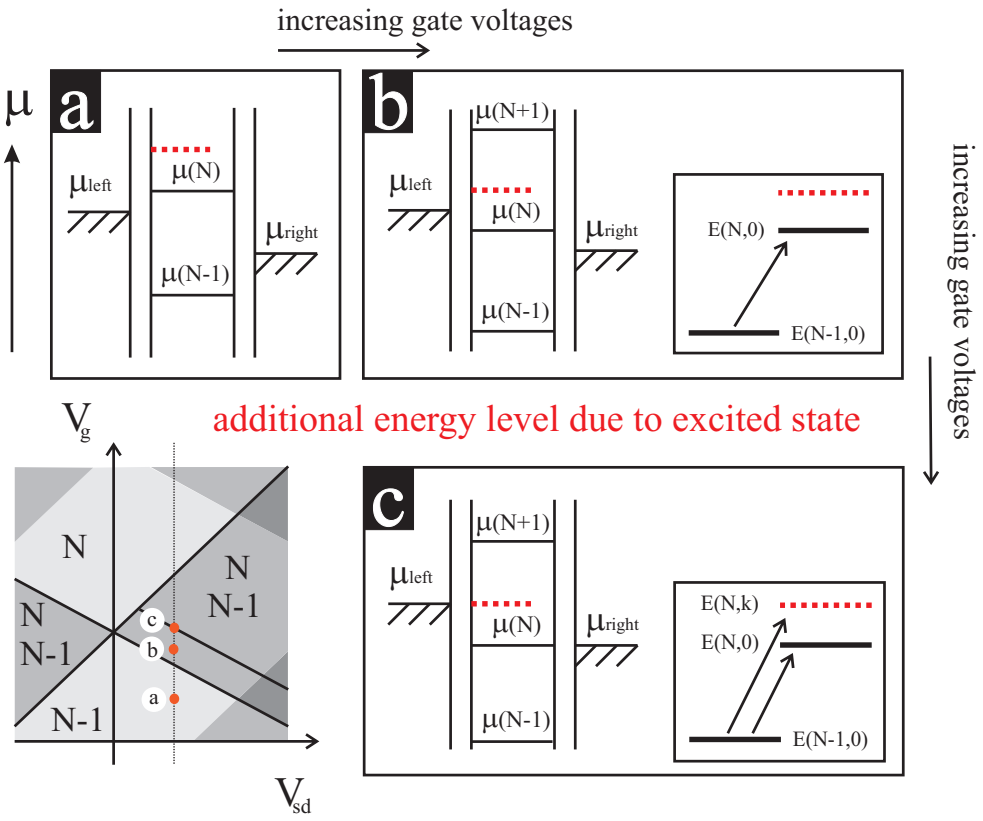

Figure 2.8: Energy schemes of single-electron transport through the system in the presence of excited states in the quantum dot. Each of them is referred to a fixed value of the source-drain voltage, shown in the sketch by the line in the parameters space of V_g and V_{sd}. (a) There are no levels of the dot in the energy window formed by the electrochemical potentials of the leads and single-electron tunneling is not allowed. (b) The ground-state transition energy $\mu(N)$ is aligned to the electrochemical potential of the source and tunneling into the dot is possible. In the insert: the energy transition required in order to tunnel through the dot. (c) Both $\mu(N)$ and $\mu^*(N)$ are inside the energy window between the reservoirs potentials and two channels for tunneling into the dot are available. In the insert: the two possible alternative transitions shown in the total energy spectrum of the quantum dot.

and drain leads so that tunneling events could be considered as being independent from each others. Transport through the system was allowed only when an energy level of the dot is aligned within the energy window formed between the electrochemical potentials of the leads. This type of transport is defined **single-electron tunneling** and it does not take into account the Heisenberg principle and the fact that energy conservation requirements can be raised on a short time scale.
By enhancing the tunnel coupling, although, higher-order tunneling events can become significant. This second type of transport is defined as **correlated tunneling**, due to the involvement of two or more electrons simultaneously; the charging and discharging of the island occurs *virtually* via quantum fluctuations.
At lowest order, there are two different means for the correlated tunneling to take place:

- Hole-like cotunneling, where an electron leaves the island and it is correlated replaced by an other one entering.
  Let us consider a QD in the Coulomb Blockade regime, with N electrons trapped within in their groundstate. In order for an electron in the dot to reach the drain lead at an energy $\varepsilon_{\rm drain} \geq \mu^{\rm elch}_{\rm drain}$, leaving the island in the state $|N-1,0\rangle$, the following energy requirement must be fulfilled:

$$\begin{aligned} \Delta E_{\rm i\to d} &= [(\varepsilon_{\rm drain} - \mu^{\rm elch}_{\rm drain}) + E(N-1,m;\{V_i\})] - E(N,0;\{V_i\}) \\ &\geq 0\,. \end{aligned} \tag{2.18}$$

  This process can take place only if $\Delta E_{\rm i\to d}\cdot\tau < \hbar$, so that the state for which there are $N-1$ electrons left in the island is a virtual intermediate state. In its turn, the virtual state will decay when an electron enters the QD from the source side and by such a transition the system gains energy

$$\begin{aligned} \Delta E_{\rm s\to i} &= [E(N,l;\{V_i\}) - E(N-1,m;\{V_i\})] - (\varepsilon_{\rm source} - \mu^{\rm elch}_{\rm source}) \\ &\leq 0\,, \end{aligned} \tag{2.19}$$

  with $\varepsilon_{\rm source} \leq \mu^{\rm elch}_{\rm source}$. The overall process doesn't violate energy conservation if

$$\Delta E_{\rm i\to d} + \Delta E_{\rm s\to i} = 0\,. \tag{2.20}$$

- Electron-like cotunneling on the other hand involves an electron entering the island first and immediately a correlated electron leaving.

The initial step costs an energy

$$\begin{aligned} \Delta E_{\mathrm{s}\to\mathrm{i}} &= E(N+1,k;\{V_i\}) - [(\varepsilon_{\mathrm{source}} - \mu^{\mathrm{elch}}_{\mathrm{source}}) + E(N,0;\{V_i\})] \\ &\geq 0\,, \end{aligned} \tag{2.21}$$

(where $\varepsilon_{\mathrm{source}} \leq \mu^{\mathrm{elch}}_{\mathrm{source}}$) compensated by the energy gained by an electron leaving the island

$$\begin{aligned} \Delta E_{\mathrm{i}\to\mathrm{d}} &= [(\varepsilon_{\mathrm{drain}} - \mu^{\mathrm{elch}}_{\mathrm{drain}}) + E(N,l;\{V_i\})] - E(N+1,k;\{V_i\}) \\ &\leq 0\,, \end{aligned} \tag{2.22}$$

with $\varepsilon_{\mathrm{drain}} \geq \mu^{\mathrm{elch}}_{\mathrm{drain}}$.

Note that both hole-like and electron-like cotunneling can take place also via excited states and this leads to a further distinction: a cotunneling event is called inelastic when it leaves the dot in an excited states, otherwise it is classified as elastic.
Moreover, the two types of cotunneling processes can be energetically allowed at the same time, even if they might have different probabilities to occur.

In Fig. 2.9 the measured stability diagram of a QD system is shown: besides the previously discussed single-electron tunneling transport, further features emerge from the greyscale plot. As schematically explained by the energy sketches in the lower section of the figure, single-electron-transmission occurs through the borderlines highlighted by the white dashed lines, either via ground states (the outer borders of the diamond-shaped regions) or via excited states (lines marked respectively as **a** and **b** in the measurements). Unlike in Fig. 2.7, where the center of the diamond-shaped region was characterized by zero conductance (Coulomb Blockade regime), here instead one can see signatures of a reduced but not completely suppressed current through the QD system. The orange dotted lines mark the border between elastic (**d**) and inelastic (**c**) transport regions [13]. The first one is dominant at low bias source-drain voltages and concerns electron traveling via the island ground state. Inelastic cotunneling, to not violate energy conservation requirements, can occur only whenever the energy window formed between the electrochemical potentials of the leads is at least equivalent to the distance in energy between the groundstate and the first excited state on the QD. This is even more clear when noticing that the borderline between elastic and inelastic cotunneling connects to that of single-electron tunneling through an excited state outside the Coulomb blockaded region.
The requirement under which the overall cotunneling process can occur is that the energy difference between the electron entering and the one leaving the island is smaller or equal to the energy window opened between source

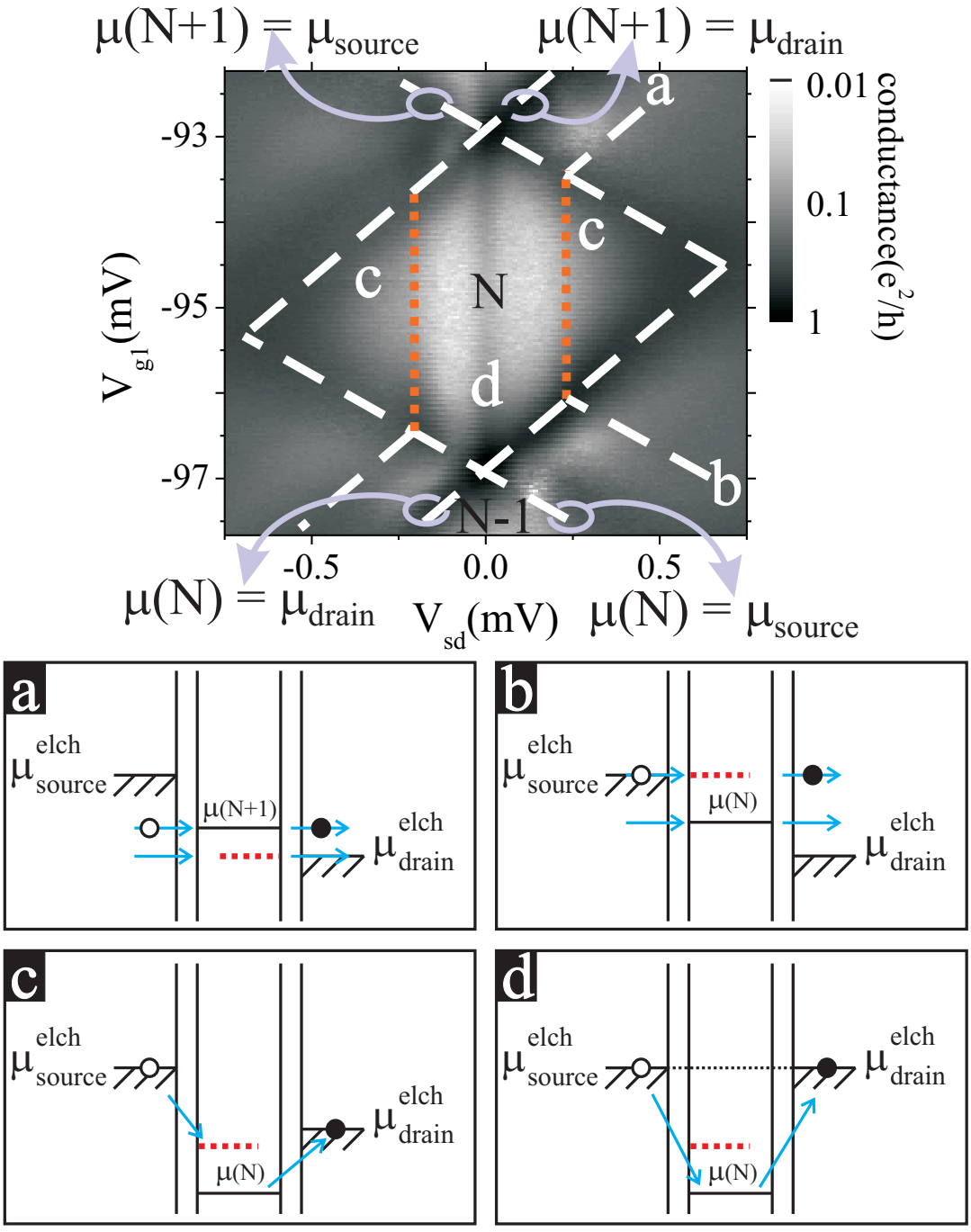

Figure 2.9: Top: differential conductance in greyscale (logarithmic) measured as a function of the source-drain and of the gate voltages. Dashed lines have been superimposed to highlight the onset of different transport regimes. Bottom: Energy schemes referring to the different types of transport marked in the charge stability diagram.

and drain leads and it does not involve considerations on the electrostatic potentials $\{V_i\}$; the borderlines defining the starting conditions of this process are therefore independent on $\{V_i\}$, as can be seen by their lying parallel to the V_g-axis.

Zero-bias anomaly

In the measurements shown in Fig. 2.9, there is a last feature that has not been discussed yet: a sharp differential conductance peak at $V_{\mathrm{sd}} = 0$ in the Coulomb Blockade region, often referred to as **zero-bias anomaly**. In order to explain this anomaly, correlated transport involving more than just two electrons has to be considered.

Such a feature had been observed quite frequently in the past years ([15],[14], [4]) and it has been explained via a mapping of the Anderson Impurity Model [16] into the case of a QD system. The Anderson Impurity Model was formulated to describe the increase of the resistivity in bulk materials with magnetic impurities due to spin-scattering of electrons in the Fermi sea at these impurity sites.

Fig. 2.10a shows how to apply this model to the case of transport through 0D systems:

- On the left, the bulk case is sketched as the energy of the degenerate impurity site, ε_0, lying below the Fermi level of the electrons sea, ε_{F}. Since $\varepsilon_0 < \varepsilon_{\mathrm{F}}$, the impurity level is always occupied by a single electron, while double occupancy is suppressed by Coulomb repulsion. Due to the initial degree of freedom (to occupy the impurity site by either a spin-up or spin-down electron) at low temperature a many-body state is formed, known as Kondo state.

- On the right side of Fig. 2.10a, the case of a QD system is sketched, highlighting the similarities between the two systems. Also here in fact a localized energy state (the one on the island) is tunnel-coupled to the electrons in the Fermi sea of the source and drain leads. A Kondo state is formed between the QD and its leads.

Unlike the bulk situation, where the many-body Kondo state was forming a cloud of electrons that, to screen the magnetic impurity, lead to an increase of the overall resistance, in a QD system the final effect is opposite. The electrons of the Kondo cloud increase in the latter the probability to tunnel through the island, leading to an increase in the conductance right in the middle of a Coulomb blockaded region (the zero-bias anomaly is therefore also denoted as Kondo effect).

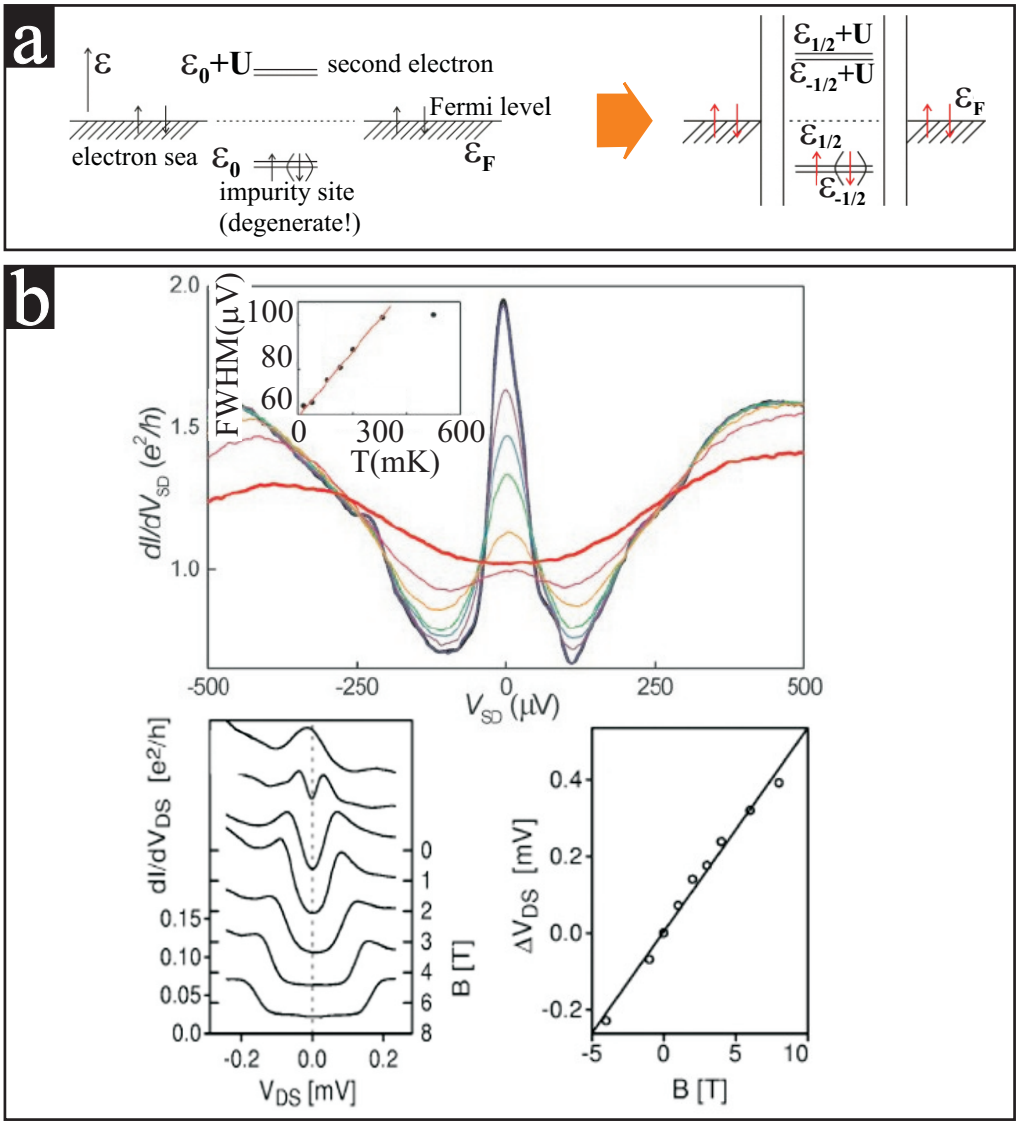

Figure 2.10: (a) Mapping of the Anderson Impurity Model into the QD system case. On the left: energy scheme for the case of a magnetic impurity embedded in a bulk semiconductor; the degenerate impurity energy level lies below the Fermi level of the electron sea. On the right: energy scheme for the QD system. The island takes the place of the impurity site and the leads take the role of the Fermi sea formed by the electrons in the conduction band. (b) Measurements of the zero-bias resonance in the differential conductance dI/dV_{sd} as a function of temperature (top, from [14]) and of magnetic field (bottom, from [4]).

Fig. 2.10b shows further measured properties of the zero-bias anomaly predicted by the Anderson Impurity Model.

- Top: The temperature dependence, as measured in [14], of the differential conductance around zero bias: at base temperature, the conductance between two Coulomb peaks reaches its maximum value and, increasing T, it gets suppressed. In the inset, one can in fact see that the full width half maximum (FWHM) of the zero-bias anomaly increases linearly with T.

- Bottom: the zero-bias resonance is measured as a function of the magnetic field [4], showing a split into two side peaks that move apart with increasing B, due to the lifting of the degeneracy of the energy level in the island; and

- the splitting of the Kondo resonance as a function of B-field; from the slope of the linear fit one can extract the value of the g-factor for GaAs ($eV_{\mathrm{sd}} = g_{\mathrm{GaAs}}\mu_{\mathrm{B}}B$).

Fano effect

Measurements of a situation in which the source and the drain leads are strongly coupled to the quantum dot is shown in Fig. 2.11a, from Göres *et al.* [17]. Here the differential conductance is plotted as a function of both the source-drain and the gate voltages and the usual diamond-shaped pattern characterizes the charge stability diagram. Contrary to similar measurements discussed earlier in this Chapter (see, for example, Fig. 2.7), though, in this Figure low conductance is plotted as dark grey. This means that, instead of the usual Coulomb Blockade peaks, here transport is characterized by sharp minima superimposed on a conductance background $G > 0$, as clearly highlighted by the line cuts of G vs. V_{g} shown on the right side of Fig. 2.11a. In order to explain such a feature, Göres *et al.* referred to earlier observations of Fano resonances, as in atomic photoionization experiments [18], where an analogue feature was observed as a result of an interference between a direct path and an other one going through a resonant site, as sketched in Fig. 2.11b. They therefore applied to the QD system configuration the Fano formula for the scattering cross-section,

$$\sigma(\varepsilon) \propto \frac{(\widetilde{\varepsilon} + q)^2}{\widetilde{\varepsilon}^{\,2} + 1}\,, \tag{2.23}$$

where $\widetilde{\varepsilon}$ is the dimensionless detuning from resonance and q is the asymmetry parameter, proportional to the ratio between the transmission amplitudes for

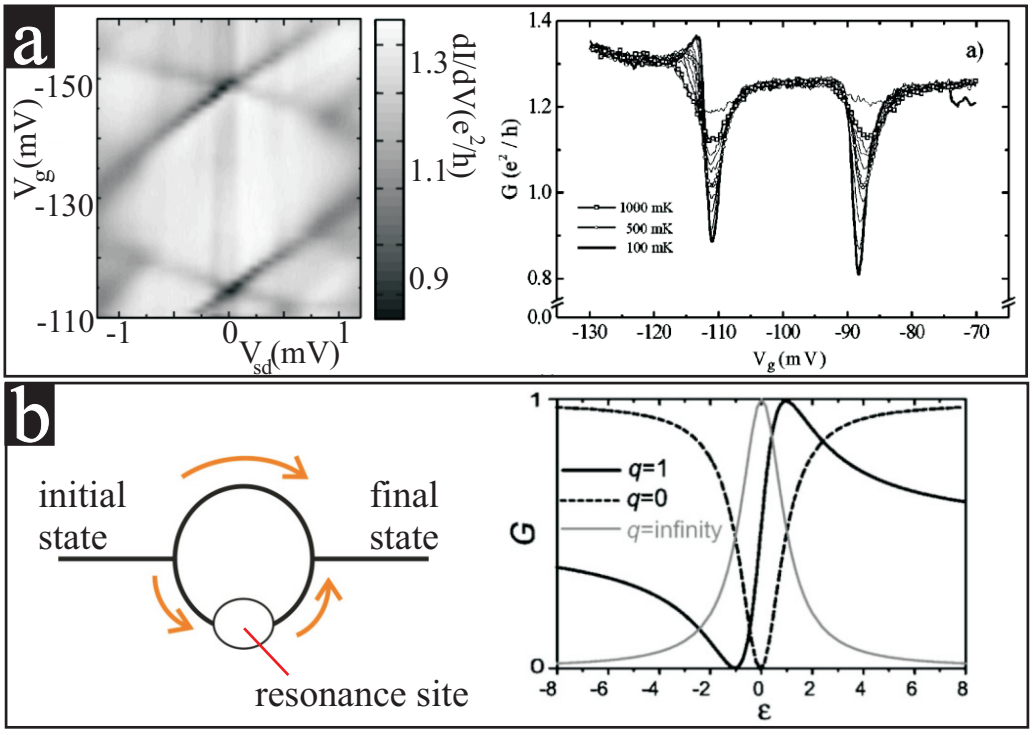

Figure 2.11: (a) Left: Charge stability diagram of a single-electron-transistor in strong coupling regime, from [17]. The conductance is plotted on the greyscale, where dark grey represents low conductance regions. Right: G vs. V_g for several temperature values. (b) Calculated Fano lineshapes for different parameters q and a sketch of possible interfering paths prerequisites to the occurrence of the Fano effect.

the transport through the resonance site and the non-resonant path. A result from the formula is depicted in Fig. 2.11b:

- When the parameter q goes to infinity, resonant transmission dominates and the conductance vs. gate voltage has a Breit-Wigner lineshape.

- If, on the other side, q goes to zero, then is the non-resonant transmission that dominates and the conductance vs. gate voltage is shaped as a symmetric dip.

From the fit of the experimentally measured G vs. V_{g} traces using (2.23), they finally concluded that the observed features could be indeed attributed to the Fano effect.
Exploring the influence of the temperature on the Fano lineshape, it was observed that its width increases linearly with T (as expected from Fermi-Dirac broadening), while its amplitude decreases logarithmically. Striking was the influence of the magnetic field, that showed that even small fields applied perpendicularly to the system could modify strongly the Fano lineshape.
The origin of the interference leading to the observation of the Fano effect was sought in the coexistence of two different transport channels, one undergoing Coulomb quantization, i.e. characterized by weak coupling between the leads and therefore equivalent to the resonant path in the sketch of Fig. 2.11b, the other analog to correlated tunneling events that then imply a stronger coupling between leads and therefore equivalent to a direct path.
In the following years, the Fano effect was widely studied in systems where the interference paths were explicitly defined, like Aharonov-Bohm interferometers with a QD embedded in one arm ([19]) or like quantum wires with a side coupled QD ([20]), leading to the observation of combined Fano-Kondo anti-resonances.

2.6 Modification in the internal electronic structure of the quantum dot due to the presence of an external magnetic field

Let us consider a two-dimensional non-interacting electronic system confined by a parabolic potential. Including in the model a homogeneous magnetic field B, the single-particle energy is given by the Fock-Darwin spectrum [21, 22] as

$$\varepsilon(m,l) = \Big(2m+ \mid l \mid +1\Big)\,\hbar\sqrt{\frac{\omega_0^2+\omega_c^2}{4}} + \tfrac{1}{2} l\,\hbar\omega_c\,, \tag{2.24}$$

where l is the angular momentum quantum number, m the radial quantum number, $\omega_c = \dfrac{eB}{m^*_{\text{eff}}}$ the cyclotron frequency, and ω_0 characterizes the strength of the parabolic confining potential.
However this picture is modified if one includes the Coulomb interaction between electrons; in high magnetic field in fact electrons rearrange themselves changing state in a way that cannot be explained in a non-interacting model.

The self-consistent model

A first improvement of this theory, including the electron-electron interaction, was given by McEuen *et al.* in [23]: there, the QD is seen as a small 2DES confined in a parabolic potential and a self-consistent (SC) model is developed. This model is based on the Thomas-Fermi approximation (TFA), where the electron system is described locally through a non-uniform electron density $\rho_{\text{sheet}}(\vec{r})$. This approximation is valid whenever the electrostatic potential varies smoothly on the scale of the magnetic length $l_B = \sqrt{\dfrac{\hbar}{eB}}$.
The electron density of the 2DES sheet would be, within a $B = 0$ treatment, as sketched in Fig. 2.12a; starting from a maximum in the center of the dot, it decreases smoothly moving towards the edges.
In the SC model, this profile comes out from minimizing the total energy of the island given by [23]

$$\begin{aligned} E_{\text{tot}}(N) \;=\; & \left(\sum_n \sum_{S_z} \Big[\,\big(n+\tfrac{1}{2}\big)\,\hbar\omega_c + g\mu_B B S_Z\Big] \int d^2\vec{r}\,\rho_{nS_z}(\vec{r})\right) \\ & + \int d^2\vec{r}\,\rho(\vec{r})\left(V_{\text{ext}}(\vec{r}) + \tfrac{1}{2}\int d^2\vec{r}\,'\,\rho(\vec{r}\,')V_{ee}(\vec{r},\vec{r}\,')\right) \end{aligned} \tag{2.25}$$

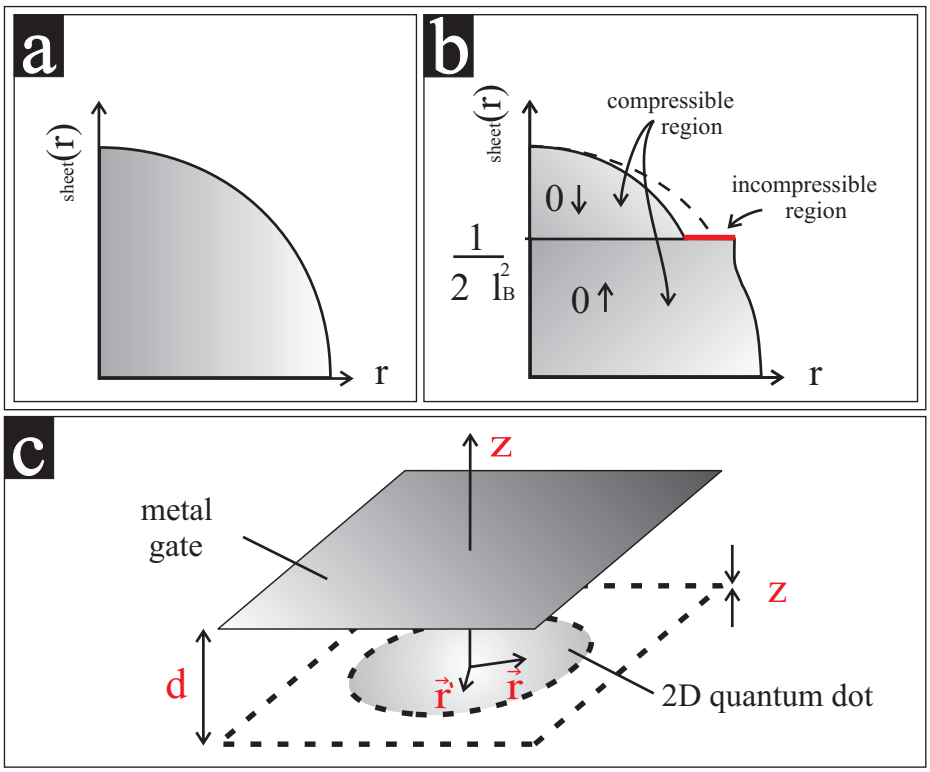

Figure 2.12: Internal electronic structure obtained from a self-consistent Thomas-Fermi approximation under the assumption of a parabolic confining potential in the $x - y$ plane. The magnetic field is so high that the electrons are find in the two lowest spin-resolved Landau levels. (a) The electron sheet density in the case of $B = 0$ vs. the dot radius is sketched. (b) The electron sheet density obtained from calculations within the SC model; $\frac{1}{2\pi l_B^2}$ is the LL degeneracy (*From* [23]). (c) Sketch showing the model parameters: $\vec{r}$ and $\vec{r}'$ are the position of the interacting electrons, d is the distance between the QD and the gate and δz is the thickness of the 2D quantum dot.

where $\rho_{nS_z}(\vec{r})$ is the sheet density of electron in the n^{th} spin-polarized LL, $\rho(\vec{r}) = \sum_n \sum_{S_z} \rho_{nS_z}(\vec{r})$ is the total electron density and $V_{ee}(\vec{r}, \vec{r}')$ is the electron-electron interaction. The e-e interaction is formalized as

$$V_{ee}(\vec{r}, \vec{r}') = \frac{e^2}{\epsilon_0 \epsilon \sqrt{\mid \vec{r} - \vec{r}' \mid^2 + \delta z^2}} - \frac{e^2}{\epsilon_0 \epsilon \sqrt{\mid \vec{r} - \vec{r}' \mid^2 + 4d^2}} \tag{2.26}$$

where, as sketched in Fig. 2.12c, d is the distance between the 2DES and a planar gate, $\epsilon = 13.6$ is the GaAs dielectric constant and δz is the thickness of the 2DES. This potential was chosen in order to take into account the finite thickness in the z-direction and the long-distance screening due to the image charges on the electrodes. In the model it is also assumed that the charge in each LL is quantized:

$$\int d^2\vec{r}\, \rho_{nS_z}(\vec{r}) = N_{nS_z}\,, \qquad \sum_n \sum_{S_z} N_{nS_z} = N\,. \tag{2.27}$$

A calculation, within the SC model, of the sheet density of electrons yields an electron density distribution like the one shown in Fig. 2.12b.

Compressible and incompressible strips

In McEuen's model a parabolic confining potential is assumed; in order to explain the Quantum Hall Effect, the TFA was afterwards applied to the edge regions of the 2DES [24], [25]. The main hypothesis used here is that the confining potential at the edges $V(\vec{r})$ varies smoothly in the plane of the 2DES, so that its characteristic depletion length is much larger than the magnetic length l_B. In order to calculate the electron sheet density, one has to consider

- the Poisson equation, linking the electron concentration to the electrostatic potential $\phi(\vec{r})$, and
- that the electrochemical potential has to be constant,

$$\mu^{\text{elch}} = \mu^{\text{ch}}(\vec{r}) - e\phi(\vec{r}) = \text{constant}\,, \tag{2.28}$$

  where the local chemical potential is a function of the local electron concentration $\mu^{\text{ch}}(\vec{r}) = \mu^{\text{ch}}(\rho_{\text{sheet}}(\vec{r}))$.

The electron sheet density obtained is

$$\rho_{\text{sheet}}(\vec{r}) = \int d\varepsilon\, D(\varepsilon)\, f\left(\frac{\varepsilon + V(\vec{r}) - \mu^{\text{elch}}}{k_{\text{B}}T}\right)\,, \tag{2.29}$$

where $f(\varepsilon) = [1 + \exp(\varepsilon)]^{-1}$ is the Fermi function and

$$D(\varepsilon) = \frac{1}{2\pi l_B^2} \sum_{j=0}^{\infty} \delta\Big(\varepsilon - (\hbar\omega_c(j + \tfrac{1}{2}) + g\mu_B B S_z)\Big) \tag{2.30}$$

is the density of states.

The results obtained from the TFA are shown in Fig. 2.13, taken from [26]. In (a), when the applied B-field is zero, the density of states $D(\varepsilon)$ is constant, leading to μ^{ch} that is linear as a function of ρ_{sheet}. The sheet electron density profile is then obtained as a smooth function that, starting from the edge of the 2DES, increase towards the bulk. In (b) instead a magnetic field is considered, affecting the system through the formation of quantized LLs. As a consequence, also $D(\varepsilon)$ is discrete and μ^{ch} becomes a step-like function

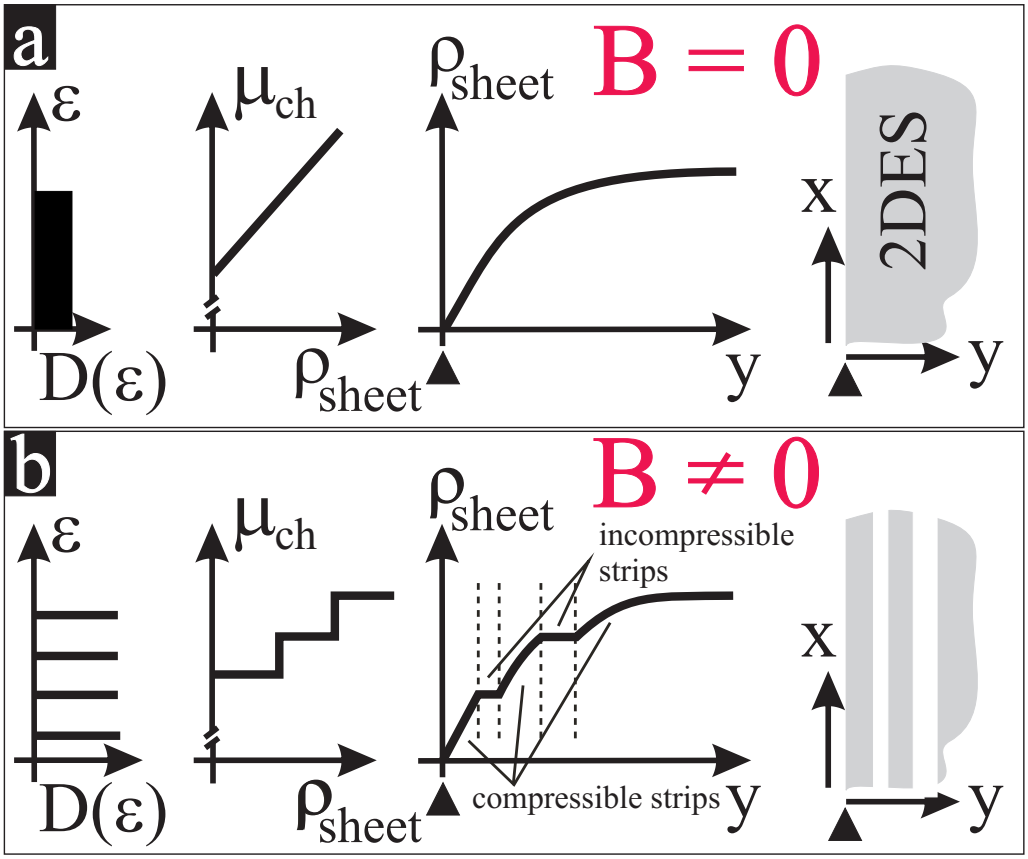

Figure 2.13: Schematic diagrams of the density of states $D(\varepsilon)$, the chemical potential $\mu^{\text{ch}}(\rho_{\text{sheet}})$ and the electron sheet density $\rho_{\text{sheet}}(y)$. In (a) there is the case of zero magnetic field; in (b) the ones for B-field applied perpendicularly to the 2DES (*From* [26]).

with ρ_{sheet}, since it follows the filling of the LLs by the electrons. Finally, the electron density profile is no longer a smooth function, but it also shows regions of constant electron density.

Let us now consider the compressibility, defined as $\kappa = \left(\frac{\partial \mu^{\text{ch}}}{\partial \rho_{\text{sheet}}}\right)^{-1}$. As long as a LL has to be filled , μ^{ch} is constant; however, when a LL is completely filled, there is a discontinuous increase in μ^{ch}, with further increasing ρ_{sheet}. This implies that $\frac{\partial \mu^{\text{ch}}}{\partial \rho_{\text{sheet}}} \to \infty$ and the system is said to be incompressible ($\kappa \to 0$), whereas before it was behaving as compressible ($\kappa > 0$). As shown in Fig. 2.13b, applying a magnetic field then plateaus in the ρ_{sheet} vs. $\vec{r}$ plot indicate the formation of incompressible strips, that separate the compressible regions from each other.

"Dot-in-dot" structure

Coming back to the QD system, we expect for a dot of arbitrary shape the formation of compressible and incompressible strips along its edges, that close themselves into loops, like shown in Fig. 2.14. Since the extension of the electron wavefunctions is proportional to l_B, it becomes smaller with increasing magnetic field. For this reason, if the incompressible strip is extended enough, the overlap between the wavefunctions of electrons in the inner part of the dot and the ones in the outer part is small. The two compressible regions are then almost isolated from each other, forming a so-called "dot-in-dot" structure, where the inner dot is coupled only capacitively to the leads and transport occurs mainly through the outer ring.

The formation of this "dot-in-dot" structure was demonstrated through several experiments, like in [23], [27] or in [28]. Measuring the CBO peak position in gate voltage as a function of the magnetic field, a zig-zag behavior appears (see Fig. 2.15a). This was explained through a redistribution of electrons between the inner and the outer parts of the dot, like sketched in Fig. 2.15b. The electronic transport through the QD system is regulated by the following steps ([23]):

- Increasing the magnetic field, the cyclotron orbit of the electrons shrinks, so that more electrons can fit in the same LL and then the LLs degeneracy also increases.

- As consequence, electrons have to redistribute from the a higher to a lower LL.

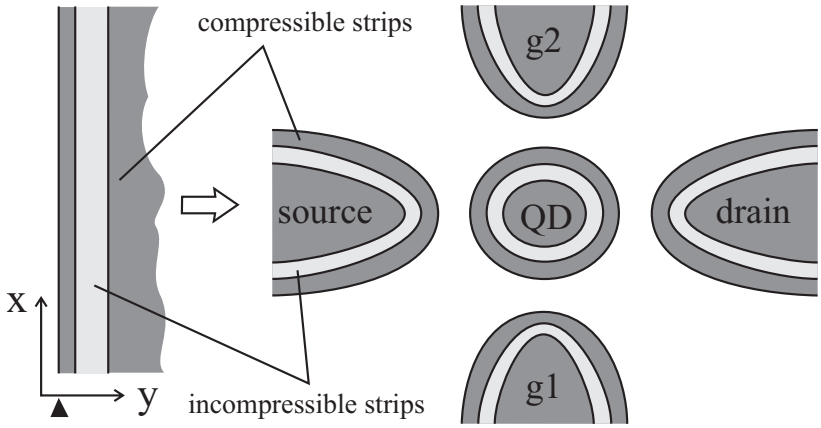

Figure 2.14: Formation of compressible and incompressible strips. On the left side the edge of the 2DES is sketched, where the black triangle points the edge position. On the right side, a QD system, where the strips inside the QD close themselves into loops.

- Additionally, the 2DES in the dot shrinks, increasing the electron-electron interaction.

- In order to minimize the total energy of the system, for certain values of the B-field, electrons from the center move to the edge region.

Depending then on the different electron configuration of the system, the transport can occur in several ways.
Let us consider a situation around filling factor $\nu = 2$, based on the McEuen model as sketched in Fig. 2.12b: In Fig. 2.15b, through the line marked (1), from a configuration with $N_\uparrow$ electrons in the inner compressible region and $N_\downarrow$ electrons in the outer one, the system move to a $(N_\uparrow + 1, N_\downarrow)$ configuration. An electron can then pass through the dot via the outer compressible ring.
Through the line marked (2), the system move from a $(N_\uparrow, N_\downarrow)$ to a $(N_\uparrow, N_\downarrow + 1)$ configuration and, in principle, the transport occurs via the inner region. However, since the tunnel coupling between the leads and the inner region of the dot is really weak, this kind of transition is strongly suppressed.
Finally, the case marked (3) shown the internal rearrangement between LLs of the dot.
At small bias voltage, Single-Electron Transport occurs along the zig-zag-like line in Fig. 2.15, depending on the energetically favorable charge configuration.

The formation of the "dot-in-dot" structure plays a crucial role also in our

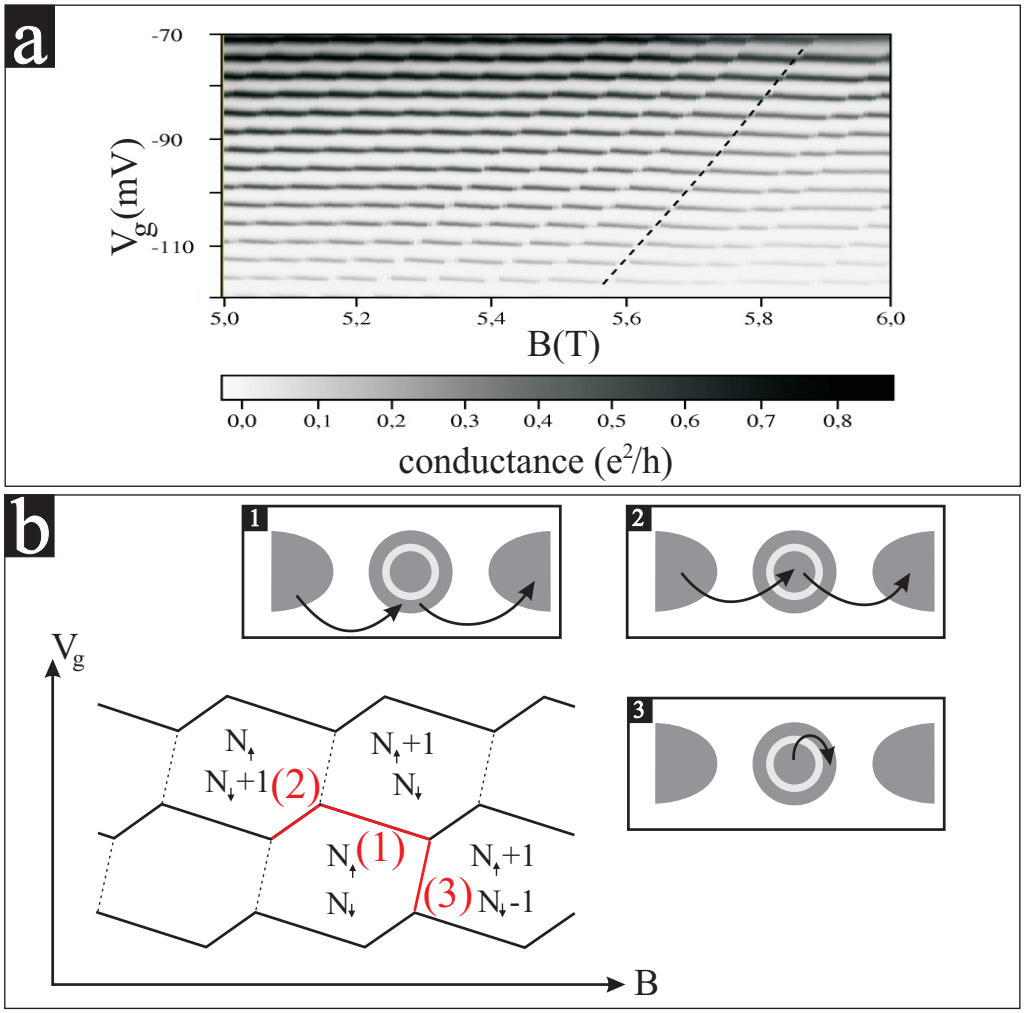

Figure 2.15: (a) CBO peak position in gate voltage as a function of the magnetic field (*From* [1]). (b) Sketch of the charge redistribution between LLs in the dot, leading to the zig-zag-like shift of the CBO peaks position seen in (a).

experiment, as we will see in the following, and it will be the key component to describe the internal electron configuration for our system and, in its turn, the transport through it.

With the measurements shown in this Chapter, the QD system under our investigation has been completely characterized.
The background theory that will guide us through the interpretation of the measurements in the following of this thesis has also been discussed.

Chapter 3

Magnetotransport through the quantum dot system from weak to strong coupling regime

In this Chapter, magnetotransport measurements on the QD system characterized in the previous Chapters are discussed.
We did observe that, applying a constant perpendicular magnetic field and increasing the coupling between leads and island, the system can be tuned through a surprisingly wide range of internal electron configurations, each one of them characterized by its own peculiar electrical transport properties.

3.1 The filling factor $\nu_{2\mathrm{DES}}$ of the 2DES forming the QD system

As described in Chapter 1.2.1, the QD system here under analysis has some design peculiarities:

- it is an in-plane structure obtained via etching through the heterostructure, where parts of the original 2DES are used as lateral gates, source and drain leads and island itself (see Fig. 1.3c), and

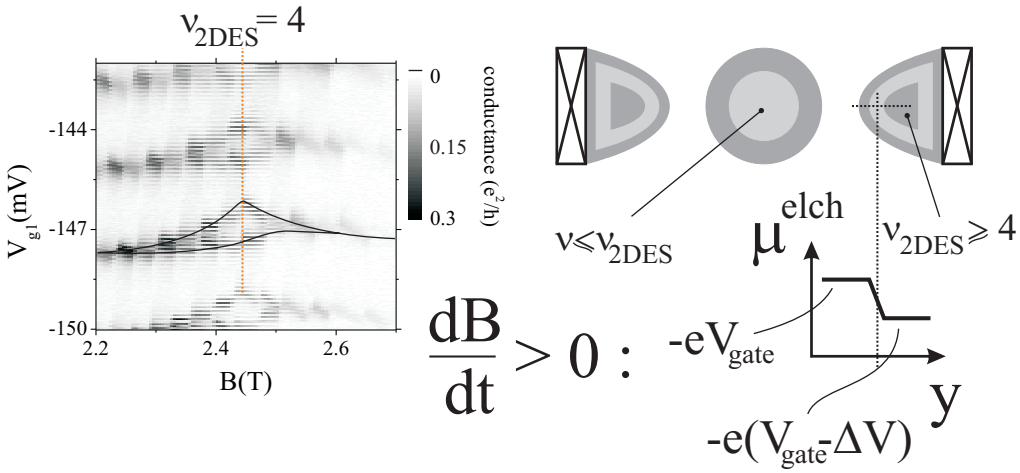

Figure 3.1: From the left: Conductance as a function of the gate voltages and of the magnetic field; sketch of the contacted QD system where compressible and incompressible strips are formed and of its corresponding electrochemical potential profile.

- the geometrical extension of the island is rather large, allowing to consider it as a small 2DES itself, where for an applied magnetic field compressible and incompressible strips can form along the whole structure.

In order to have all the ingredients for a complete description of the internal configuration of the system, it is therefore necessary to be able to extract the filling factor value ν_{2DES} for the 2DES forming the QD system.
As pointed out by Keller in [1], it is possible to link the actual value of ν_{2DES} to the presence of an hysteresis of the conductance peak position of the Coulomb Blockade Oscillations in a certain B-field range, i.e. when the 2DES is in the Quantum Hall regime.
This behavior can be explained on the basis of experiments made by Hüls *et al.* [29] using a Single Electron Transistor (SET) as a highly sensitive electrometer on the top of the bulk region of the 2DES:

- According to Faraday's law,

$$\oint \vec{E}_{\mathrm{ind}} \cdot d\vec{r} = -\int_A \frac{d\vec{B}}{dt}\, d\vec{A}\,, \tag{3.1}$$

  a varying magnetic field induces a circulating electric field $\vec{E}_{\mathrm{ind}}$ and, in turn, a Hall current $j^{\mathrm{Hall}} = \nu \dfrac{e^2}{h} E_{\mathrm{ind}}$, given by the local filling factor ν, arises in the 2DES perpendicularly to $\vec{E}_{\mathrm{ind}}$.

- Because of j^{Hall}, the charges in the 2DES move from the center towards the edge regions, creating a voltage difference (electrochemical potential difference) between the inner and the outer part.

- Finally, this voltage difference acts as a Hall voltage, $dV^{\mathrm{Hall}}_{\mathrm{eddy}}$, driving an eddy current density j_{eddy} in a loop along the border of the system.

The case of our QD system is sketched in Fig. 3.1: on the left side, the CBOs measured as a function of B-field are shown. As sketched next to the measurements, the compressible edges are directly connected to the contacts of the sample, so that μ^{elch} is fixed along the 2DES edge (at least immediately after $\frac{d\vec{B}}{dt} = 0$). The inner incompressible regions instead have a varying μ^{elch} because of $dV^{\mathrm{Hall}}_{\mathrm{eddy}}$. This electrochemical potential variations are detected by the QD through the capacitively coupling between the dot and the inner region of the 2DES. The sign of the variation of the B-field in fact determines the direction of the circulating current and then also the sign of the difference in voltage between border and inner region of the 2DES. Therefore it affects the gate voltage position of the CBO peaks, leading to the hysteresis effect. Note that this effect occurs only around integer filling factors, since only then an incompressible (i.e. insulating) loop along the border of the 2DES exists and the potential difference can arise.
Finally, let us point out that, since the value of the filling factor depends on the local electron density, one could expect that the filling factor of the 2DES forming the dot, due to electrostatic depletion, is not necessary the same of that of the surrounding 2DES, i.e. $\nu_{\mathrm{dot}} \leq \nu_{\mathrm{2DES}}$.

3.2 Antidot quantum systems

Before starting with the analysis of the magnetotransport through our QD system from weak to strong coupling regimes, let us consider a case that present some interesting common elements: the one of **quantum antidot systems**.

A scanning electron micrograph (from [30]) of such an antidot system is shown on the left side of Fig. 3.2a, with also some details about the experimental setup. The zoom in of the antidot region explain the working principle of the structure: applying a voltage to the antidot gate $V_{\mathrm{G_{ad}}}$, a depletion is formed in the 2DES. The current that flows through the constrictions so formed is regulated by the voltages applied to the side gates V_{G1} and V_{G2}. To avoid the effect of the series resistance of the ohmic contacts, a four-point configuration is used in the measurements: a modulated voltage is injected

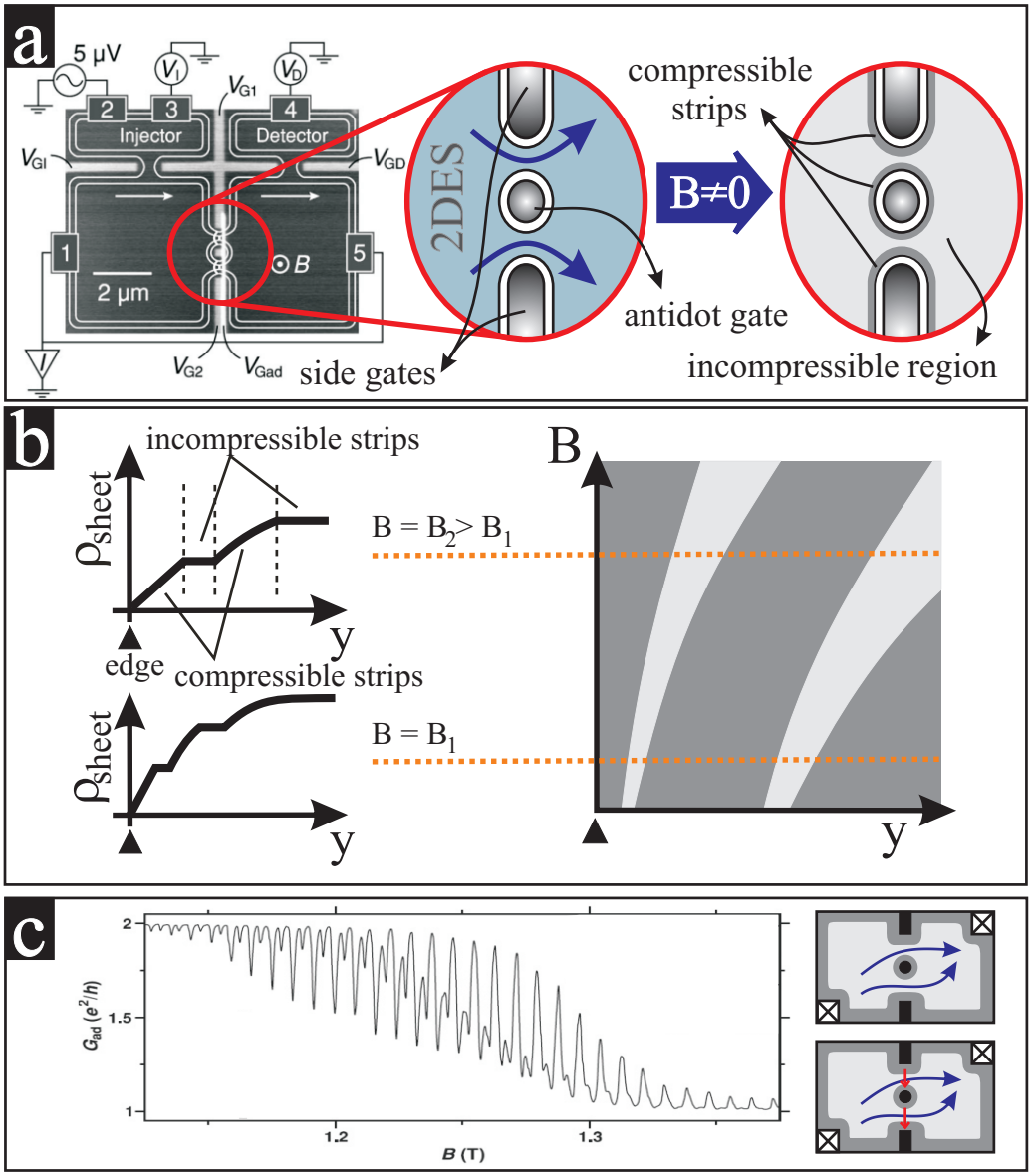

Figure 3.2: (a) On the left: SEM image of a quantum antidot system from [30]; the setup for a four-point measurements is also shown. In the center: zoom into the active region in which the antidot is formed by applying a voltage to the antidot and the side gates. On the right: the same region for the case $B \neq 0$, where compressible strips run all around the incompressible region. (b) Schematics of the evolution of the compressible and incompressible regions with increasing B-field. (c) Conductance through the antidot constrictions vs. B (from [31]). On the right: drawings explaining the backscattering process.

into the 2DES and both the current and the voltage drop through the constrictions around the antidot are detected.
The switching on of the magnetic field, as previously discussed, leads to the formation of compressible and incompressible strips all along the borders of the 2DES, that behave respectively metallic and insulating. In particular (see right side of Fig. 3.2a), compressible strips run around the side gates and the antidot gate, where they close into a loop that confines electrons at the antidot site. The insulating incompressible region in the bulk of the constrictions acts as a tunnel barrier between the compressible strips around the side gates (- leads) and the one around the antidot (- island).
In Fig. 3.2b the evolution of the compressible and incompressible regions as a function of the magnetic field is sketched. From the schematic diagrams of the electron sheet densities as a function of the position in the bulk for different magnetic field values, we can see that, at a field $B = B_2 > B_1$, the ρ_{sheet} curve changes in a more elongated shape, where the plateaus of the incompressible regions are wider and placed at higher y positions. As calculated in [25] and summarized in the sketch on the right side of Fig. 3.2b, for increasing B-field, the compressible strips move towards the inner part of the 2DES and become also wider.
As theoretically discussed by Davies [32] and proved by the scanning force microscopy investigations carried out by Weitz, Ahlswede and Dahlem [33, 34, 35], whenever a magnetic field is applied to a 2DES, the Hall voltage V_{H} builds up transversally to the sample and it leads to a current flowing orthogonal to V_{H} along the incompressible bulk.
The direct consequence of these considerations can be observed in the measurements of Fig. 3.2c (from [31]):

- On the left side of the G_{ad} vs. B plot, the current flows through the constrictions, in the incompressible bulk region for which $\nu_{\text{2DES}} = 2$, as described by the upper sketch at the side of the measurements. The lower sketch refers to the situation of an electron tunneling between compressible strips, resulting in a re-equilibration among them and therefore to a local decrease of the Hall voltage through the constrictions, detected in the measurements as a dip in the conductance. This re-equilibration process is also known in literature as backscattering.

- For higher B-field values (right side of the measurements), the compressible strips have moved towards the center of the constrictions, leading to a stronger coupling between the metallic strips around the side gates and the one around the antidot. The minima of the conductance therefore become more pronounced until merging in the $\nu_c = 1$ plateau with conductance e^2/h.

3.3 Coulomb Blockade Oscillations at filling factor $\nu_{2\mathrm{DES}} = 2$

In the measurements carried out on our system, an external magnetic field of 5 Tesla was applied perpendicularly to the in-plane structure and the conductance was measured as a function of both the gate voltages, tuning the coupling strength between the island and the source and drain leads.
The result is shown in Fig. 3.3: here one can see that, depending on the strength of the coupling between the leads and the island, the conductance trace follows a smooth transition from a Coulomb Blockade regime (on the left side of the gate voltage axis, for weak coupling conditions) to a regime in which it has an almost constant value of about e^2/h (on the right side of the gate voltage axis, for a strong coupling regime). One should note at this point that the value reached by the differential conductance in the plateau is slightly lower than the expected e^2/h; this can be explained taking into account that the measured conductance also includes resistances in series between the sample itself and the rest of the electronic setup.
This peculiar behavior of the conductance through the quantum dot system is strictly dependent on the value of the external magnetic field applied; it is in fact observed only for magnetic field values corresponding to integer Landau level filling factors $\nu_{2\mathrm{DES}}$ for the 2DES constituting the in-plane structure.
The value of e^2/h reached by the conductance for the strong coupling regime leads us to consider that a spin-polarized current is flowing through the system. The formation of a direct one-dimensional channel from the source to the drain along which transport could occur was observed and discussed by different groups during the past years [28, 36, 37, 38, 39, 40]. The model proposed to explain these experiments was based on a single-particle picture:

- Due to the electrostatic confining potential present at the etched grooves, the whole energy band structure of the 2DES is bent at its edge.
- Consequentially, the Landau levels are also bent and therefore they cross the Fermi energy.
- Finally, this leads to the formation of the so-called circulating edge states: Electrons with different LL index n and spin orientation move along different equipotential lines.

In the case of a QD weakly coupled to its surroundings, these equipotential lines would be located along the border of the 2DES forming the leads of the QD system and along the border of the island; the transport between different edge states could occur via tunneling. In the case of a stronger

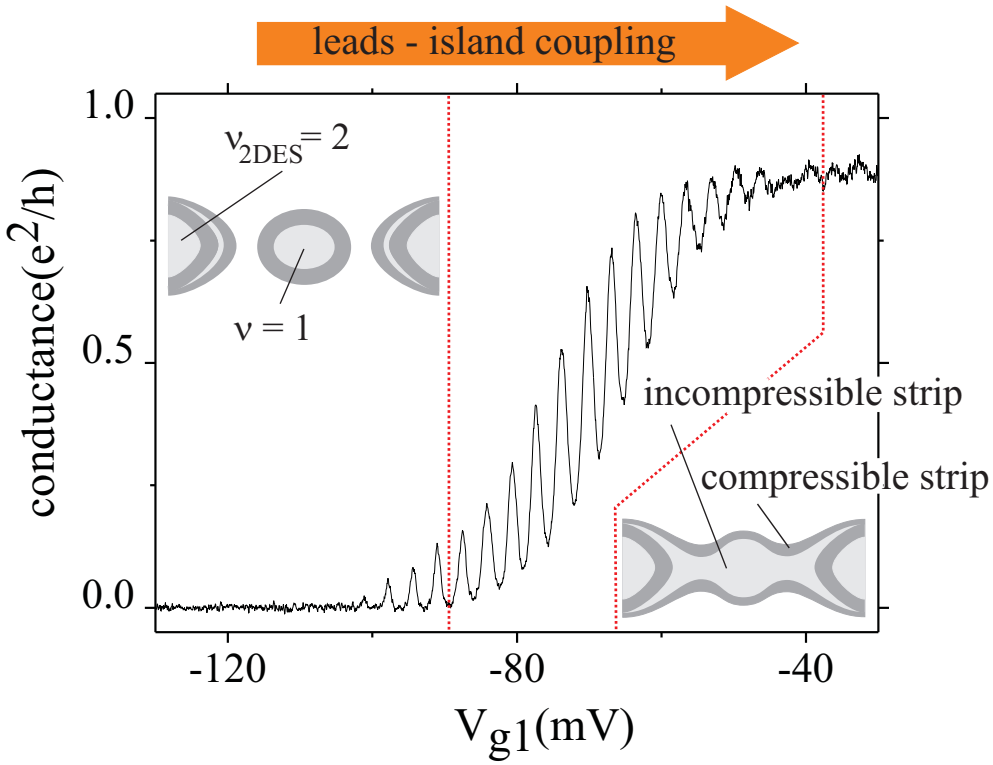

Figure 3.3: Conductance plotted as a function of gate voltages for Landau level filling factor $\nu_{2DES} = 2$; the strength of the coupling between leads and island increases moving towards positive values on the V_{gi}-axis. In the inset, sketches of the internal electronic configurations due to the applied B-field for weak and strong coupling conditions.

coupling between the leads and the QD, the more external edge states in the leads are then overlapping with the ones of the island, forming a direct one-dimensional channel from the source to the drain lead along which transport occurs.
Even if the circulating edge states model itself cannot be accepted because it doesn't take into any account the electron-electron interactions, we can still apply the general idea of a direct channel forming through our system. In the case of our measurements, in fact, the presence of the external B-field results in the appearance of compressible and incompressible strips. As sketched in the inset on the top-left of Fig. 3.3 for weak coupling conditions, compressible strips run along the whole structure of leads and island; transport occurs via single-electron tunneling from the leads to the isolated QD. In the bottom-right inset, the internal electronic configuration is sketched for the strong coupling condition; the outer compressible strip in the leads overlaps with the one of the QD and the incompressible strip corresponding to $\nu = 1$ extends over the dot region. From the value reached by the conductance for this last case, we can infer that a spin-polarized current is flowing directly from source and drain leads within this incompressible bulk region, driven by the electrochemical potential difference between the compressible edge regions.
For the internal structure of the island there is another possibility: Encircled by the compressible border there is an incompressible strips and at the center of the bulk an additional compressible region, i.e. $1 < \nu < 2$. Since in the present case this inner compressible region does not play any measurable role, i.e. it is completely isolated from its surrounding, this configuration is not distinguishable from that where the core region is purely incompressible, i.e. $\nu = 1$.

3.4 Coulomb Blockade Oscillations at filling factor $\nu_{\mathrm{2DES}} = 4$

To obtain Landau level filling factor $\nu_{\mathrm{2DES}} = 4$ for the 2DES forming the QD system so to have, at least, $\nu > 2$ inside the island, the magnetic field had afterwards been decreased to a value of 2.5 Tesla. The result is shown in Fig. 3.4, where the conductance is plotted as a function of both gate voltages. Similarly to the case previously described of $\nu_{\mathrm{2DES}} = 2$, also here increasing the strength of the coupling between the dot and the leads, the transition from a Coulomb Blockade regime to a constant conductance plateau is clearly observed in the data. Nevertheless, some differences with respect to Fig. 3.3

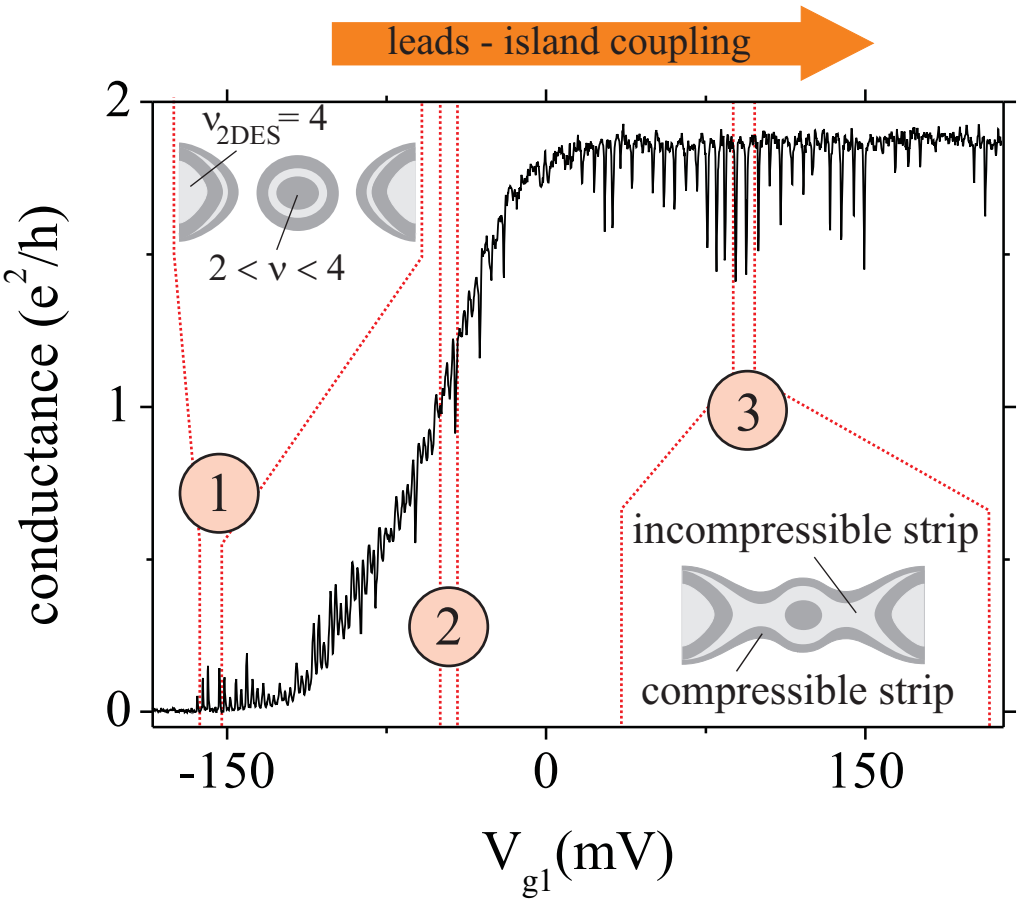

Figure 3.4: Conductance plotted as a function of gate voltages for 2LL; the strength of the coupling between leads and island increases moving towards positive values on the V_{gi}-axis. In the inset, sketches of the internal electronic configurations due to the applied B-field for weak and strong coupling conditions.

can be highlighted:

- The plateau in the conductance in the strong coupling regime now occurs for $2e^2/h$: the current flowing through the system is now within the $\nu = 2$ incompressible strip.

- Unlike on the plateau formed at $\nu_{\mathrm{2DES}} = 2$ where only a faint oscillation was detected without a well defined structure, here in the strong coupling regime sharply pronounced dips appear.

Even if the mechanisms that drive the transport through the system have definitely some analogies in the two different electronic configuration defined by the magnetic fields, there are in the case of $\nu_{\mathrm{2DES}} = 4$ some further points to be considered.
The transition between the weak and the strong coupling regimes is therefore further analyzed via measurements of the differential conductance as a function of V_{sd} and V_{G}.

The weak coupling regime

In Fig. 3.5a the conductance is plotted on grey scale as a function of both the lateral gate voltages $V_{\mathrm{g}i}$ and the bias voltage V_{sd} applied between source and drain leads. The gate voltages are swept following the same trace of the previous data, corresponding to the interval marked as (1) in Fig. 3.4.
A clear Coulomb Blockade diamond-shaped pattern arises from the measurements: transport takes therefore place only via single-electron tunneling for this weak coupling regime ($E_C \approx 0.5$ meV). This situation is already well established by previous experiments (see, for example, Fig. 2.15), demonstrating that transport can occur in several ways: an electron can pass through the dot via the outer compressible ring, via the inner region (even if, due to the weakness of the coupling between the leads and the center of the island, the probability for this transition is strongly suppressed), or an internal rearrangement between LLs of the dot can take place in order to minimize the total energy of the system. In Fig. 3.5b a line cut along the $V_{\mathrm{sd}} = 0$ axis is shown and in Fig. 3.5c there is a cut perpendicular to the gate voltages axis, highlighting the sharpness and the height of the Coulomb Blockade peaks.
In the plotted charge stability diagram, the presence of excited states taking active part in the transport can also be detected from sharp conductance peaks in the single-electron tunneling regions. This additional feature is a further proof of the fact that the system, even if divided in compressible and incompressible regions, behaves as a quantum dot.

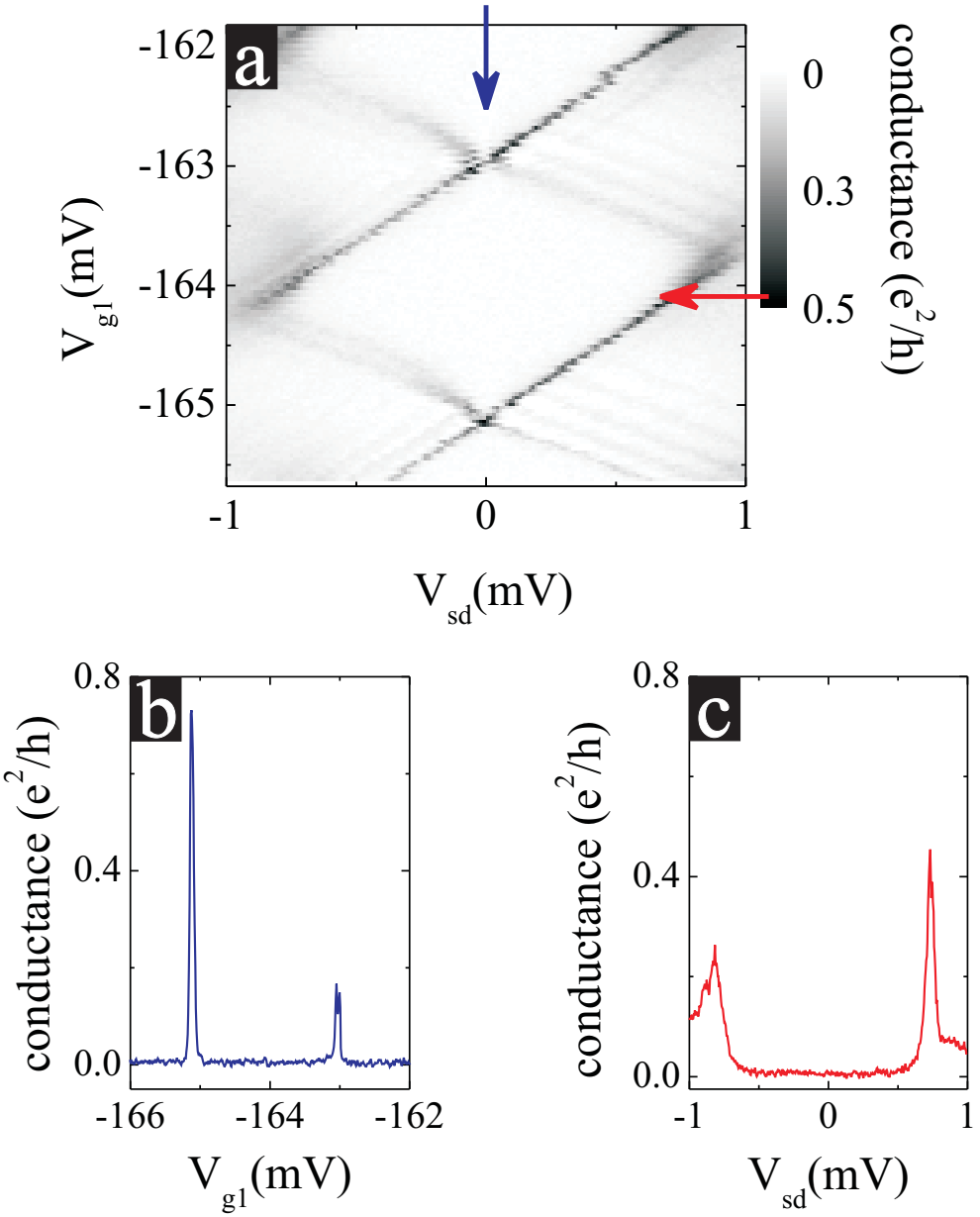

Figure 3.5: (a) Differential conductance measured as a function of the source-drain and of a gate voltage trace; the intensity of the conductance is plotted on the grey scale. The gate voltage trace is the one marked as (1) in Fig. 3.4. Line cuts through the charge stability diagram corresponding respectively to the blue arrow (b) and to the red one (c).

The strong coupling regime

The coupling between the quantum dot and the leads was afterwards increased up to the range marked as (3) in Fig. 3.4 and once again the differential conductance as a function of V_{sd} and V_G was measured. The result is shown in Fig. 3.6a: the expected Coulomb diamond-shaped pattern is now completely reversed and, instead of having its borders defined by single-electron tunneling peaks, it is defined by deep and sharp minima, as can be clearly seen from the line cuts in Fig. 3.6b and c.
It seems to have similarities to the data of Göres *et al.*, where the interpretation was based on the Fano effect. However, here the origin is different: According to the compressible and incompressible strips model, for such a strong tunnel coupling configuration, the internal electronic structure can be described as it follows:

- The outer compressible borders of the leads and of the island overlap completely, the current flowing through the system is now within the $\nu = 2$ incompressible bulk region and therefore $G \approx 2\frac{e^2}{h}$.

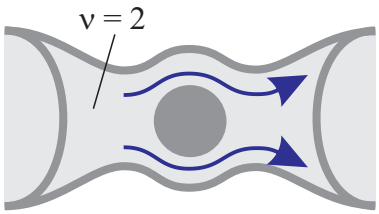

- Inside the QD an isolated compressible droplet is left; electrons scattering between the compressible border and the inner droplet can lead to a local decrease of the Hall voltage in that area

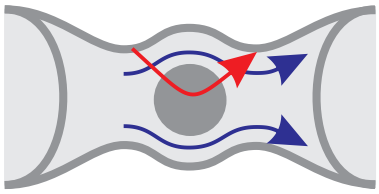

and therefore to a decrease in the locally transmitted current. Such a possibility is very close to the prerequisites analyzed in Chapter 2.5 for the occurrence of the Fano effect, characterized by an asymmetrical modification of the Coulomb Blockade Oscillations peaks. From Fig. 2.11b, among the possible lineshapes calculated for different values of the asymmetry parameter q, the case of a symmetrical dip was related to a unitary ratio between the transmission amplitudes of the resonant and the non-resonant paths. Nevertheless, such an explanation is not completely convincing, since it would be very peculiar to observe, as in the present case, that the factor q is always equal to

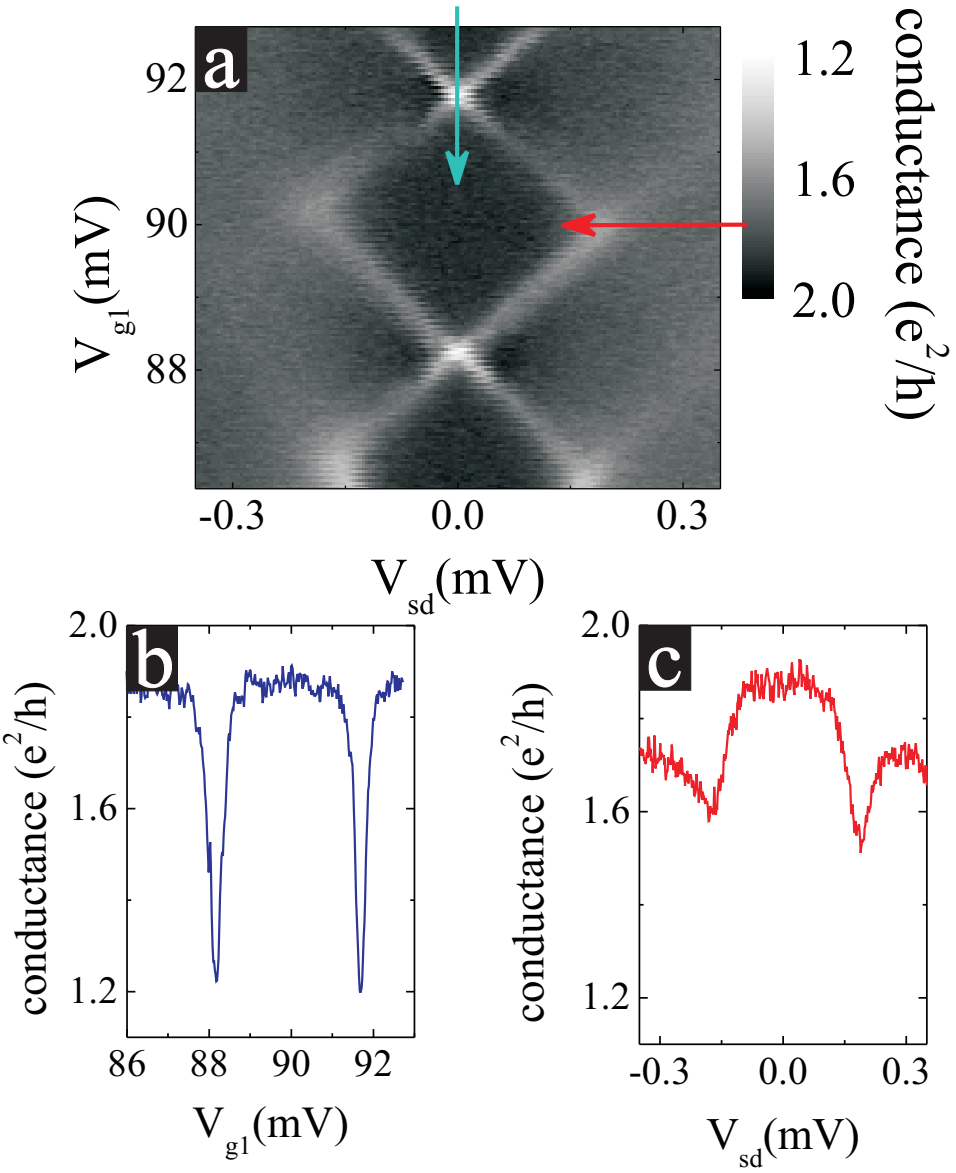

Figure 3.6: Charge stability diagram for the strong coupling regime, corresponding to the interval marked as (3) in Fig. 3.4; on the colorbar, dark grey stands for high conductance. Line cuts of the measurements along the blue (b) and the red (c) arrows are also shown.

the unity. Furthermore, a local decrease of the portion of the current transmitted through one side of the QD region could be re-equilibrated by that flowing through the other side, leaving unaffected the total transmitted current.

- Sharp symmetrical dips superimposed to a finite value for the conductance were also observed in the electron transport through quantum antidot systems, as discussed earlier in this Chapter;

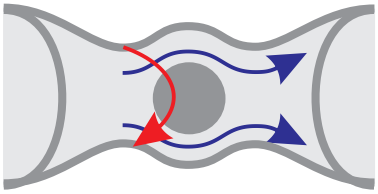

in that case they were explained via the backscattering of charges between compressible strips with opposite chirality running close to each other. Also this configuration could indeed be possible in our system, in correspondence of the constrictions of the tunnel barriers, prospecting a more convincing explanation of the conductance lineshapes.

A very striking aspect of the conductance in strong coupling regimes that we have been measuring is the reproducibility and the robustness of this reversed diamond-shaped pattern. In some cases we could also observe sharp minima located parallel to the borderlines of this diamond-shaped regions, in a fashion that resembles the conductance peaks due to transport via excited states for a weak coupling regimes (see Appendix B, Fig. B.3).

The intermediate coupling regime

In the last part of this Section, the intermediated coupling regime is described: Fig. 3.7a shows the differential conductance as a function of gates and source-drain voltages for the range marked as (2) in Fig. 3.4. The corresponding line cuts are displayed below in (b) and (c).
At first, one can notice that the whole contour of the diamond-shaped regions is smeared out and that the background conductance in the Coulomb Blockade regions is no longer equal to zero, but is already increasing towards the value of $2e^2/h$.
Considering the possible internal electron configuration due to the applied magnetic field and to the increase of the coupling strength with respect to the situation of the parameter range of Fig. 3.5, one can infer that in the system a direct channel is almost formed because of the overlapping between

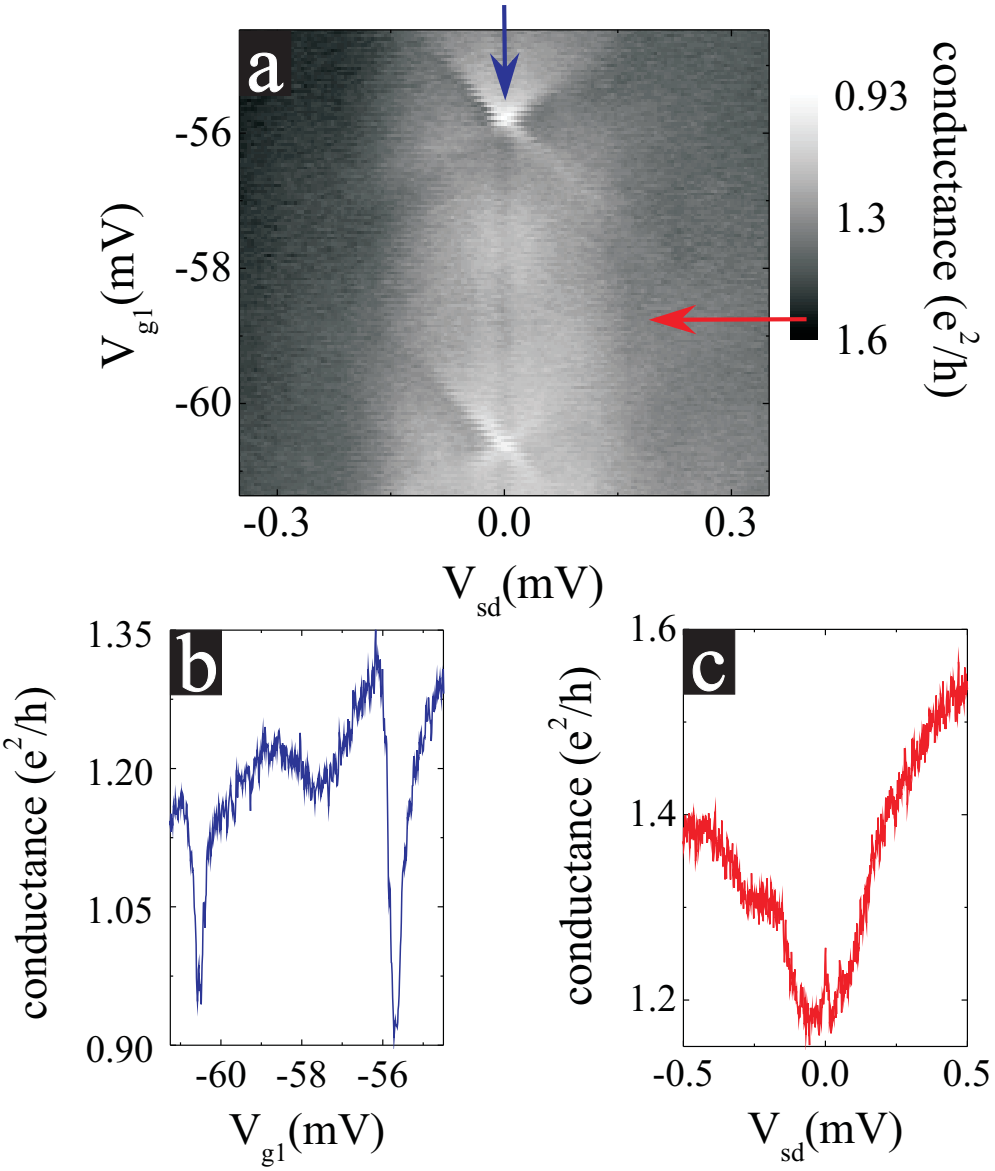

Figure 3.7: (a) Differential conductance measured as a function of the source-drain and of the gates voltages for the gates voltages range is the one marked as (2) in Fig. 3.4. Line cuts through the charge stability diagram corresponding respectively to the blue arrow (b) and to the red one (c).

the compressible border in the island and the ones in the leads. The observation of sharp minima, analogous to that reported for the strong coupling regime and there associated to backscattering events, support the modeling of the internal electron configuration with an incompressible bulk region that extends though the whole system and where current flows.
Secondly, here an additional feature appears in the the center of the Coulomb Blockaded region as a zero-bias anomaly.
The nature of this sharp enhanced transport in the $V_{\mathrm{sd}} \approx 0$ region can be understood via the analysis of CBOs traces measured as a function of varying magnetic field, as shown in Fig. 3.8. Here the transport is enhanced and suppressed following a highly regular trend, known in literature as the checkerboard pattern. Such a behavior had been reported as first by Keller *et al.* in [41] and explained referring to the Kondo effect, a phenomenon that, as mentioned in Chapter 2.5, involves correlated tunneling of many electrons due to the formation of a many-body state. Following the description given in [41], the origin of the Kondo feature is linked to the internal electronic structure on the island arising from the externally applied magnetic field. In Fig. 3.8a, an odd number of electrons is present on the core of the island; by increasing the voltage applied to the gates, an additional electron enters into the island, positioning itself on the peripherical region of the dot (Fig. 3.8b), where then it will be spin unpaired. Replacing this latter electron with an other of opposite spin orientation would cost just the Zeeman energy; the spin degeneracy in the dot is therefore lifted, allowing the occurrence of the Kondo effect, that is detected in the measurements by an increase of the conductance in the otherwise Coulomb blockaded region. By further increasing the gate voltage, an other additional electron enters into the outer region of the system, so to pair up the spin state of the outer compressible ring (Fig. 3.8c). According to the internal re-arrangement as described in Fig. 2.15, by increasing the magnetic field, to minimize their Coulomb repulsion, an electron from the core moves to the peripherical ring of the dot (Fig. 3.8d): once again on the outer ring there is an electron with unpaired spin and therefore Kondo effect can occur.
In the case discussed in [41], the checkerboard pattern was measured while applying a bias voltage V_{sd}: this was done because, as seen also in Fig. 2.10b, an applied magnetic field leads to the Zeeman splitting of the zero-bias anomaly. Quite surprisingly in our case though, even if there was an applied B-field, the zero-bias anomaly was not split and therefore the measurements in Fig. 3.8 were performed at $V_{\mathrm{sd}} = 0$.
An other relevant difference between previous and our measurements is the coupling regime in which they are taken: Unlike what previously observed, here we are in a regime of significantly stronger coupling between leads and

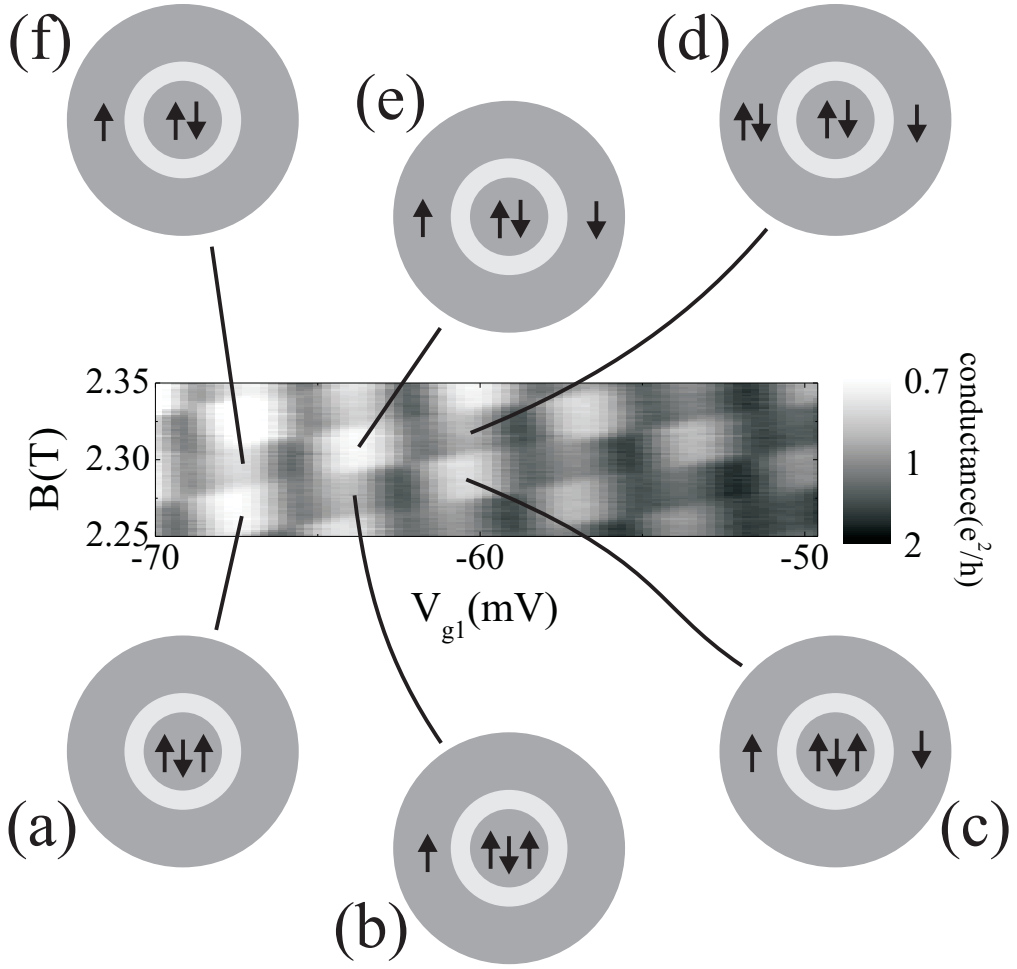

Figure 3.8: Differential conductance measured as a function of the gates voltages and of the magnetic field: the highly regular checkerboard pattern is visible. As a try, the pattern is explained referring to the different electron configurations through which the QD moves depending on the sweeping parameters.

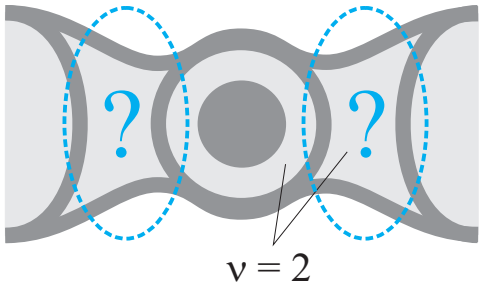

Figure 3.9: Sketch of the different possible internal electron configurations for the regime of intermediate coupling between island and leads: the direct channel, across which electron backscattering can occur, coexist with the situation for which electrons are still localized on the island, giving rise to the observation of the Kondo effect.

island, where, as aforementioned, transport should occur directly from source to drain leads via the incompressible bulk. This configuration would imply though that the Kondo effect would lead to an anomalous backscattering enhancement within the Coulomb blockaded region, i.e. to the observation of a zero-bias minima. In our case, on the contrary, the zero-bias anomaly is shaped as a peak, clear indication of forward and not back- scattering.
For these reasons, it is still not clear what is the exact internal electron configuration of our QD system in the intermediate coupling regime, as highlighted in Fig. 3.9.

Since one of the requisites for which the Kondo effect manifests itself is the existence of a spin-degenerate state in the quantum dot and the presence of electrons of both spin orientations in the leads, from our measurements one can therefore infer that, in the present parameters range, the compressible edge regions of the leads are not (fully) spin polarized.

3.5 Conclusion

Electrical transport measurements through a large quantum dot were performed, showing a remarkably high degree of tunability between different internal configurations. On the same sample and for the same cooling down process, it was possible to observed several transport regimes, tuning only the constant magnetic field applied perpendicularly to the system and the strength of the coupling between the island and the leads. Each one of these regimes could give us insights on the internal electron configuration of the whole system under analysis.

As summarized in the sketches of Fig. 3.10, depending on the applied magnetic field, two different LL filling factors for the 2DES at the basis of the QD system could be obtained.

- For $\nu_{2\mathrm{DES}} = 2$, a compressible border runs along the whole leads structure, encircling an incompressible bulk where the filling factor is equal to 2; due to an electron concentration presumingly different, in the dot region one could instead have $\nu < \nu_{2\mathrm{DES}}$.
  Whenever the coupling between leads and island is increased by tuning the voltages applied to the gates, the outer compressible borders of leads and dot overlap: transport takes place within the inner bulk region, where a spin-polarized current flows up to a value of almost e^2/h.
  For the internal structure of the island two different possibilities had been considered: Encircled by the compressible border there is an incompressible strips and at the center of the bulk an additional compressible region, i.e. $1 < \nu < 2$. Since the presence of an inner compressible region at the center of the QD system would lead to the observation of backscattering events that we did not detect in our measurements, we could finally conclude that at the center of the dot system $\nu = 1$, i.e. there is only the incompressible bulk.

- For $\nu_{2\mathrm{DES}} = 4$, the presence of a compressible inner dot has been detected from the measurements, i.e. in the dot $2 < \nu < 4$. In the strong coupling regime, the presence of the dot leads to the observation of deep and sharp minima in the differential conductance, that have been related to backscattering events. An open issue is still left about the internal electron configuration in the case of intermediate coupling regime between leads and island, where it is not clear whatever transport already occurs within the inner incompressible region formed by the merging of the compressible borders, as it is indicated by the observation of backscattering features, or instead the outer compressible borders are still resolved from each other. Astonishing is the simultaneous observation of the forward scattering linked to the Kondo effect.

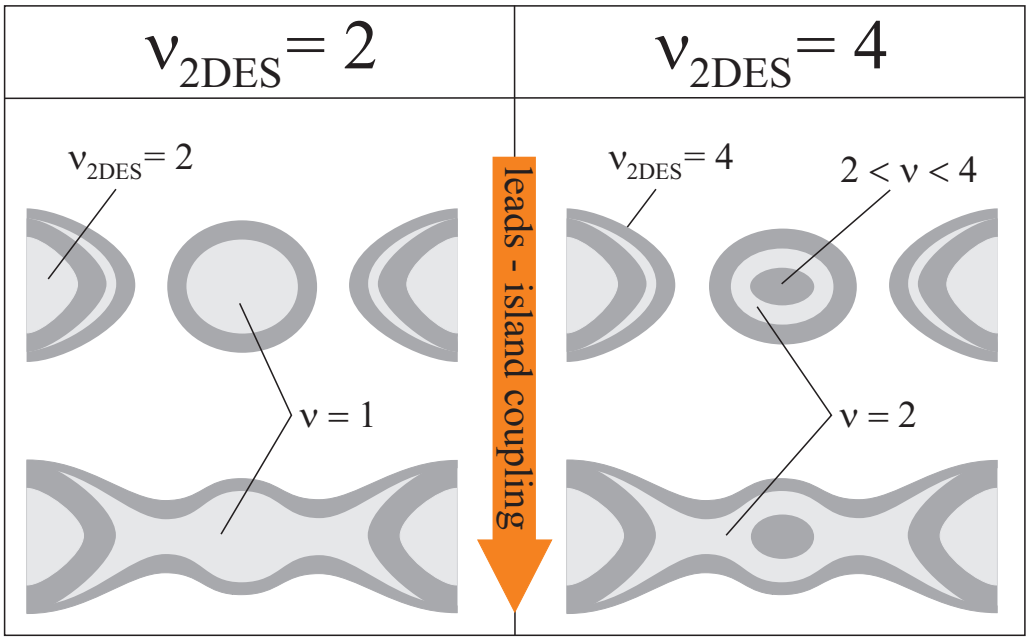

Figure 3.10: Sketches of the internal electron configuration of the measured dot as a function of both the magnetic field and the coupling between the leads and the island.

Part II

Magnetotransport in MBE-grown III-V NWs

Chapter 4

Preparation of nanowire systems

In recent years, a strong interest has developed towards nanowire systems, triggered, among other reasons, by the possibility of combining into a single device the advantages offered by both their particularly small sizes and the wide tunability obtainable via electrostatic gating.
This Chapter discusses the technologies used in this thesis for the successful growth, and subsequent nano-structuring methods of reliable, reproducible nanowire devices for use in magneto-transport at low temperature.

4.1 The growth of nanowires: the vapor-liquid-solid growth method

One-dimensional nanostructures are created by promoting the crystallization of solid state structures along one direction. Among all methods based on crystal growth from a vapor phase, the so-called vapor-liquid-solid (VLS) method seems to produce the largest quantity of wires with single-crystalline quality.
The VLS mechanism was first described by Wagner and Ellis in 1964 [42],

in a paper which discusses the epitaxial growth of gold particle induced nanowhiskers. They observed that

- silicon whiskers did not contain an axial screw dislocation,
- the presence of metal particles on the substrate turned out to be essential for the whisker growth, and
- a small globule was present on the top of the structure during its growth.

Their conclusion was that they were indeed facing a novel growth mechanism. Analyzing the VLS mechanism, we will also see how these early observations can be fully explained.

The growth of nanowires (NWs) can be divided in three phases [43], [44], [45]:

1- **The preparation of the substrate by coating it with metal nanoclusters.**
Even if these nanoclusters are almost everywhere in literature referred to as the catalysts for the growth, they are in reality better understood as collectors of material. A catalyst in fact increases the rate of a chemical reaction by reducing its activation energy while not been finally consumed by the reaction. In contrast to this definition, the VLS growth of the NWs simply does not start without the presence of the nanoclusters and, in some proportions, the metal crystallizes forming a compound with the other reactants.
For all these reasons it is therefore more correct to refer to the metal particles as accretion sites for the deposited materials. The wire growth occurs at temperatures where planar film growth is either completely hindered or it is a competing mechanism: the material of the reactants diffuses along the surface of the growth substrate towards the metal particles, that then act as traps for the material.

2- **The selected III-V semiconductor reactants are brought into the system in their vapor phase.**
The group III precursor material is incorporated into the metal droplet forming an alloy and material is added until the alloy is supersaturated. At this point, to reduce the supersaturation, the dissolved group III material will precipitate through the metal-semiconductor interface, combining with the local group V reactants: the III-V crystalline material will start forming directly underneath the metal droplet.

3- **The growth of the nanowire**.
There are two competing interfaces during the growth: the liquid-solid interface between metal-semiconductor alloy and the growing NW and the vapor-solid interface at the sidewalls between the local reactants and the NW. In the first case, the wire will grow and elongate along its axis, while through the second interface it will thicken in the radial direction.

Let us briefly consider here the kinetics of the growth, as discussed in [46]. Assuming that the metal droplet is a hemisphere of radius r identical to the radius of the wire, that R_{top} is the impingement rate of the material that directly hits the top of the wire and that R_{side} is the impingement rate at the sidewall

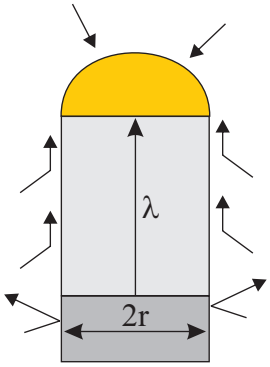

area of the wire, then the NW growth rate can be given as

$$\frac{dL}{dt} = \frac{2\pi r^2}{\pi r^2} R_{\text{top}} + \frac{2\pi r \lambda}{\pi r^2} R_{\text{side}} \,, \tag{4.1}$$

where L is the wire length. The prefactor in front of R_{top} is the surface area of the metal particle divided by the cross section of the wire, while that on front of R_{side} is the sidewall area of the wire within one diffusion length λ of the metal droplet divided once again by the wire cross section. By assuming $R = R_{\text{top}} = R_{\text{side}}$, one finally obtains that

$$\frac{dL}{dt} = 2R\left(1 + \frac{\lambda}{r}\right) . \tag{4.2}$$

The whole VLS growth process is visually summarized in Fig. 4.1:

- in (a), the substrate wafer is covered by the metal that will be the nanoclusters;

- by heating, in (b) the metal coating clusters into many droplets on the whole surface. The molecular beams of the materials that will form the chosen semiconductor to grow are injected into the growth chamber. When the eutectic conditions are reached, a metal-semiconductor or a metal-metal alloy is formed, depending on the materials.

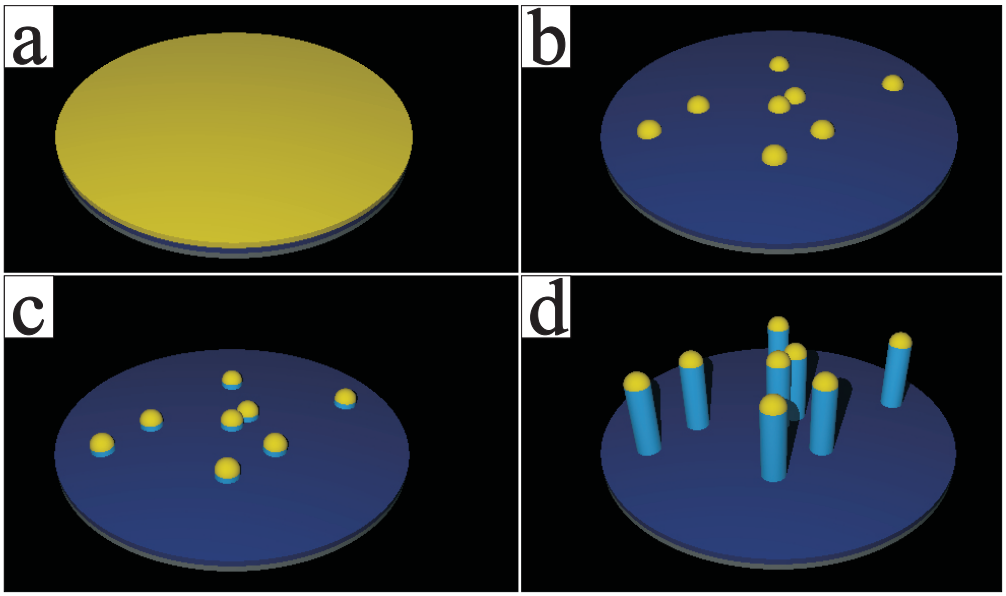

Figure 4.1: Schematic diagram of the VLS process: starting from a substrate metalized with a thin layer of the material that will induce the growth process (a), liquid droplets of the selected metal-semiconductor alloy are formed (b), from which the solid semiconductor nucleates via MBE technique (c), leading to the formation of the NWs (d).

- By continuing to feed the reactants into the liquid droplet, the alloy supersaturates, leading to the nucleation of the solid semiconductor, as shown in (c).

- The semiconductor is incorporated into the lattice through the growth interfaces and, in (d), the NWs grow from the substrate with the alloy droplet riding on the top.

Epitaxially grown III-As NWs usually have a cubic zincblende or hexagonal wurtzite crystal structure, or a combination of the two structures alternating each other [43]. Being an epitaxial process, the crystallographic structure of these wires will be dictated by the crystal structure of the substrate from which they are grown, even if, as it will be seen, growth from amorphous substrates is also possible. Beside the substrate, key roles are played by the wire material, the growth conditions (like, for example, temperature of the substrate and pressure of the growth chamber) and finally the wire diameter, dictated by the original nanocluster size.

The measured samples

The samples electrically characterized in the following part of this PhD thesis were grown at the Laboratorio Nazionale TASC-INFM-CNR in Trieste (Italy) by the group of Silvia Rubini.
As we will see, we had quite of a variety of different samples available:

- InAs nanowires, grown using gold as the nanocluster that will trigger the nucleation of the crystalline structures, and

- Be doped GaAs nanowires, grown using both gold and manganese as triggering metals.

In this Section, the details of the growth of GaAs and InAs NWs performed in Trieste will be discussed; more technical specifications about the growth process and the crystallographic analysis of the obtained wires have been published in [47], [48] and [49].
A fundamental difference between the wires measured in this work and the majority of the other wires grown via the VLS mechanism is the means through which the reactants are feed into the system. If elsewhere techniques like, for example, chemical vapor deposition (CVD) or laser-ablation are commonly used, here we preferred the Molecular Beam Epitaxy (MBE) approach. The latter, in fact, implies the use of a Ultra High Vacuum chamber for the growth, leading therefore to a minimization of the amount of oxidation/contamination in the growing structures. Furthermore, the relatively low growth temperatures prevent interdiffusion of nano-sized heterostructures. For all these reasons, we expect to have very high quality semiconductor wires.
Our GaAs NWs have therefore been grown by solid-source MBE on a SiO_2 substrate, previously heated at 300 °C for half an hour for contaminant degassing.
In a metallization chamber connected via ultra-high vacuum with the growth chamber, the metal film (either Au or Mn) was deposited on a room temperature substrate before its introduction into the growth chamber.
The wires growth parameters were:

Growth parameters	
substrate temperature for GaAs NWs	from 580 to 615°C
substrate temperature for InAs NWs	from 390 to 430°C
V/III b.e.p. ratio for GaAs at 1.0 μm/h	between 8 and 9
V/III b.e.p. ratio for InAs at 0.2 μm/h	between 22 and 26
corresponding impurity concentration	from 1 to 2×10^{19} cm^{-3}

The NWs growth lasted 30 minutes, after which the main shutter placed between sources and substrate was closed and the sample was cooled down. NWs up to 20 μm long randomly oriented covered the sample surface; the lateral dimensions were from tens to few hundreds of nanometers, showing a tapered shape. SEM images of typical samples are shown on the left sides of Fig. 4.2a and b. The growth of the nanowires showed to be very reproducible in terms of shape, density, and size, under the same growth conditions.
In Fig. 4.2a a representative High Resolution Transmission Electron Microscopy (HRTEM) image of a Au-induced GaAs NW, with diffractograms relative to the sample portions enclosed in the squares, discloses details about the structure of these type of wires. The metallic droplet is clearly seen on the top of the wire, but it is not homogeneous and shows two distinct regions:

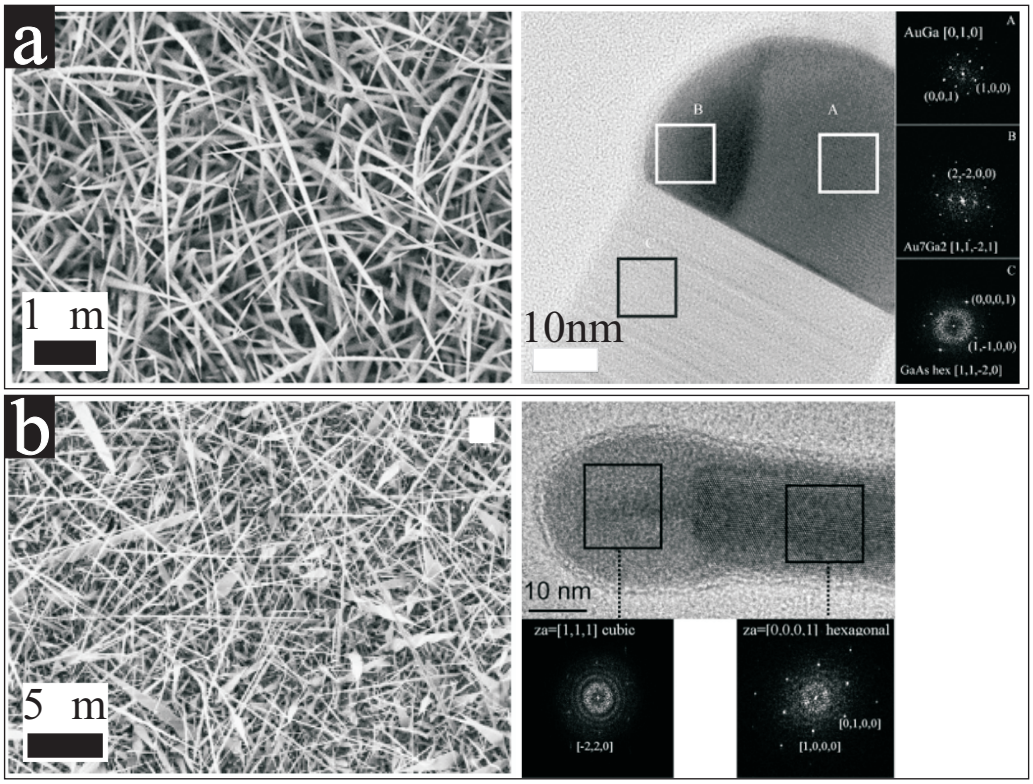

Figure 4.2: Scanning Electron Microscope (on the left) and High Resolution Transmission Electron Microscope (on the right) images of the grown GaAs nanowires: In (a) the Au-induced samples (*from* [48]), in (b) the Mn-induced ones (*from* [47])

these regions are AuGa compounds with different percentage of gold. The body of the nanowire is composed of wurzite GaAs.
A typical Mn-induced GaAs NW tip is shown in Fig. 4.2b: also in this case the nanowire body has a wurzite structure. A small fraction of grown wires is characterized by having a large number of stacking faults, they present a mixing between wurzite and zincblende microcrystals.
The HRTEM images also highlight an amorphous region surrounding the wires, most probably oxidized GaAs: the Mn wires display a thicker oxide layer (≈ 4 nm) than the Au ones (≈ 1 nm).

4.2 Contacting the nanowire systems

After the growth at the TASC-INFM-CNR laboratory, the samples were further processed at the Max-Planck-Institute for Solid State Research in Stuttgart (Germany) and (in smaller extends) at the Laboratoire de Transport Electronique Quantique et Supraconductivité (LaTEQS) in Grenoble (France), so to be able to perform magnetotransport measurements for their characterization.
The subject of producing low resistance electrical contacts to nanostructures has been for an extended period ineffectively discussed in literature. Many authors present methods and techniques which apparently allow reproducible contacts to be fabricated [50, 51, 52]. The multitude of different nanowire geometries provided by the many different growth modes and techniques appear to be the selection parameter rather than the contact type itself. The challenge in contacting nanowire systems appears therefore to be a statistical problem which has been solved in this thesis by selective statistical methods.
The contacting was done in the following way (see Appendix C for more details):

- The nanowires were transferred from the growth batches onto an other substrate, characterized by the presence of micrometric markers on its surface that will allow the precise location of the wires to be determined for the lithographic step (Fig. C.1). The substrates are highly n-doped and covered by a 200 nm thick layer of SiO_2, so that it is eventually possible to use them also as back gates.
  The wires were afterwards identified using the micrometric markers by means of Atomic Force Microscopy (AFM) or Scanning Electron Microscopy (SEM), depending on the size of the structures under examination. An example of an AFM image is given in Fig. 4.3a, where an InAs wire lies on the smooth substrate between two markers.

- For the contacting process, the substrates with the wires on their surface were first spin-coated by a double layer PMMA resist: the two different layers were employed to obtain an undercut during the development step and therefore have an easier lift-off of the deposited metal at the end. While the thickness of the top layer remained unchanged for all the samples, that of the bottom layer was chosen depending on the thickness of the specific wire to contact and it was then calibrated every single time.

- Based on the AFM or the SEM images, the design for the contacts was defined via the program supplied with the Raith E-Line System (Software version 4.0), used then for the electron beam lithographic step.

- After the development of the exposed resist, etching was crucial to remove the oxide from the surface of the wires before contacting them. It was divided in two stages: O_2 plasma to remove residuals of the exposed and developed resist, and buffered HF for the oxide covering the wires in the contact regions. As it will be discussed in Chapter 5.2.1, attempts were also made using Argon plasma instead of buffered HF. The final effect of this etching is shown in Fig. 4.3b: as one can see, the etched regions appear smoother than the rest of the SiO_2 substrate that was protected by the unexposed resist. The wire itself in the etched regions is slightly thinner compared to its other sections, as it was demonstrated via AFM measurements.

- Immediately after the etching step, the samples were loaded into the evaporator chamber, that was then pumped and brought to a pressure down to 10^{-8} mbar.
  As will be more extensively seen in the following Chapters, different materials were used during this work to define the contacts: for the InAs NWs, Ti/Al and Cr/Au proved to be equivalently valid options, where both Ti and Cr were the thin sticking layers, and Al and Au were the contacting materials; for the GaAs NWs, we preferred to use Cr/Au for normal contacting and Ni for ferromagnetic contacts.

- Finally, the samples went under the lift-off process, where the excess metal was removed via an hot N-Methyl-2-pyrrolidone (NMP) bath, and the finished samples were bonded and prepared for electrical transport measurements. An SEM image of a typical InAs sample after the contacting process is given in Fig. 4.3c.

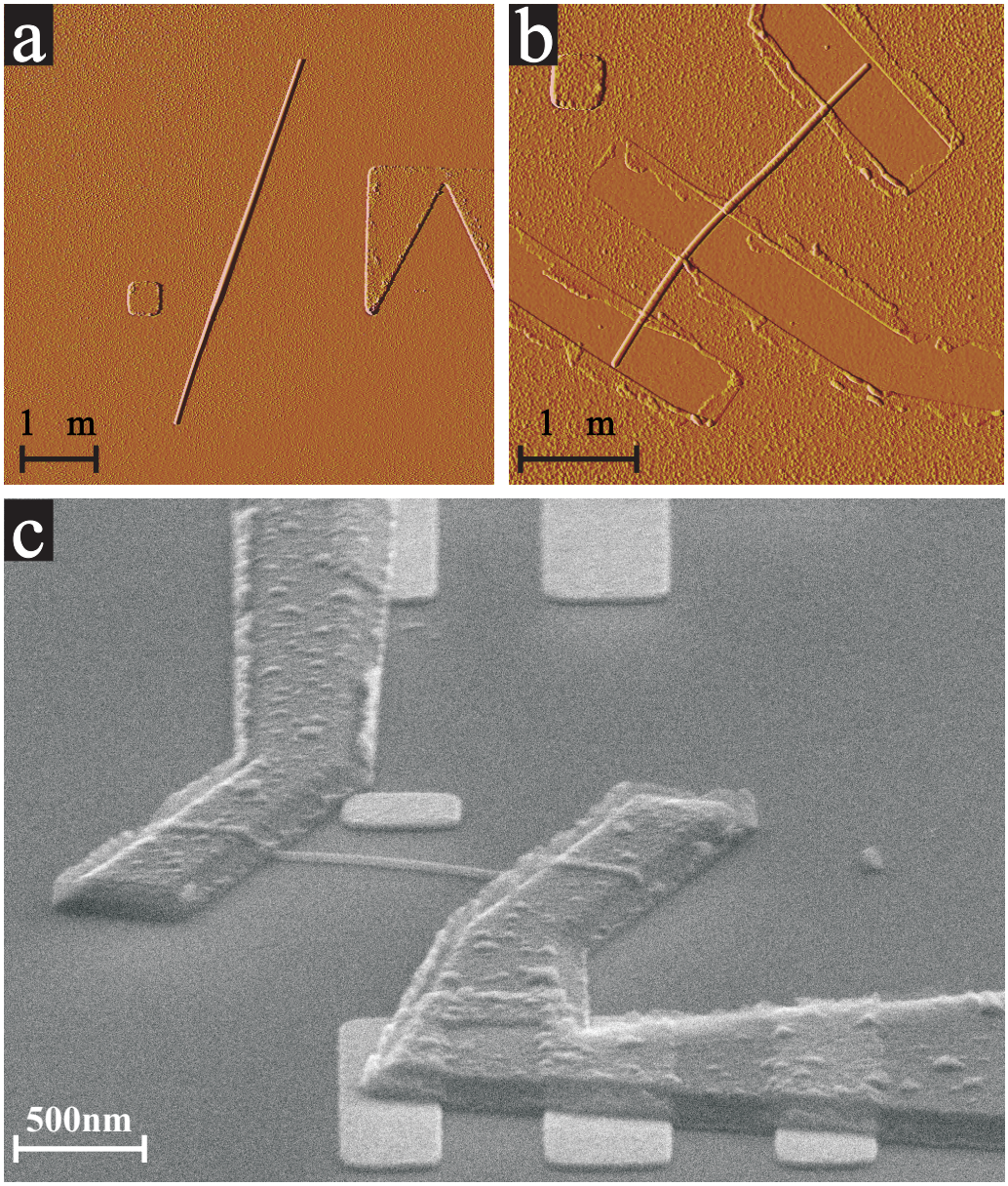

Figure 4.3: Atomic Force Microscope (AFM) images of an InAs wire deposited on the SiO_2 substrate between two markers (a) and of an other InAs wire undergone the etching process to remove the resist residuals and the oxide layer covering the wire in the region that would be contacted (b). (c) Scanning Electron Microscope SEM image of a typical finished sample.

In the following Chapters, the wires prepared using the aforementioned fabrication process will be characterized with and without an external magnetic field.

Chapter 5

Indium Arsenide nanowire systems

In the previous Chapter we saw how high quality nanowires can be fabricated via the VLS growth method using MBE. In this Chapter we will focus on the Indium Arsenide (InAs) material system which, due to its combination of material parameters, presents itself as an optimal candidate for the study of electrical transport.
We will start outlining the advantages of InAs and then proceed to the characterization of wires contacted using various methods. The final sections are dedicated to the study of samples with increased tunability.

5.1 Motivation

In the recent past, InAs nanowires have been extensively studied by many different groups interested in their promising properties [53], [54], [55].
The research fields that triggered all this interest are mainly the further development of semiconductor transistors and of spintronic devices. In the first case, the conventional scaling of devices obtained via the top-down approach (described in Chapter 1.2.1), where the transistors' geometrical size shrinks in all the directions simultaneously, is facing increasing technological difficul-

ties, reaching its fundamental limit. A different point of view on the problem has to be therefore considered, bringing an increasing amount of researchers to look towards the possibilities offered by devices fabricated via a bottom-up approach. The aim here is to reach a control at the atomic scale during the growth process which defines the size of the devices. In the second case, instead, the interest is focused on the active manipulation of the spin degree of freedom in solid-state systems [56]; a deep understanding of spin transport properties in electronic materials, spin dynamics and spin relaxation is crucial here.
Because of its intrinsic properties, InAs is a very promising candidate to fulfill the requirements essentials in these research fields:

- InAs has a Fermi level pinning in the conduction band at the surface, leading to electron accumulation there, making it therefore easier to obtain Ohmic contacts;

- it has a small band gap, good starting point for heterostructure fabrication;

- it has a low effective mass $m^*_{\text{eff}} = 0.023\, m_0$, that leads to strong quantum confinement effects and a high mobility; and

- it has a strong spin-orbit interaction: single spins could be manipulated using an electric instead of a magnetic field.

In order to achieve atomic scale control on the wire growth and to have devices suitable for spintronic applications, the crystal structure of the NW systems has to be low on impurities. Unlike the proposals brought forwards by other groups, based on chemical approaches, in the present thesis we exploit the possibilities of high structural purity that molecular beam epitaxy could bring forward, showing that we were able to scale down the devices size to a very remarkable length.

5.2 Magneto-electrical characterization of a typical NW sample

5.2.1 Statistics of the wire resistance versus the design parameters

InAs nanowires, grown and structured as described in Chapter 4, have been extensively characterized by means of electrical transport.

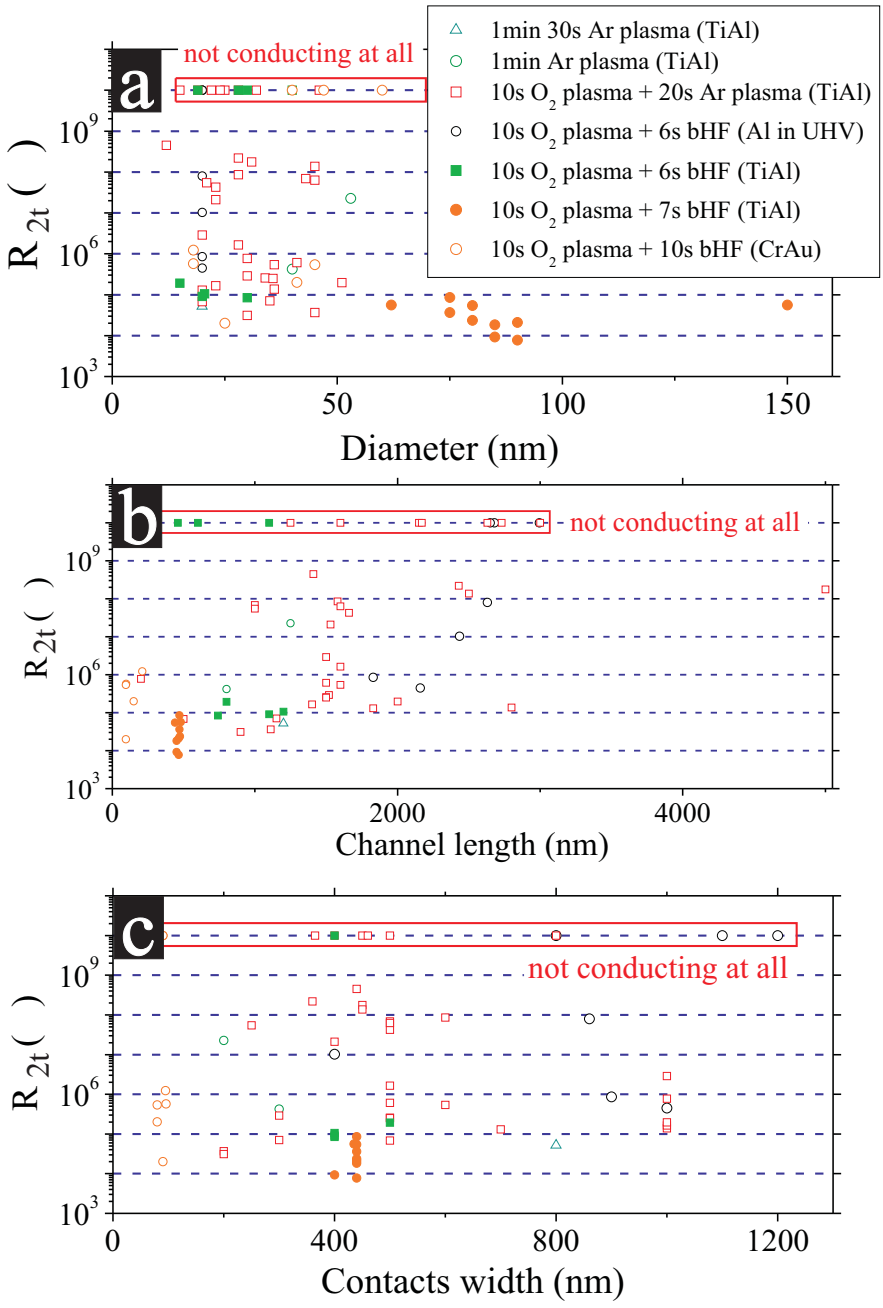

Figure 5.1: Two-terminal resistance values, extracted from the current-voltage characteristics of the measured wires, vs. the wire diameters (a), the channel lengths (b) and the contacts widths (c). The legend, common to all the three plots, indicates the different preparation recipes used to remove the oxide layer covering the wires.

The systems have been measured in a two-terminal configuration: a voltage was applied across the sample and the device resistance R_{2t} could be obtained from the measured current output. Note that in such a measurement not only the intrinsic wire resistance is detected, but also the resistance of the contacts in series.
By measuring current-voltage characteristics on the wires at room temperature, a large spread of discordant results arose. The results are here shown and discussed. In Fig. 5.1 the resistance extrapolated by the current-voltage characteristics is plotted as a function of three different structural parameters. On the same plot, different data are grouped, as described by the legend (common to all the plots): each group corresponds to a different processing procedure to remove the oxide layer encapsulating the wires that has been tried during the optimization phase to obtain a reliable standard recipe. In (a) the resistance is plotted versus the AFM measured diameter of the single contacted wire; in (b), resistance versus the length of the channel formed by the wire between two adjacent contacts; and in (c), resistance versus the width of the contacts superimposed to the wire, i.e. the overlapping surface between wire and metal contacts. From Fig. 5.1a, some highlighting conclusions can be drawn:

- above a diameter of about 60 nm, all the processed NWs were conductive, showing good resistance values between 7 kΩ and 85 kΩ; for this diameter range, evaporation of Ti/Al or Cr/Au as contacting materials proved to be equivalently successful.

- Also for smaller diameters some positive results were achieved, but the spread in the resistance values was much bigger.
  If the contacts width was of the order of $\approx$ 100 nm, we preferred to use Cr/Au for the contacts, so to avoid oxidation of the wire-contact interface from the sides.

- More specifically, the process that involved oxygen plasma and buffered HF etching, followed by evaporation of Ti and Al as contacts, led to a quite uniform set of resistance values of reasonable entities, but the success rate was not encouragingly high;

- a similar etching process, followed by evaporation of Cr and Au contacts, showed a higher success rate and reached lower values for the extrapolated resistance, but the total spread of the results was less compact than the Ti/Al option.

- As mentioned in Chapter 4.2, Argon plasma was also tested in order to remove the oxide layer at the wire-contacts interface via mechanical

sputtering. It could indeed give reasonable results for the resistance values ($\approx$ 30 kΩ), but it proved itself to be highly inconsistent in the performance results and therefore too unreliable for our purposes.

From the analysis of the resistance values versus channel length and versus contacts width, it was not possible to extract a specific trend.
It was quite clear that the transport properties of single NW devices are dictated more by the geometrical size and morphology than by the specific processing. Improvements on the sample processing could lead to an improvement in the values of the contact resistances, without, obviously, affecting the intrinsic wire resistances. Considered the extremely small diameter of these wires, we inferred the origin of such a high intrinsic resistance to the possible presence of impurities along the wire that could lead in their turn to a localization of the charges at low temperatures and therefore to the formation of several zero-dimensional systems in series. In order to avoid such a complicated internal configuration in the NW systems, we investigated the possibility of scaling down the device sizes, as it will be discussed in the last part of this Chapter. The goal would then be to obtain a single zero-dimensional system on which we could control all the transport parameters.

5.2.2 Magnetotransport at base temperature

Electrical characterization

Among the wide variety of NWs contacted and discussed up to here, the samples giving the best room temperature results were also cooled down in the dilution refrigerator to a base temperature of about 40 mK.
The base temperature characterization measurements on the sample shown in the SEM image of Fig. 4.3c are discussed in this Section. In this case, the wire channel length between the contacts was of about 1.1 μm, the width of both the source and drain contacts was of about 200 nm, and the diameter of the wire was of about 30 nm. The wire was lying on a highly n-doped Si substrate covered by a 200 nm thick SiO_2 layer: the substrate could therefore be used as back-gate to tune the electrostatics of the NW. The contacts were formed by a 10 nm sticky layer of Ti followed by 90 nm of Al. Measured first at room temperature, the wire showed a two-terminal resistance value (once again extracted from the linear current-voltage characteristic) of 36.9 kΩ.
Once cooled down to base temperature, the current was measured as a function of the back-gate voltage and we could see that the transport through the NW was strongly characterized by Coulomb Blockade Oscillations (Fig. 5.2a). To extract the value of the charging energy E_C of the NW system, the charge

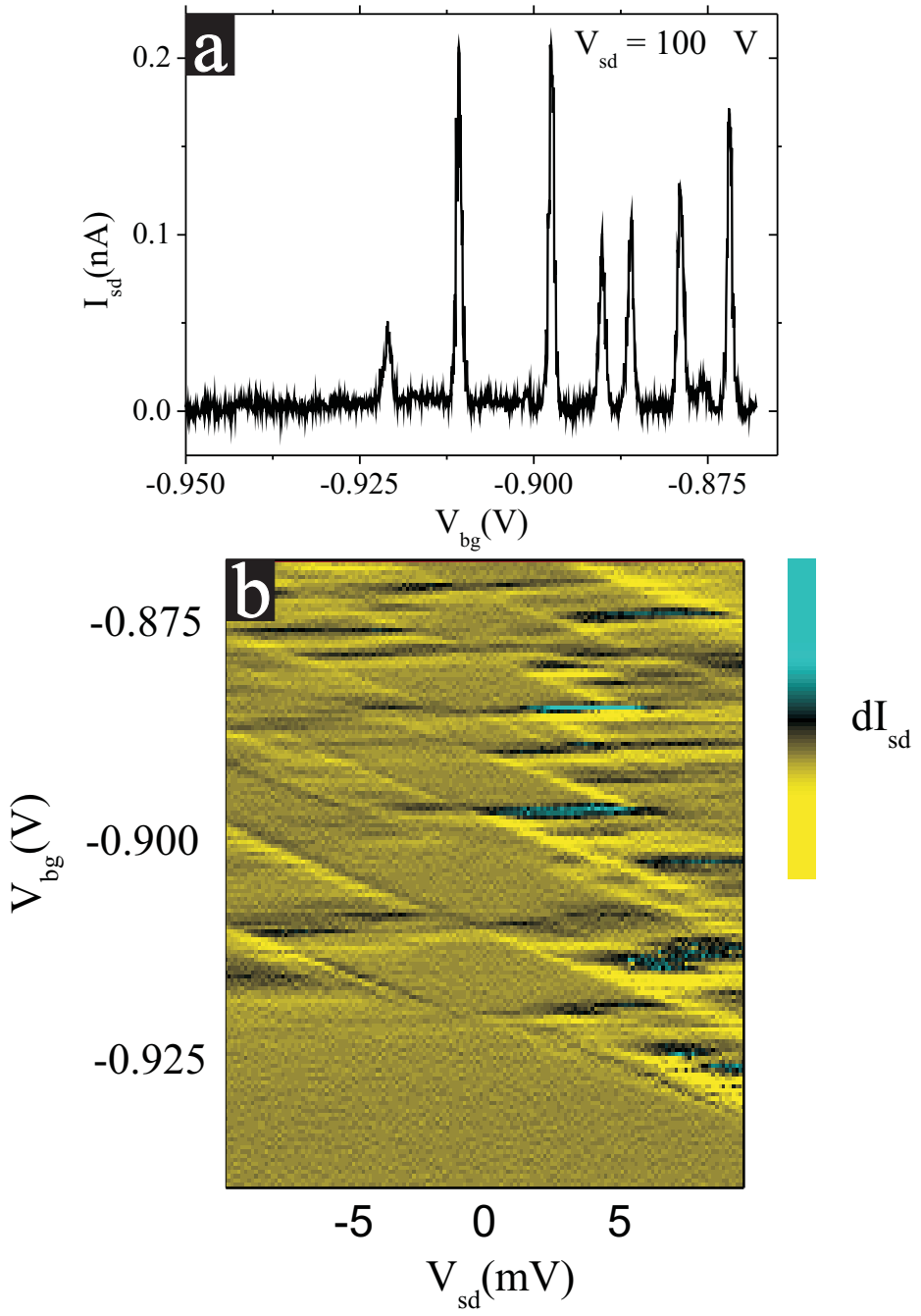

Figure 5.2: Magneto-electrical characterization of the InAs NW system of Fig. 4.3c. In (a): current measured as a function of back-gate voltage shows Coulomb Blockade Oscillation features. In (b): corresponding charge stability diagram, where current is measured vs. source-drain and back-gate voltages.

stability diagram was measured as discussed in Chapter 2.4 and the result is shown in Fig. 5.2b: the numerical differentiation of the current is plotted on the color scale as a function of both the source-drain voltage and the back-gate voltage. As electrical transport is blocked, inside each diamond-shaped region the number N of electrons is fixed, while along the borderlines single-electron transport can occur and therefore current flows through the NW system. The extracted charging energy was of about 7.5 meV; with respect to the QD system discussed in the first part of the present thesis, one can note that now the size of the diamond-shaped Coulomb blockaded regions (and therefore the magnitude of E_C) is much more extended. If the QD of the previous measurements was shaped as a disk with a ≈ 400 nm diameter, now we are investigating a cylinder with a diameter of about 30 nm and 1.1 μm long. The charging energy can therefore be estimated as [11]

$$E_C = \frac{e^2}{2C_\Sigma} = \frac{e^2}{2}\frac{ln\frac{L}{R_0}}{2\pi\epsilon_0\epsilon L}\,, \tag{5.1}$$

where L is the length of the InAs cylinder and R_0 its radius (ϵ(InAs) = 15.15). The obtained value for the charging energy is of about 5.6 meV, quite smaller than that experimentally extracted. It means, the islands have to be smaller. This result can be explained by analyzing the shape of the charge stability diagram: alternating to the large diamond-like Coulomb blockaded regions, one can also observe smaller diamond-shaped ones. This would then suggest that, instead of the one-dimensional cylinder discussed up to here, we have the case of smaller dots in series along the length of the NW channel. Given the small diameter of the NW, in fact, the presence of an even small imperfection could have a strong impact on the overall transport through the wire system, leading to the formation of quantum dots.

Magnetic field dependence

In a different cool down of the same NW system, an external magnetic field was applied perpendicular to the wire channel and substrate.
As observed by Fasth *et al.* in [55] for the case in which only few electrons are trapped into the NW, the presence of a magnetic field leads to the Zeeman splitting of the energy levels within the localized system, offering then two different channels along which transport can occur, depending on the spin orientation of the tunneling electrons. Similarly to the case described in Chapter 2.5, the energy level with spin-up orientation will now be the ground state for the island with ΔN electrons, while the level formed by the spin-down oriented electrons will be its excited state. This effect can be detected

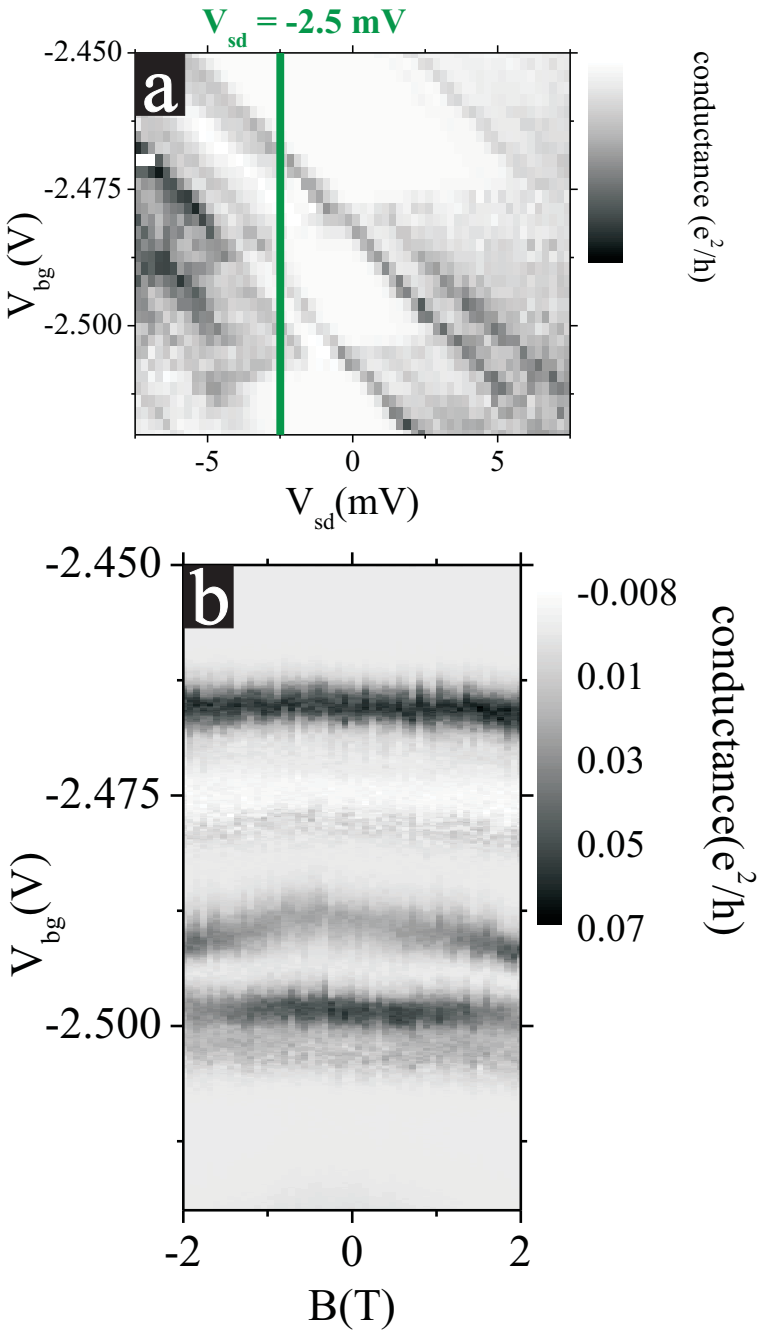

Figure 5.3: (a) Detail of the charge stability diagram of a second cool down of the same sample as in Fig. 5.2. (b) Sweeping of the magnetic field for the CBO trace highlighted in the upper plot.

in the data via a splitting of the conductance peak at the interface between Coulomb-blockaded and Single-Electron-Tunneling regions when measured as a function of increasing B-field. The splitting is caused by the fact that, increasing the B-field, the Zeeman splitting of the energy levels involved in the transport is also increased, shifting then the position of the ground state and the excited state levels in the localized system with respect to the electrochemical potential of the leads.
In order to investigate such magnetic effect in our NW system, a line in the charge stability diagram was selected in the transport pinch-off region (Fig. 5.3a), where the source-drain voltage was kept fixed while sweeping the back-gate voltage. The Coulomb Blockade Oscillation line so obtained was then measured as a function of the magnetic field. The final result is shown in Fig. 5.3b: the Coulomb peaks show to be insensitive to the magnetic field, and only the peak at $V_{\mathrm{bg}} = -2.4875\,\mathrm{V}$ is slightly shifted by the applied field. The weakness of such a magnetic field effect in the transport through our NW system can be explained by the fact that the wire had not been completely depleted at the pinch-off of the transport, but, when the tunnel barriers are completely closed and no current can flow through the wire, some electrons are still trapped into the channel: It is then a many-electrons and not a few-electrons system, the interactions between the electrons would not allow to resolve the spin degeneracy and, therefore, for this reason, our measurements are not comparable to that of the Fasth *et al.* experiment.

Counting down the electrons

Following the tactic exposed in [55], we also tried to count the number of electrons in our NW system down to the very last one. The results of this investigation are shown in Fig. 5.4: in (a) there is the charge stability diagram for the pinch-off region were electrons start to tunnel through the system and at its bottom (in (b)) the zoom in of the parameter range for which the very first electron visibly enters the wire channel. In (c), Coulomb Blockade Oscillation traces are plotted for different values of the source-drain bias voltage and at its bottom, once again, the detail of the pinch-off range (d). One can note here that, even if at zero bias voltage it would appear that there are no more Coulomb peaks below $V_{\mathrm{bg}} = -0.925\,\mathrm{V}$, by increasing the source-drain voltage some additional small peaks appear also below that back-gate voltage value. The peak at $V_{\mathrm{bg}} = -0.95\,\mathrm{V}$ shifts towards more negative back-gate voltage values and therefore belongs to the borderline between the $N = 0$ and the $N = 1$ regions in the charge stability diagram (i.e. the two side wings of the very first diamond that does not close).
From our side, although, such a measurements demonstrates only that we

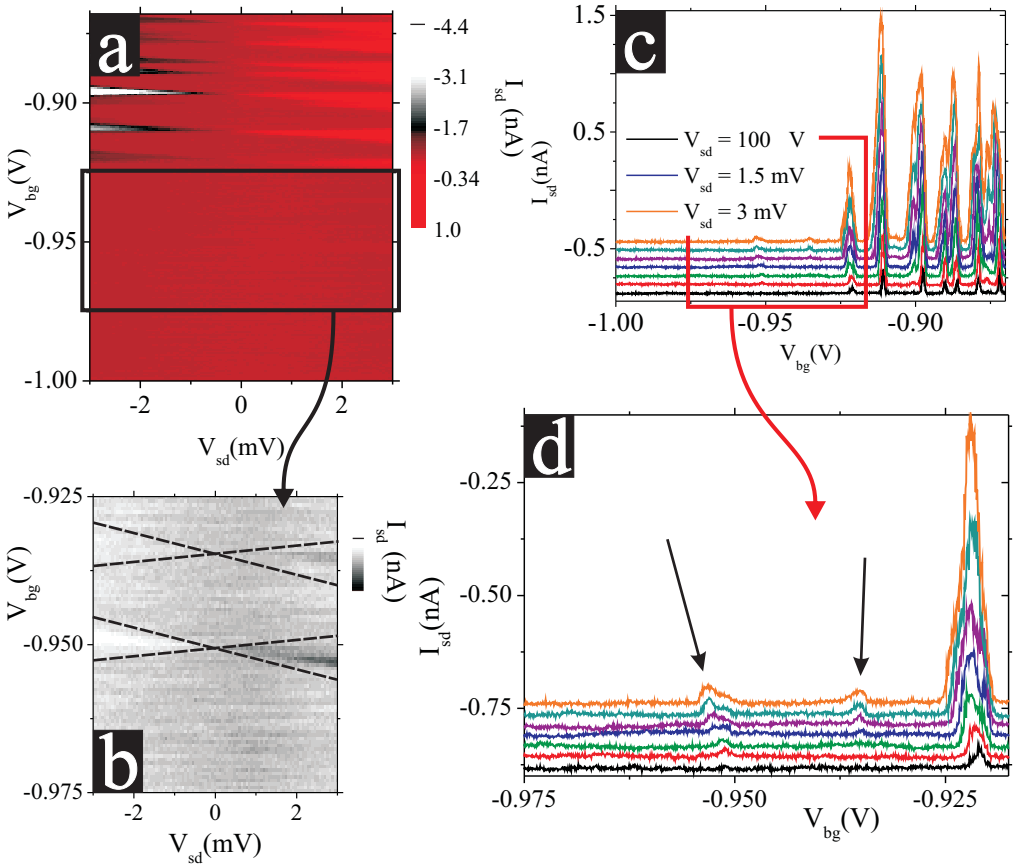

Figure 5.4: Counting the number of electrons inside the NW system channel down to the very last one. In (a): charge stability diagram of the pinch-off region; in (b): detail of the $N = 0 \rightarrow N = 1$ transition region. In (c): Coulomb Blockade Oscillations traces for increasing values of V_{sd}; at its bottom: detail of the parameter region for which the first electron enters the channel.

could identify the very first electron tunneling through the NW system, but not that the channel itself was actually empty before this first transition. This concern is made even stronger considering that the tool used to tune the electrostatic in the channel is a back-gate quite far away, the SiO_2 layer is 200 nm thick, that therefore acts on the channel in a smooth and weak manner, affecting not only the width of the tunnel barriers but also the whole potential landscape in the wire channel. This implies then that, while opening and closing the tunnel barriers, the potential landscape is shifted uniformly and puddles of electrons can be formed in its local minima and trapped there.

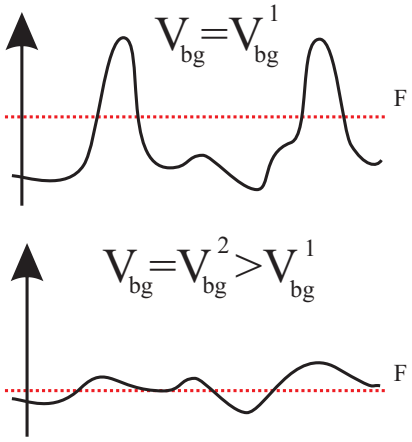

A more satisfying means to make undoubtable the complete emptying of the channel would be the presence of a charge detector nearby, that could probe the number of electrons present inside the pinched-off channel even when transport is blocked.

5.3 Increasing tunability of the NW system

In the previous Section of this Chapter, the main obstacle encountered when characterizing the magnetotransport properties of the NW system was the impossibility to define the exact number of electrons trapped inside the wire channel and taking part in the transport.
To overcome this problem we wanted then to have a better control over the electrostatics of the NW: this meant to add local lateral gates to tune the coupling between the source and drain leads to the channel and to tune the channel separately. In Fig. 5.5 some examples of the different designs tried is shown:

- in (a), the simplest configuration is shown: two gates electrostatically coupled to NW deplete the portions of the channel that they are facing, closing and opening the connections between channel and leads;

- in (b), there are three lateral gates, two of them acting as described in (a), the third one tuning separately the electrostatics of the channel; and

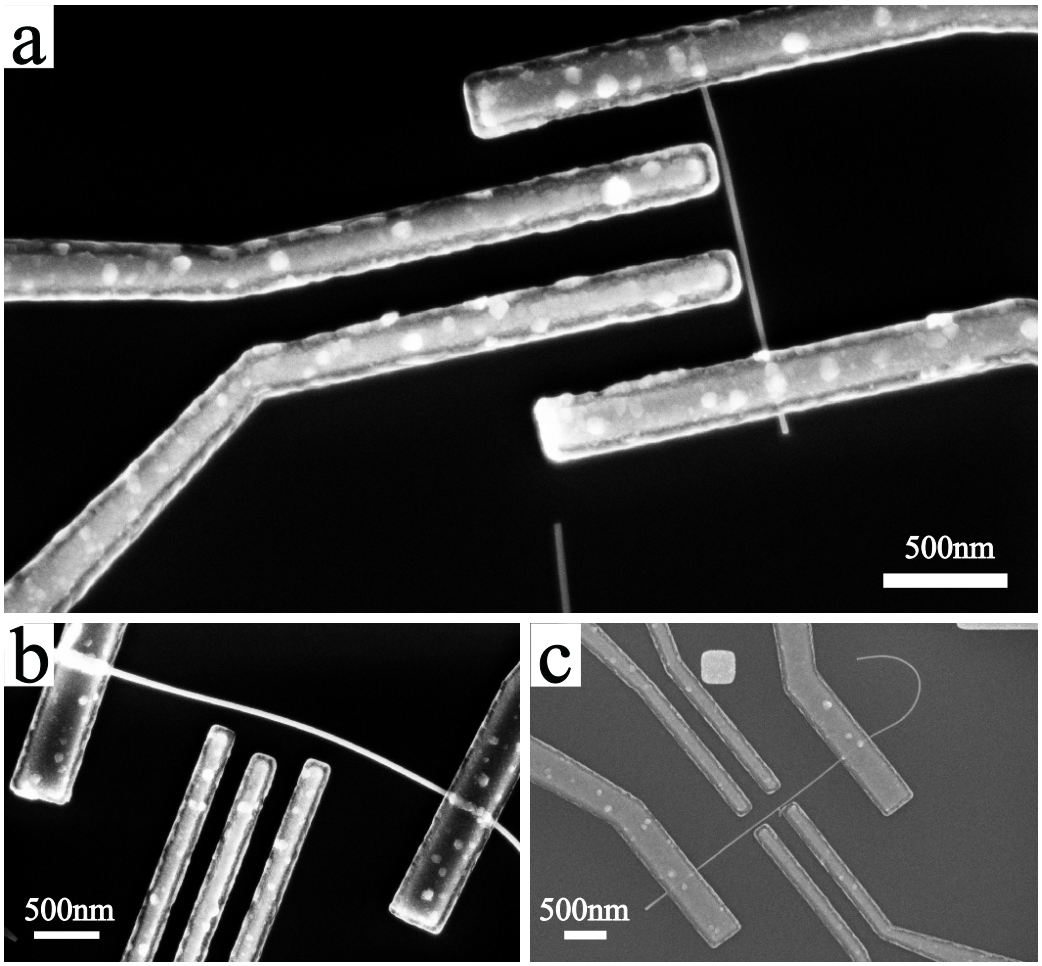

Figure 5.5: SEM images of the different lateral gate configuration designed to increase the tunability of the NW systems. In (a), two lateral gates control the coupling between channel and leads. In (b), a third gate tune separately the electrostatic of the NW channel. In (c), two couples of gates facing each other to deplete more efficiently the portions of channel in between.

- in (c), the last design, where two couples of lateral gates face each other, so to increase the strength eventually needed to deplete the portions of the channel in between and therefore to better tune the coupling between channel and leads.

The NW system of the SEM image in Fig. 5.5a was measured at $T = 4.2$ K and the results are reported in Fig. 5.6: in (a), the current measured in the $V_{g1} - V_{g2}$ plane is plotted in the grey scale, showing the borderlines between

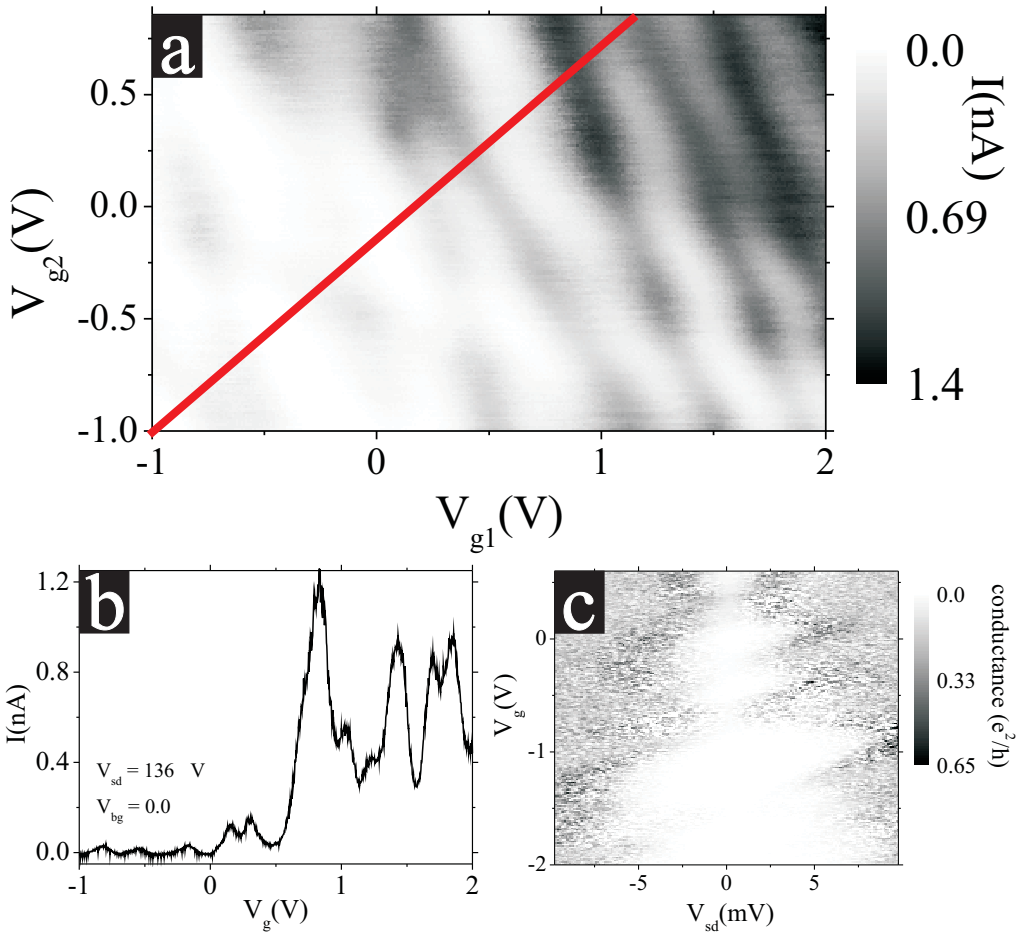

Figure 5.6: Electrical characterization of a NW system with lateral gates that electrostatically tune the coupling between the wire channel and the leads. In (a), the current is plotted on the grey scale as a function of the voltage applied to both the lateral gates; in (b), the CBOs trace along the red line defined in the $V_{g1} - V_{g2}$ plot and the corresponding charge stability diagram (c).

two adjacent charge states of the island as a function of both lateral gates. This type of measurements is very valuable to define how clean is the system under investigation, as already discussed in Chapter 2.3. Comparing these measurements with that of Fig. 2.6, here one can indeed clearly see a strong modulation in the current over the $V_{g1} - V_{g2}$ plane, attributed by us to imperfections of the NW system driven by intrinsic static potential fluctuations due to disorder. The irregularity in the pattern of these modulations superimposed to the normal CBOs suggests a combination of different elements: on one side, the intrinsic potential fluctuations can lead to the splitting of the channel in a series of consecutive dots and therefore transport is characterized by the single-electron tunneling of charges through all these dots in series one by one. One an other side, the presence of impurities in the vicinity of the channel is also possible; for certain values of the voltages applied to the lateral gates, these impurities can be charged and discharged, strongly affecting the whole electrostatics of the wire channel and then the configurations for which electron tunneling can occur.
In Fig. 5.6b the Coulomb Blockade Oscillation trace along the red line in the upper plot is shown; as expected from the strong modulations in the $V_{g1} - V_{g2}$ plot, the Coulomb peaks are here very irregular. An other aspect to be noticed is how broad the peaks are, presumably because of the weakness of the effect that the lateral gates can manage to have on the channel since they act on a very small portion of the wire. By sweeping simultaneously also the backgate, a parameter configuration for which the transport through the NW system was better resolved was unsuccessfully sought.
Nevertheless, a charge stability diagram could be measured even at $T = 4.2$ K: in Fig. 5.6c the conductance is plotted in the grey scale as a function of the source-drain voltage V_{sd} and of both the lateral gate voltages swept along the red trace marked on the $V_{g1} - V_{g2}$ plot. Also in this case, the charging energy E_C is of almost 10 meV, much bigger than the theoretically calculated value of approximately 5.6 meV.
Also the NW gated systems of Fig. 5.5b and c were measured, but unfortunately their room temperature two-terminal resistance was too high to allow a thorough investigation at lower temperatures.

5.4 Scaling down the geometry of the NW systems

To overcome the difficulties arising from the presence of impurities leading to intrinsic potential fluctuations, we proceeded scaling down the whole ge-

ometry of the contacts and of the gates, aiming to a more compact design that could leave less room for the impurities to influence the transport characteristics of the nanowires.
Some examples of the remarkably high lithographical definition achieved in the present work are shown in Fig. 5.7.
Quite peculiar is the structuring of the two systems in Fig. 5.7b and d: there are four consecutive contacts interleaved by three lateral gates. Transport can be measured through the channel between the two central contacts, while the back and the central gates tune the wire electrostatics. In the mean time, the two outer gates will deplete the portions of the wire right at the outside of the source and drain leads so to avoid interference from eventual impurities at the wire-contact interfaces. The outermost contacts will be used to check that these outer portions of the wire have indeed been decoupled.
Given the extremely small width of the contacts, in this case Cr/Au have been evaporated instead of Ti/Al, so to avoid oxidation of the wire-contact interface from the sides.
The NW system of the SEM image in Fig. 5.7a was cooled down to 4.2 K and electrically characterized. The results are shown in Fig. 5.8: on the left,

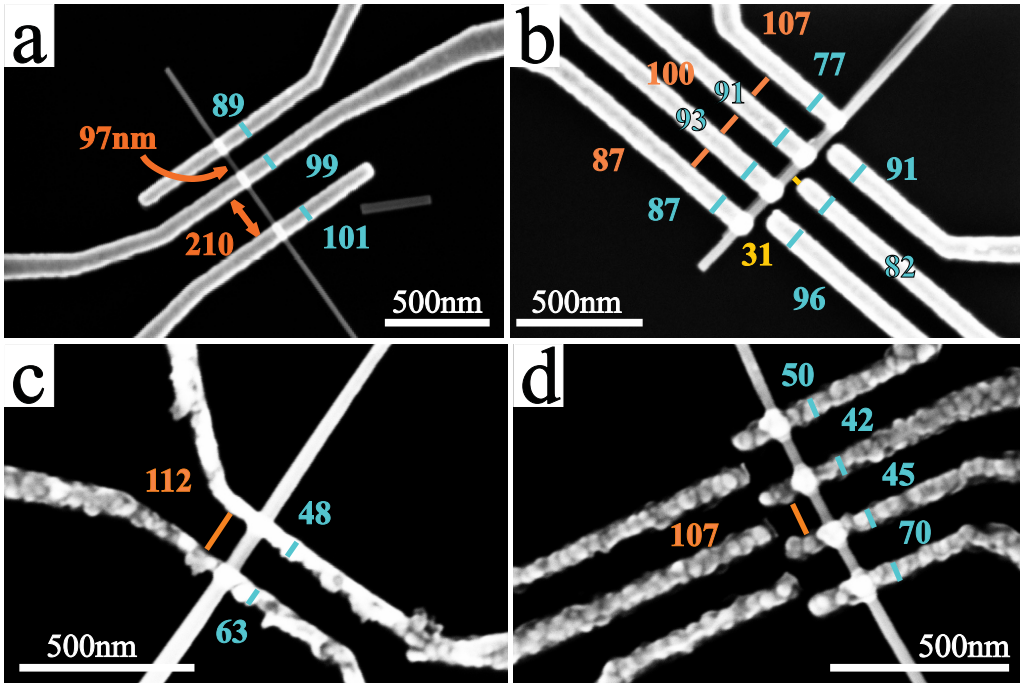

Figure 5.7: SEM images of some of the NW systems defined by a particularly compact design.

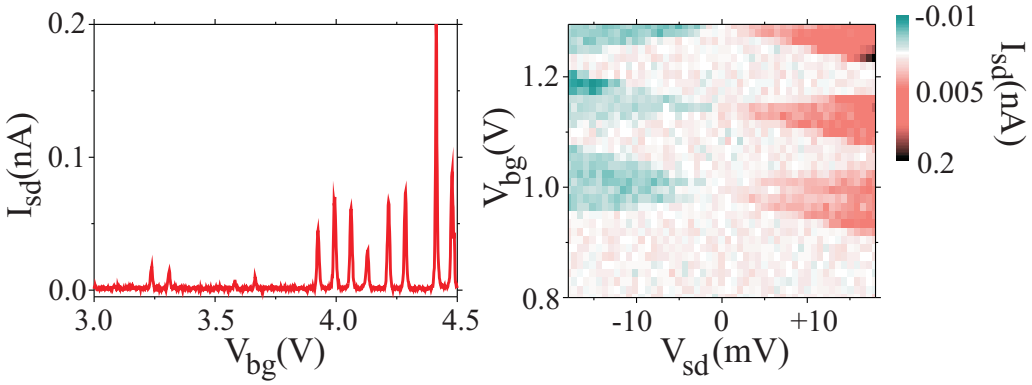

Figure 5.8: Electrical characterization of a particularly small and compact NW system. On the left: CBOs trace; on the right: current vs. back-gate and source-drain voltage.

current measured as a function of the back-gate voltage, and, on the right, the corresponding charge stability diagram. The charging energy is here of almost 20 meV, not too surprisingly, given the AFM measured wire diameter of approximately 19 nm and the length of $\approx$ 100 nm.
To our knowledge, this is the smallest NW system of which measurements have been reported.
Also the other structures in Fig. 5.7 have been measured, but once again, their room temperature two-terminal resistance was too high to allow a thorough investigation at lower temperatures.

5.5 Conclusion and Outlook

In this Chapter we demonstrated how it was possible to combine in sample definition the best properties of the bottom-up approach (extremely reduced geometric size of the wires) together with the wide tunability possibilities offered by the local gating typical of the top-down approach.

- It has been proven that InAs NW systems can in principle be defined adding a large variety of back and lateral gates aiming towards a full tunability of the electrostatics of the wires.

- Systems with wire channels shorter than 100 nm and thinner than 20 nm have also been obtained and characterized, to our knowledge the smallest NW system of which measurements have been reported.

From the magnetoelectrical characterization carried out by us, MBE grown InAs NW systems proved themselves to be suitable candidates for further development of semiconductor transistors and of spintronic devices. Given the small diameter of the NW, though, the presence of an even small imperfection was proved to have a strong impact on the overall transport through the wire system, leading to spread in the reliability of the devices. If, on one side, all the key ingredients for fabricating a high quality and fully tunable device have been demonstrated to be feasible, on the other side, the inconsistent performances of the wires is still an open issue.
In the last step, we want also to upgrade the sample design and include a charge detector nearby, so to be able to probe the number of electrons in the channel without having to inject a current through the system. This will allow us to completely empty the channel of the NW system before the pinch-off of the tunnel barriers.
In literature, the most used type of charge detectors are quantum point contacts (QPCs). A QPC, in fact, forms a one-dimensional channel, through which the conductance is quantized in $\frac{e^2}{h}$ times the number of 'wave modes' (1D sub-bands) of the propagating electrons: the conductance vs. gate voltages measurement is therefore characterized by a series of quantized plateaux that occurs for multiple values of $\frac{e^2}{h}$. When a QPC is tuned to the regime between two quantized conductance plateaux, its conductance depends sensitively on the electrostatic environment, and a single additional electron charge close to the QPC can be enough to induce a measurable change in the QPC transmission [57].
A first feasibility study for the realization of a charge detector has been performed, as can be seen in Fig. 5.9. Unluckily, it was not possible to measure

them due to electrostatic discharge damage during the measuring process. Two possible designs are shown, both of them using a quantum dot capacitively coupled to the primary NW system under investigation: Similarly to the aforementioned QPC usage principle, here the probing dot is biased on the steeper part of the slope of a Coulomb Blockade peak, so that transfer of a charge in the primary system produces a step in the sensor conductance. In (a), a wire close by acts as charge detector via a gate that couples it electrostatically to the NW system under investigation [58], while, in (b), a different portion of the same wire could be used as detector providing that it is only capacitively coupled to the channel involved in the transport.

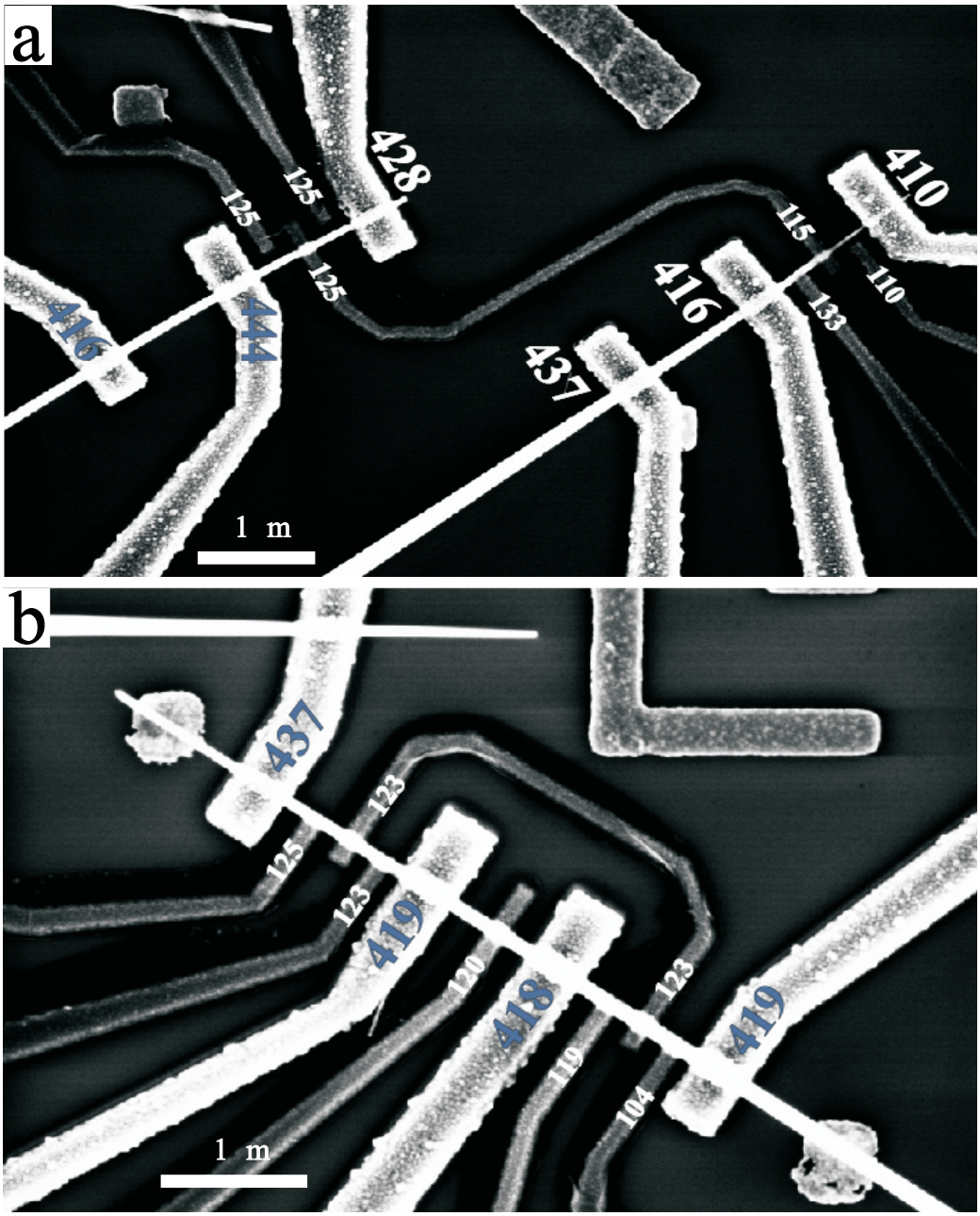

Figure 5.9: Examples for including charge detectors in the NW systems designs.

Chapter 6

Beryllium doped Gallium Arsenide nanowire systems

In Chapter 4, the MBE growth of nanowires was discussed. The inclusion of a dopant source further increases the level of usability resulting in a whole new family of devices and associated novel device physics. Some of the most promising among these novel devices, as it will be discussed, are the so-called diluted magnetic semiconductors (DMS), where magnetic and semiconductor properties can be tailored in a single device.
In this Chapter, we will discuss the feasibility of applying the well known DMS technology to devices obtained from single Gallium Arsenide (GaAs) nanowires grown via the MBE technique.

6.1 Motivation

The information technology of today utilizes both the charge and spin properties of electrons in the solid state, applying them to semiconductor devices for integrated circuits and magnetic materials for mass storage of information.
The aim of the research discussed in the following Chapter is to exploit the possibility of combining these two properties in one material, focusing on semiconductors with ferromagnetic properties.

There are two main issues to take into account when considering magnetic materials and semiconductors:

- the crystal structure of magnetic materials is usually very different from that of semiconductors used for electronic devices, affecting therefore the efficiency of spin-injection through their interface, and

- semiconductors commonly used for device fabrication, like Si and GaAs, are nonmagnetic and their magnetic g-factors are too small for everyday use.

In order to overcome these problems, we focused on the development of ferromagnetic semiconductors for spin-electronic devices by introducing magnetic elements into nonmagnetic semiconductors. These types of materials are know in literature as diluted magnetic semiconductors (DMS) and they are characterized by the fact that their magnetic properties are driven by the spin-exchange interactions between the magnetic ions and the free holes.
Investigations in this research field, initiated in the late 1970s and widely developed during the 1990s, have concentrated on three major fronts: the microscopic origin and fundamental physics of ferromagnetism occurring in these systems, the material science of growth and defects, and the development of spintronic devices. An introductory insight in this topic can be found in [59, 60, 61, 62, 63], or on the database of published work and preprints at http://unix12.fzu.cz/ms.
To understand the microscopic origin of ferromagnetism in such DMS materials, let us consider, for example, the nominal atomic structure of the elements in a bulk GaAs compound doped with Mn [63]:

Mn:	[Ar] $4s^2$ $3d^5$
Ga:	[Ar] $4s^2$ $3d^{10}$ $4p^1$
As:	[Ar] $4s^2$ $3d^{10}$ $4p^3$

Manganese has 7 valence electrons, 2 placed in the s-orbital and the remaining 5 in the d-orbital that is therefore incomplete. Gallium has 13 valence electrons, 2 in the s-orbital, 10 in the d-orbital and the last one in the p-orbital. Arsenide has 15 valence electrons, 12 filling the s- and d-orbitals as for Ga, while 3 electrons are placed in the p-orbital.
Given the minor difference between their relative atomic numbers, preferably Mn tends to replace atoms of Ga and, because of the missing valence electrons, the Mn_{Ga} impurity acts as an acceptor with local spin $S = 5/2$. It is believed that interactions suppress charge fluctuations in the Mn impurities and d electrons can be treated as nonitinerant in DMS [64], and therefore they are exchange coupled to itinerant carriers originating from the p-levels of

the Fermi sea of the hosting GaAs crystal (the exchange energy is minimized, in this case, for $J_{\text{exch}} > 0$, i.e. for the electron spins in an antiferromagnetic configuration).

Inspired by the success reached in fabricating bulk DMS, a significant effort has been also focused on two-dimensional (Ga,Mn)As systems [65, 66], leading to the successful observation of high values for the Curie temperature, domain structure properties, anomalous Hall effect, and magnetooptical properties, etc.
Following this trend in dimensionality reduction, we will investigate in this Chapter the possible realization of a one-dimensional DMS. It is based on GaAs nanowires grown from a Mn metallization of the substrate; since on their own the Mn ions would interact too weakly, we further increase the presence of carriers by doping the NWs with Be.

6.2 Sample preparation and measurement setup

The sample preparation and the measurements discussed in the following are the result of the collaboration with the group of Silvano De Franceschi at the CEA (INAC/SPSMS/LaTEQS facility) in Grenoble, France.

The Be doped Mn-GaAs NWs have a diameter ranging from 50 nm up to 150 nm, that implies a contact design less constrained to small sizes than that seen in Chapter 5. A typical contacted wire is shown in Fig. 6.1: the two inner contacts are $\approx$ 470 nm wide, while the outer ones extend to the whole length of the NW. The distance between adjacent contacts is on the order of 330 nm.
Before the deposition of the metal contacts, the oxide layer covering the NWs have been removed by dipping for 10 seconds in a solution of 49% HF and deionized water, with a proportion 1:100. Different combination of metals have been alternatively evaporated: CrAu, for normal metal contacts, and Ni, for ferromagnetic contacts. Additional details about the sample preparation can be found in Appendix C.
Two experimental configurations have been used: In the two-terminal configuration a voltage is applied across the sample and the system resistance $R_{2\text{t}}$ can be obtained from the measured current output. We realized that in some devices contact resistances were large compared to the NW channel resistance, becoming then the predominant component in the measured current-voltage characteristic. In order to avoid such a dominant role of the contacts, we preferred a four-terminal configuration, where a current is in-

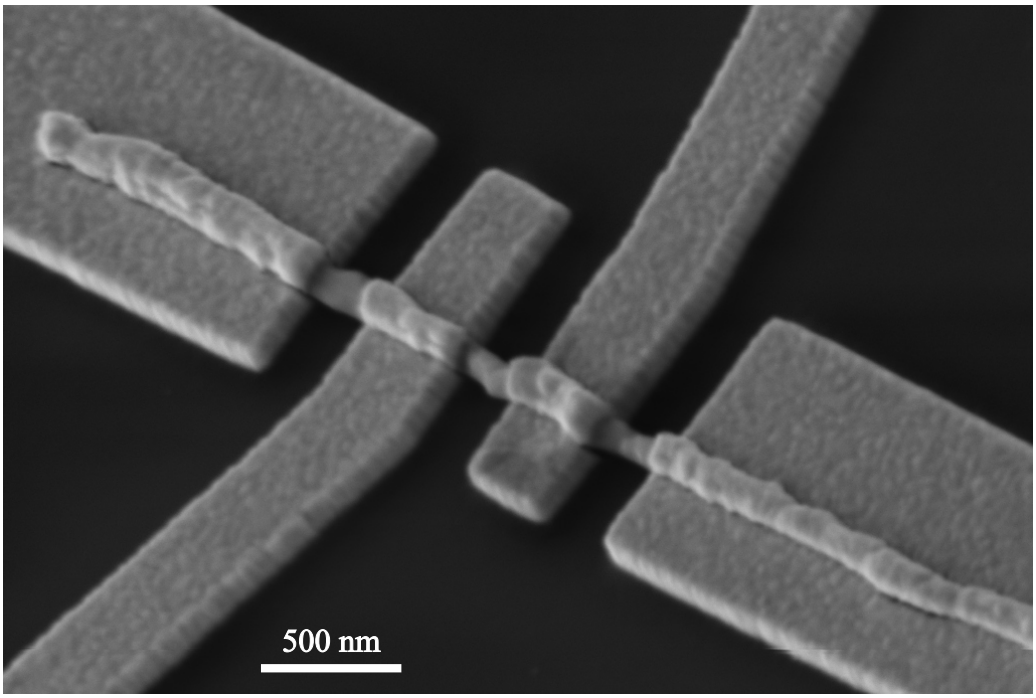

Figure 6.1: Scanning Electron Microscope image of a typical Be-doped Mn-GaAs NW system in a four-terminal configuration: the contacts are $\approx 470\,\text{nm}$ wide and 110 nm thick, the length of the channel formed by the wire between adjacent contacts is of about 330 nm. Even if the surface of the wire is characterized by a strong roughness, given the large diameter, the transport through the system is usually not localized as a QD would be formed.

jected from one of the outer contacts while keeping the other at ground and the voltage drop is measured between the two inner contacts. This last configuration enables direct access to the magneto-resistance properties of the NW without suffering from contact effects.
With the goal to uncover possible signatures of ferromagnetic correlations, the NW systems have been measured at temperatures ranging from 300 K down to 1.5 K. In order to access such a wide temperature range, a heating element was added into the sample holder located close to the wires, so that, once inserted into a helium bath, the temperature could be tuned in a controlled manner (more details about the measurements setup in Appendix A).

6.3 Magnetotransport measurements

In this Section, measurements on two different sets of samples are presented: a first investigation carried out by the group at the Laboratorio Nazionale TASC-INFM-CNR in Trieste on Mn-GaAs with a low Be doping level, and the more extended analysis on NWs with a higher doping level.

6.3.1 Low Beryllium doping level

The experiment of Martelli *et al.* in [47] demonstrated that nominally undoped Au-GaAs NWs, grown in the very same conditions as the wires presented here, resulted in n-type electrical behavior. On the contrary, undoped Mn-GaAs NWs showed a well pronounced p-type characteristic. Since Mn in GaAs acts as an acceptor, these data support the thesis that Mn diffuses into the wire during the growth.
In order to strengthen the interaction between the Mn ions diluted along the wire, a further hole-type Be doping was later introduced [67], with a corresponding impurity concentration of $9 \times 10^{18}\mathrm{cm}^{-3}$. The electrical characterization at room temperature of this last type of NW systems showed that the wire system was highly resistive ($R_{2\mathrm{t}} \sim 0.57\,\mathrm{M}\Omega$) and it was characterized by a strong non-linearity around the zero source-drain voltage (data not shown). The current through the wire has been measured as a function of the back-gate voltage for different constant value of the source-drain voltage. From this last set of data, it was possible to observe an increase in the current through the system whenever negative back-gate voltages were applied. This measurements then highlighted the p-type nature of transport through Be doped Mn-GaAs NWs. At room temperature the effect of the back-gate was not particularly strong, though, indicating that the hole concentration is

already starting to be high enough to lead towards a quasi-metallic behavior of the wire.
A more effective tuning of the holes concentration in the channel via the voltage applied to the back-gate is obtained at lower temperatures: Fig. 6.2 reproduces the same type of measurements as those aforementioned, but at $T = 77$ K.
On top the current-voltage characteristics for several values of the back-gate voltage and, on the bottom, source-drain current vs. back-gate voltage for different V_{sd} voltages. The two-terminal resistance at zero V_{bg} is not much affected by the lower temperature. On the contrary, the effect of V_{bg} is here much more noticeable: by applying voltages $V_{\mathrm{bg}} \approx 40\,\mathrm{V}$, the wire channel is emptied of hole carriers and no transport occurs through the NW system.

Finally, the same sample has been also cooled down to $T = 4.2$ K (data not shown); in this last case, the transport through the NW system was completely localized and characterized by Coulomb Blockade Oscillations. This was somehow expected, given the already high two-terminal resistance at room temperature and the fact that in a semiconductor usually the resistance increases for decreasing temperatures. This localization effect proved itself to be the dominant component in the transport through the wire, making it impossible to distinguish possible ferromagnetic signatures.
In order to overcome this obstacle, Mn-GaAs NWs with a higher carriers concentration were grown, as it will be discussed in the next Section.

6.3.2 High Beryllium doping level

Au-GaAs nanowire systems

Before investigating the effect of diluted magnetic impurities on semiconducting nanowires, let us analyze magnetotransport through Be doped GaAs NWs grown from a non-magnetic layer of gold deposited on the growth substrate.
In Fig. 6.3 the results from a typical Au-GaAs NW system with high Be doping level (corresponding impurity concentration of 2.5×10^{19} cm^{-3}) is reported: the diameter of the (tapered) wire is ranging between 60 and 100 nm, while the channel between the central contacts is 330 nm long. The NW system is contacted with a 110 nm thick Cr/Au metallization. The four-terminal resistance $R_{4\mathrm{t}}$, extracted from a series of current-voltage characteristics, is plotted as a function of the temperature: from this measurement, transport appears to be dictated by two different regimes, depending on the temperature ranges:

- Starting from $T = 300$ K and cooling down: charges moving through

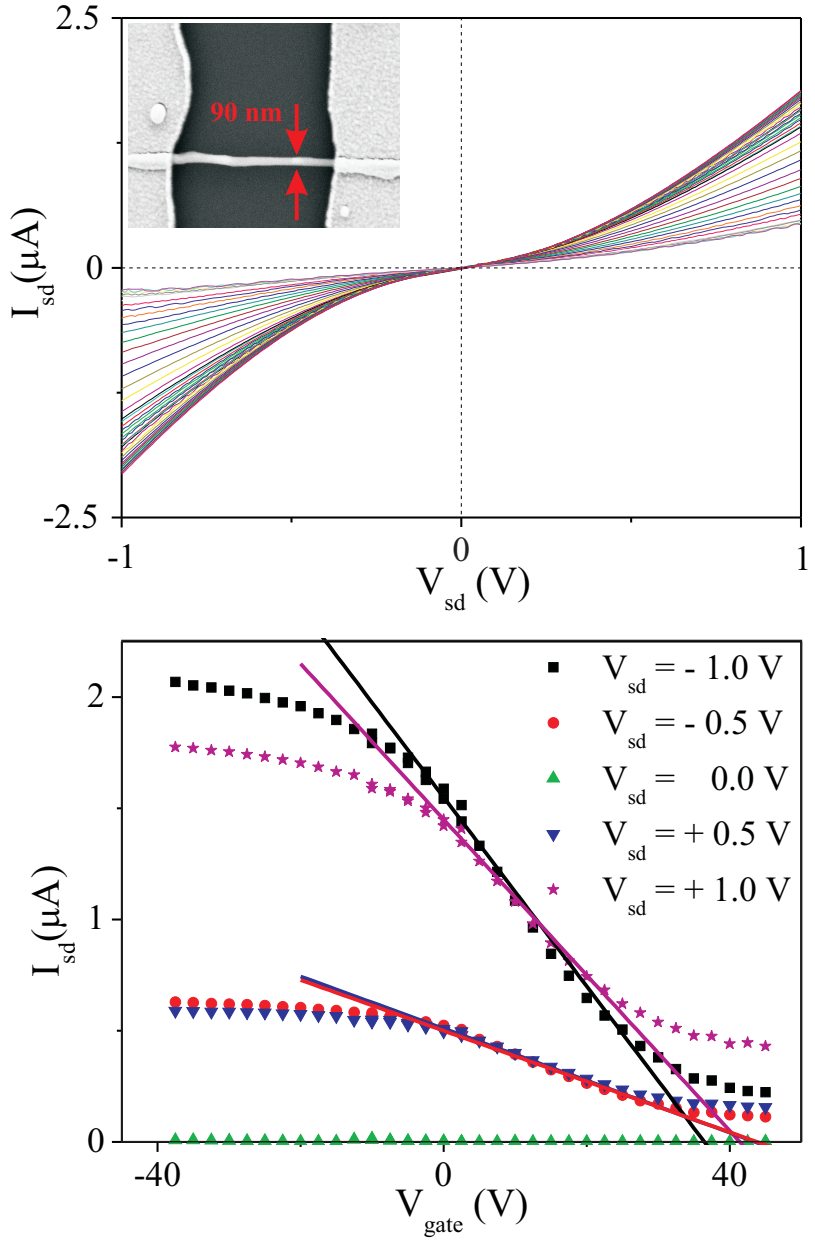

Figure 6.2: Typical Mn-GaAs NW doped with a low concentration of Be measured at $T = 77$ K. Top: current-voltage characteristics for different values of the applied back-gate voltage. In the inset, SEM image of the wire system. Bottom: source-drain current vs. back-gate voltage for different values of the applied constant source-drain voltages. Courtesy of F. Capotondi [67]

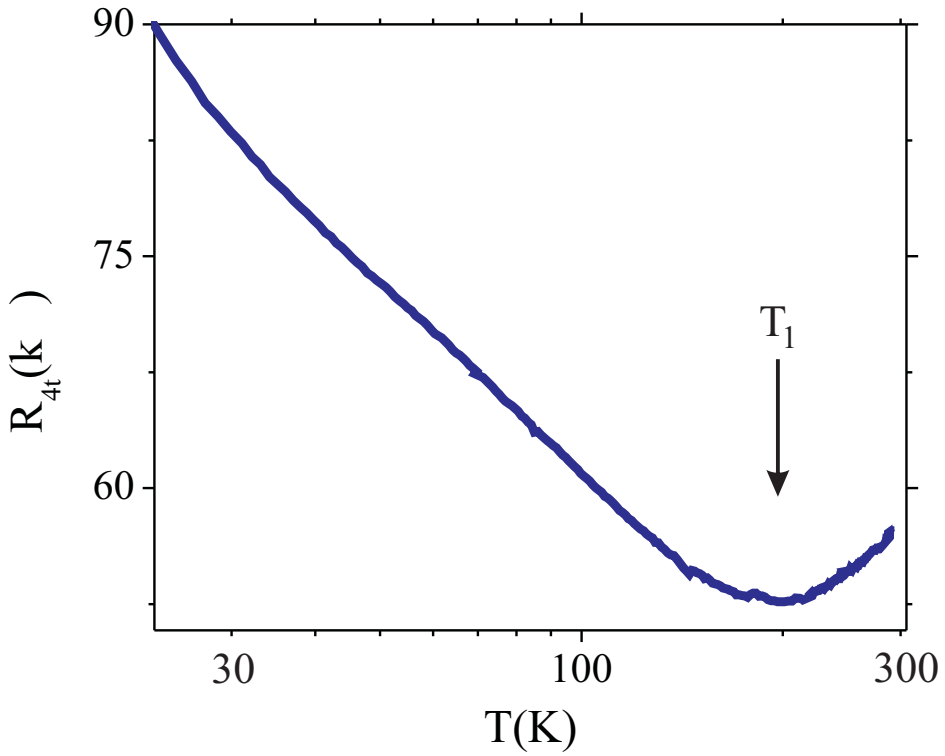

Figure 6.3: Four-terminal resistance vs. temperature for a typical Be doped Au-GaAs NW system with Cr/Au contacts.

the system suffer mostly phonon scattering. While decreasing T, the lattice vibrations become weaker, leading therefore to a decrease of the resistance measured through the wire [68]. For a temperature $T_1 < T_{\text{room}}$ (where the value of T_1 varies slightly from sample to sample), the resistance of the NW reaches a minimum.

- Below $T = T_1$: the resistance $R_{4\text{t}}$ increases again. In this temperature region, in fact, the intrinsic carrier concentration of a semiconductor decreases [69].

In most of the measured NW systems the resistance values $R_{4\text{t}}$ were low enough and did not lead to a localized type of transport like the one previously observed for the cases of lower Be doping. However, as shown in Appendix D, a small minority of the measured wires showed at low temperature Coulomb Blockade Oscillations.
The effect of an external magnetic field applied perpendicular to the wire was also measured; the results are shown in Fig. 6.4: On top, the temperature

dependence of the wire resistance R_{4t} has been measured for both the $B = 0$ T and the $B = 5$ T cases, on a lower T range with respect to the one of Fig. 6.3. It is clearly seen that

- for $T > T_2$, the two curves ($B = 0$ T and $B = 5$ T) are perfectly superimposed to each other: there is no magnetic effect in the transport through the NW system, while

- for $T < T_2$, the behavior of the wire when a magnetic field is applied differs significantly from that in absence of the field.

The difference in the magnetotransport is plotted in a more direct way on the lower part of Fig. 6.4, where R_{4t} is shown as a function of the B-field for several temperatures: A strong magneto-resistance arises in the data, which becomes more pronounced the lower the temperature. For higher temperatures, a small asymmetry with respect to the $B = 0$ T point can be noticed, due to a slight variation of the temperature in those ranges.
Low-temperature magneto-resistance in low-dimensional electron systems, in literature, is usually linked to a weak localization effect (for an introduction to this topic see, for example, [9]). Weak localization is the result of an enhancement of back-scattering from a set of scattering centers in a disordered environment, that leads to a value of the electrical conductivity of the system lower to that expected from the classical Drude formula. While the Drude formulation is based on a single-impurity scattering process, the weak localization is generated by the constructive interference between electron waves that scatter from the same set of impurities either clockwise or anti-clockwise:

The electron waves start from the same impurity site, scatter from it to follow a random-walk path (in the form of a closed loop) along the same set of surrounding impurities, but in the opposite direction, and finally scatter into exactly the same backwards direction.

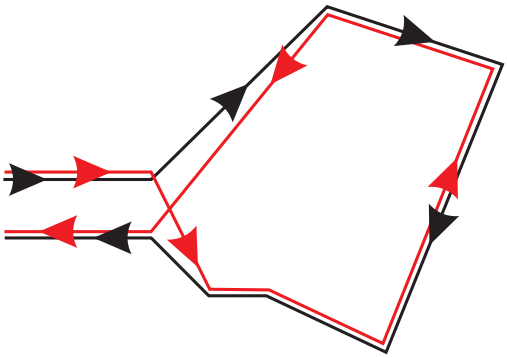

The observation of such an interference effect requires phase-coherent propagation along the closed-loop part of the geometrical trajectory. Furthermore, the magnitude of the observed contribution from this backscattering depends

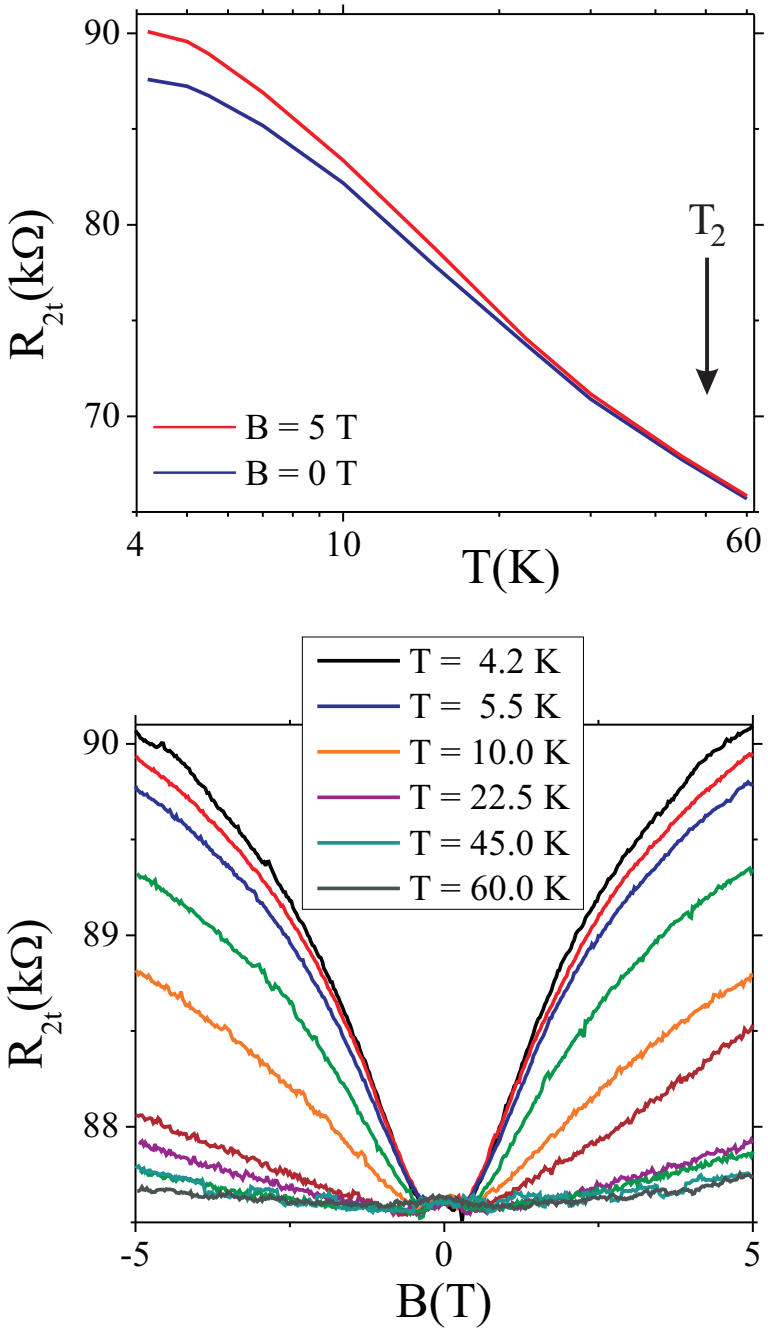

Figure 6.4: Four-terminal resistance for a typical Be doped Au-GaAs NW system with Cr/Au contacts, plotted as a function of temperature (top) and of magnetic field (bottom, the curves are offset for clarity).

on the amplitudes related to the electron propagating along the same geometrical loop either clockwise or anti-clockwise. Whenever an external magnetic field is applied, a difference between these amplitudes arises due to the Aharonov-Bohm phase accumulated along the path. The result of the B-field is therefore a reduction of the resistance of the conductor at low temperatures (i.e. a **negative** magneto-resistance).
In our measurements, though, the distinctive feature was a strong **positive** magneto-resistance, i.e. a weak anti-localization effect.
Another possibility for the magnetic field to affect the interference arises due to the coupling between orbital motion and electron spin [70]. The spin-orbit coupling is particularly strong in p-type GaAs materials because of

- their crystal structure, that are characterized by p-like valence band wave functions, and

- the fact that spin-orbit interaction scales with the atomic number of the atom, so that heavy elements like Ga and As lead to a significant coupling effect [71], [72].

Spin-orbit modifies the above-described interference effects: As the spin experiences a sequence of scattering events along its path, the spin orientation is randomized on a characteristic length scale l_{SO}. The stronger the spin-orbit interaction, the smaller is l_{SO}; so that, as the strength of the spin-orbit interaction increases, a transition from weak localization to weak anti-localization can be observed [73]. In particular, strong spin-orbit coupling changes the constructive interference between the different paths encircling the same closed geometrical loop in opposite directions into destructive interference [74]. Furthermore, weak antilocalization effects in quantum nanowire systems have been widely studied both experimentally and theoretically [75, 76, 77], showing that the amplitude of this effect depends non-linearly on the ratio between the wire width and the phase coherence length.
Even if the quantitative analysis carried out for these aforementioned experiments is not directly comparable with out case, due to the different material (InAs instead of GaAs) and of the different range of the widths there considered, the qualitative discussion about the origin of the observed weak anti-localization still holds. For this reason then, the applied magnetic field can lead to the strong positive magnetoresistance observed in our measurements.

Mn-GaAs nanowire systems

In order to uncover possible signatures of ferromagnetic correlations, the same measurements procedure as in the previous Section were performed on

similarly grown Mn-GaAs wires.
The results are plotted on Fig. 6.5:

- On top, the resistance R_{4t} is plotted as a function of temperature. The trend of the curve shows the same features as for the case of Au-GaAs NW systems, a higher T range where transport is dominated by phonon scattering, a middle range where it is dominated by impurity scattering and a lower T range were weak anti-localization dictates the transport characteristics.

- On the bottom, the resistance R_{4t} as a function of the magnetic field. Once again, the strong positive magneto-resistance effect originated by the spin-orbit interactions is clearly visible.

Analysis on Mn-GaAs NW systems with ferromagnetic contacts (110 nm thick Nickel) have also been carried out, as reported in Fig. 6.6.
On top, the two-terminal resistance R_{2t}, extracted from current-voltage characteristics at $T = 4.2$ K, is plotted as a function of the magnetic field. Depending on the direction along which the field is swept, one can notice a jump in the resistance values when the $B = 0$ T axis is crossed (denoted as magnetic switch). The four-terminal resistance (bottom of Fig. 6.6), though, measured under the same conditions does not show such a behavior, but the curve has a smooth minimum around the zero field region. From this, we can state that the switching feature observed in the R_{2t} is a characteristic arising from the contacts properties and not from the Mn-GaAs NW itself. This feature can be explained by the fact that, because of the different geometrical configuration between the two ferromagnetic contacts, one of them changes its spin polarization before the other, giving reason to the observed change in the resistance through the system depending on the direction of the sweeping magnetic field.

6.4 Conclusion

In the present Chapter, magnetotransport through Beryllium doped Gallium Arsenide NW systems have been discussed. Different cases have been considered, depending on the level of Be doping, on the metal used to grow the NWs (either Au or Mn) and on the type of contacts (normal metals, with Cr/Au, or ferromagnetic metals, with Ni).
Comparing all these data we can extract valuable information about the GaAs NW systems:

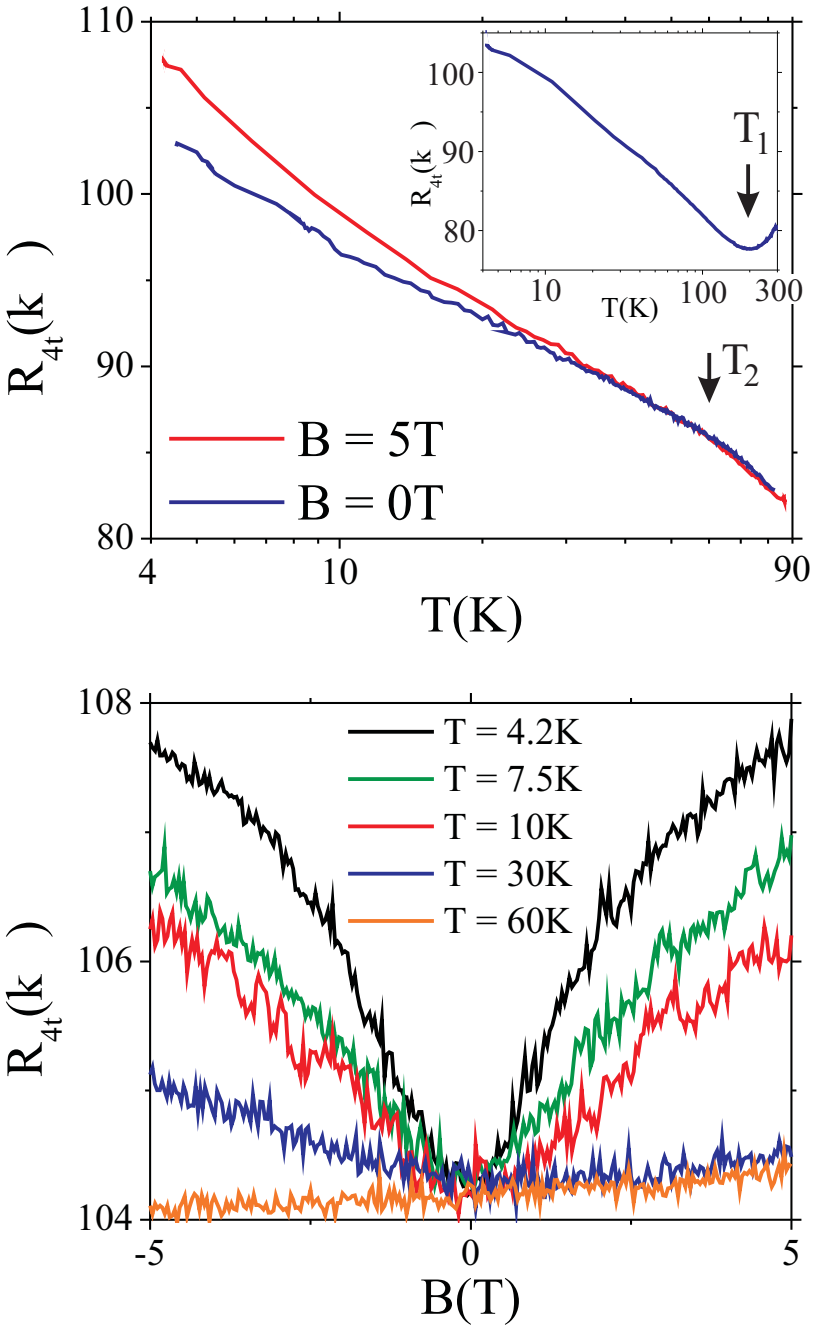

Figure 6.5: Four-terminal resistance for a typical Be doped Mn-GaAs NW system with Cr/Au contacts, plotted as a function of temperature (top) and of magnetic field (bottom, the curves are offset for clarity).

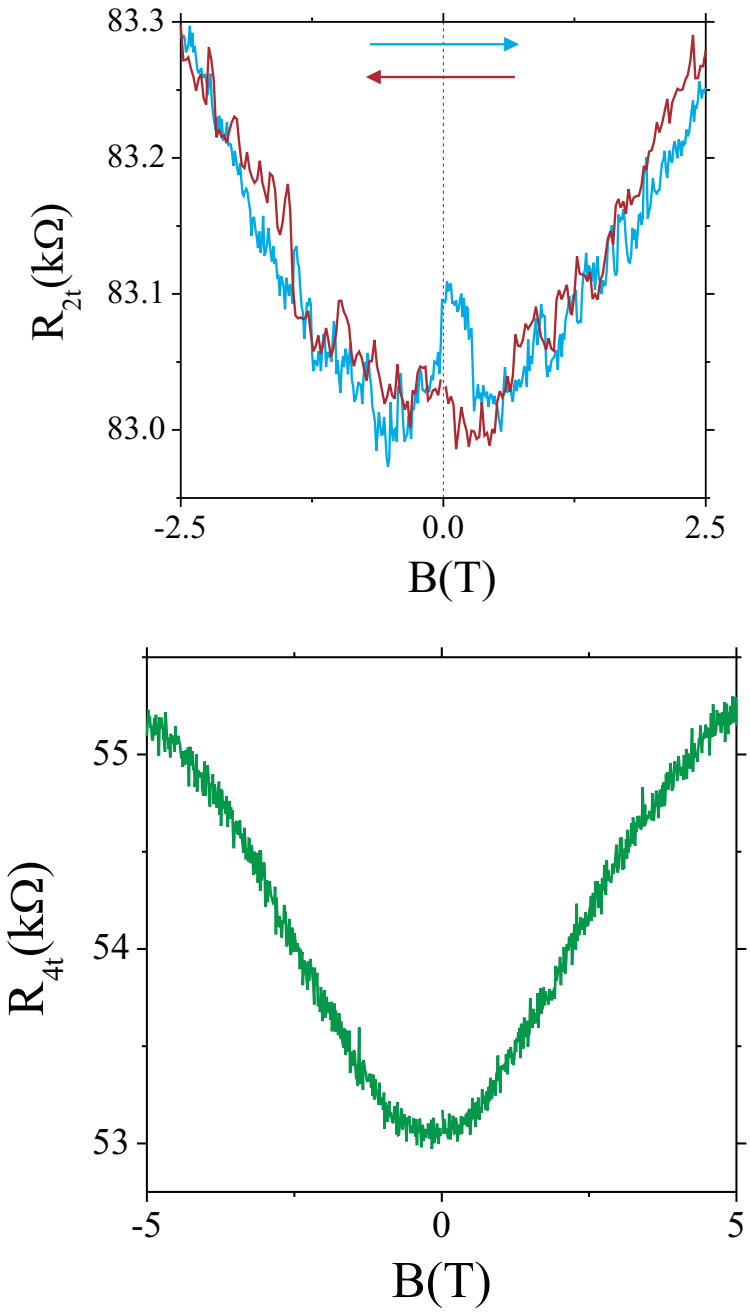

Figure 6.6: Two-terminal (top) and four-terminal (bottom) resistances for a typical Be doped Mn-GaAs NW system with ferromagnetic contacts, plotted as a function of magnetic field. The arrows indicate the sweeping direction of the magnetic field.

- Depending on the temperature range, the transport can be dominated by phonon scattering, impurity scattering or weak anti-localization;
- in the T range dominated by weak anti-localization, a strong magnetoresistance is observed, stronger the lower the temperature, explained via the spin-orbit coupling between the electrons spin and the orbital motion; and
- no apparent effect of the presence of magnetic ions situated along the length of the wires could be observed.

The Mn-GaAs NW systems were also contacted using ferromagnetic metals, but, even if the contacts themselves show indications of their spin-polarization, no spin information could be carried through the wire.
From the experiments performed at the Laboratorio Nazionale TASC-INFM-CNR in Trieste and reported in [47], we know that Mn ions are indeed present dislocated along the GaAs NW, but, most likely, their concentration is not high enough to lead to the formation of a diluted magnetic semiconductor.

Appendices

Appendix A

Experimental Setup

In the present thesis, different combinations of experimental equipment have been used, depending on the measurements intended to be performed.

Cryogenic control systems

Three different ranges of temperature have been investigated, requiring different instrumentation:

- The Oxford Kelvinox^{TLM} 400 dilution refrigerator. This is a top-loading system: when the sample has to be placed in, only the sample holder is taken out of the cryostat. This procedure allows to keep the mixing chamber and the still always below about 2 K. The sample, that lies at the bottom of the sample holder, is placed inside the main magnet. In this way it is possible to make measurements in the range between -18 T and $+18$ T. Depending on the kind of sample holder, the magnetic field can be applied parallel or perpendicular to the sample.
  The base temperature of this dilution refrigerator is of about 25 mK.
  The dilution refrigerator have been employed for measurements on the QD systems and on some of the InAs NW systems.

- The ^{4}He Oxford cryostat with variable temperature insert. This is a ^{4}He systems, where, via pumping, a temperature of 1.5 K can be reached and maintained. A perpendicular magnetic field between -13 T and

+13 T could be applied.
This cryostat have been employed for the preliminary measurements on Be-doped GaAs NW systems, when it was not necessary a broad temperature sweeping range.

- The helium dewar. A sample holder with basic functionalities could be inserted inside a dewar filled with ^{4}He equipped with a magnet at its bottom (B range between -4 T and $+4$ T).
The dewar was used for fast characterization of wire systems at a constant temperature of 4.2 K.

- The ^{4}He Oxford dewar. It is a ^{4}He system for which a specific sample holder have been built in order to perform measurements sweeping the temperature on a very wide range (from 300 K to 4.2 K). The sample holder consists of a tube that can be evacuated from outside: by injecting a small amount of helium gas (exchange gas) the sample holder can thermalize with its surroundings (the liquid ^{4}He at 4.2 K), while, evacuating it and switching on the heating element placed next to the sample, the inner temperature of the tube could be decoupled from that of the ^{4}He bath and therefore it could rise up to 300 K. This cryostat was equipped with a bipolar magnet that could sweep between -6 T and $+6$ T.
Most of the measurements on the Be-doped GaAs NW systems have been performed in this fridge.

Electronic setup

Since the measurements have been performed in several different laboratories, the electronic setup could vary in its components. Nevertheless, the measurement principle was always the same, and here a general idea of it is discussed, using as typical example the electronic setup utilized for the QD system investigations.
A scheme of the electronic measurement setup is shown in Fig. A.1.
A dc voltage $V_{\mathrm{sd}}^{\mathrm{dc}}$ is applied between the source and the drain leads of the sample, given by a voltage source controlled by a Digital-Analog-Converter (DAC). The voltage range of the source is between -10 V and 10 V; since a divider with a ratio 1:2500 is afterwards placed, at the sample side the voltage range is between -4 mV and 4 mV.
Using a voltage adder, an ac source-drain voltage $V_{\mathrm{sd}}^{\mathrm{ac}}$ is superimposed to the dc signal; this is taken from a function generator (Stanford Research System, model DS345) and it has an amplitude of 36 $\mathrm{mV_{p-p}}$ (i.e. $1\,\mu\mathrm{V_{rms}}$ at

the sample side) and a frequency of about 11 Hz, which is chosen to avoid an integer fraction of the power line frequency of 50 Hz. Two RC filters in series ($R = 100\,\Omega$ and $C = 4.7\,\mu F$) are placed before the adder in order to filter interfering noise signals.
After the adder, the voltage signal reaches the I-V converter. A schematic diagram of the main components of the I-V converter is shown in Fig. A.1b. With the device used here, depending on the input plug chosen, three different ways of applying a voltage between the source and the drain lead are possible:

- applying an equal voltage to both the source and the drain leads at the same time (COM-input),
- acting only on the source or on the drain side (SOURCE- or DRAIN-input), and
- applying a voltage to one lead and at the same time an opposite voltage to the other lead (DIFF-input).

Similarly, for the I-V output one can choose between SOURCE-, DRAIN- or SUM-output.
On the output of the I-V converter a voltmeter (Keithley 2000) is used to measure the dc source-drain current I_{sd}^{dc}. At the same time, using a lock-in amplifier (EG&G Princeton Applied Research, model 5210), the modulated ac source-drain current amplitude I_{sd}^{ac} is also detected, where the reference signal for the lock-in is taken from the function generator.
Finally, the gate electrode voltages V_{gi} are provided (as in the source-drain

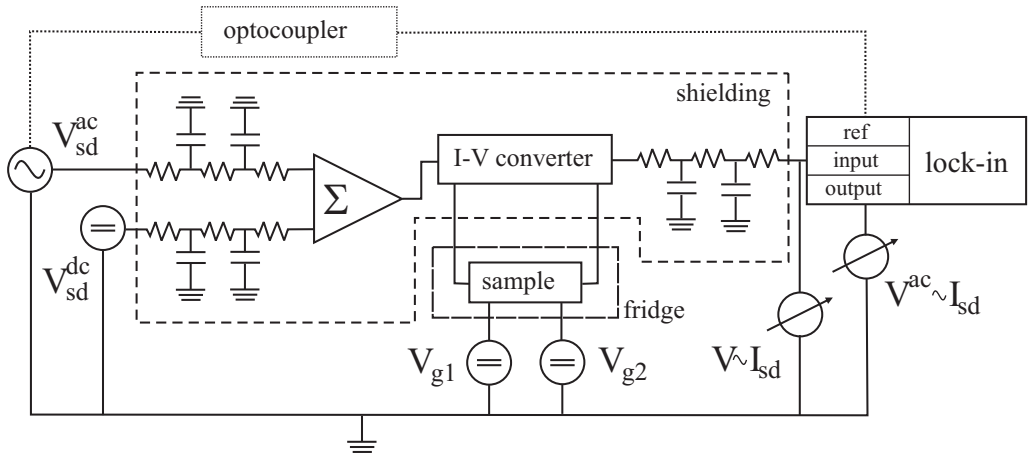

Figure A.1: *Schematic diagram of the measurement setup*

case) by a voltage source controlled by a DAC. All the electrode voltages are referred to ground.
In order to prevent ground loops, all the measurements devices are isolated from the mains supply using separated transformers. The reference ground of the instruments is given by the ground of the cryostat. In the circuit of the electronic setup, an optocoupler is also present between the function generator and the reference input of the lock-in in order to prevent a loop.

Temperature controllers

Two different temperature controllers have been used for the temperature dependence measurements, the *Cryocon 32* and the *Lakeshore 340*.

Appendix B

Additional measurements of charge stability diagrams on the quantum dot system

In this Appendix, some additional measurements performed on the quantum dot system discussed in Part I and characterized in Fig. 2.2a and Fig. 2.7 are shown, to emphasize the rich variety of internal electron configuration that can be found by tuning either the magnetic field or the coupling strength between the island and its leads.

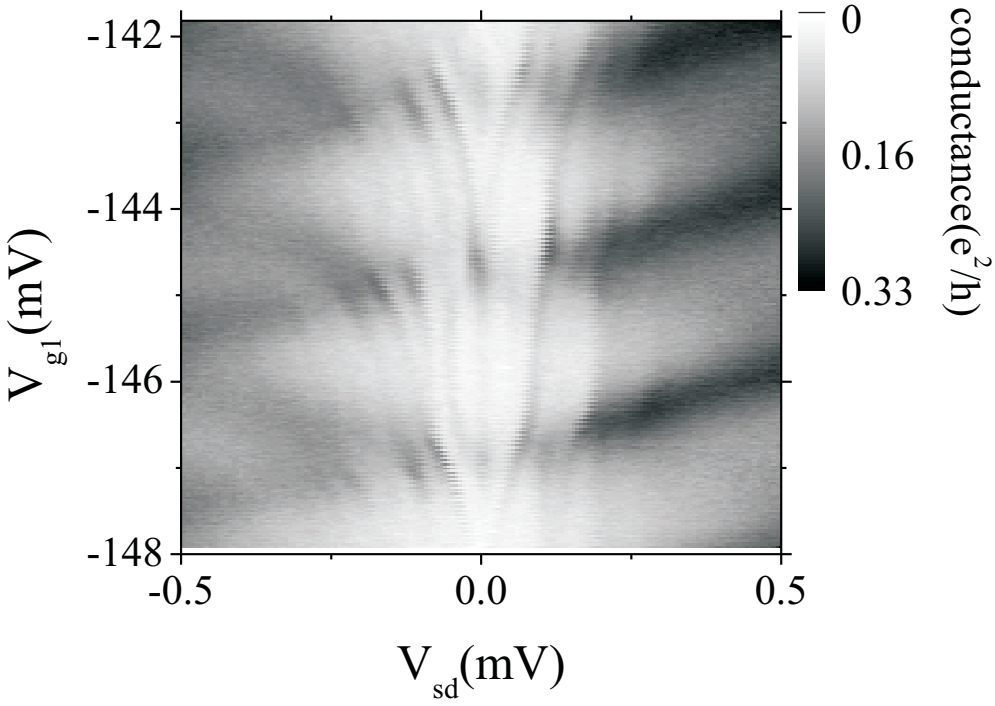

Figure B.1: Differential conductance measured on the grey scale as a function of the source-drain and of the gates voltages for a weak coupling regime.

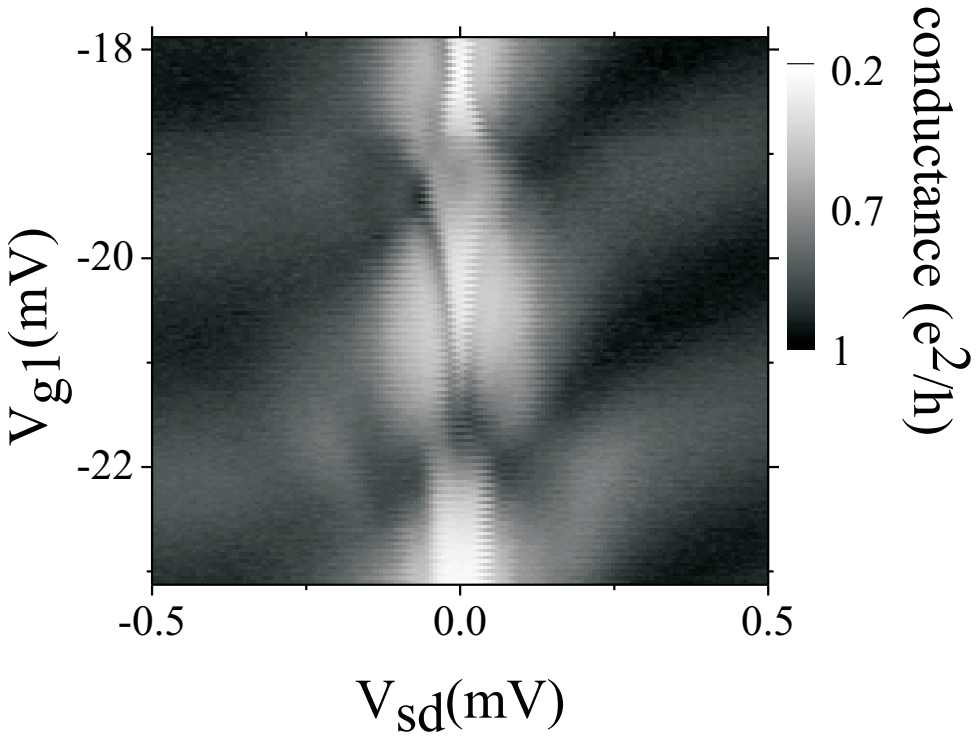

Figure B.2: Differential conductance measured on the grey scale as a function of the source-drain and of the gates voltages for an intermediate coupling regime.

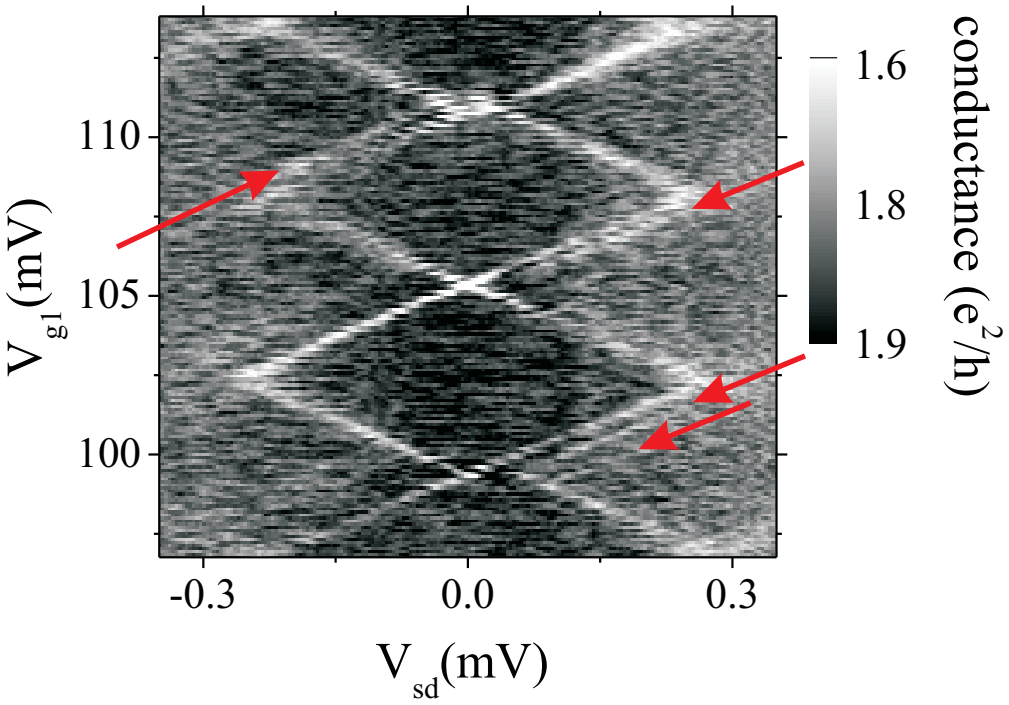

Figure B.3: Differential conductance measured on the grey scale as a function of the source-drain and of the gates voltages for a strong coupling regime. The red arrows indicate sharp minima located parallel to the borderlines of this diamond-shaped regions, in a fashion that resembles the conductance peaks due to transport via excited states for a weak coupling regimes.

Appendix C

Contacting process for the nanowire systems

In this Appendix the detailed recipe for the nanowire samples preparation will be given.

1- **The Molecular Beam Epitaxy growth** via Vapor-Liquid-Solid technique has been carried out by the group of Silvia Rubini at the Laboratorio Nazionale TASC-INFM-CNR in Trieste (Italy) and details of this part of the process can be found in [47], [48], and [49].

2- **Deposition of the wires on the SiO_2 substrate**:
Preparation of the substrate: Since on the substrate markers have been previously defined via e-beam processing, they are coated by some residual resist that has to be firstly removed:

- 10 min to 15 min in a N-Methyl-2-pyrrolidone (NMP) bath at 55° C with ultrasounds,
- 10 min to 15 min in an acetone bath at 55° C with ultrasounds, and
- 10 min to 15 min in an isopropanol bath at 55° C with ultrasounds.
- Blow dry.

Lay the substrate on a tissue and gently place the nanowire chip on it pushing very slightly with cleanroom tweezers. Check at the optical microscope (dark field helps) to have obtained a reasonable distribution of nanowires on the substrate, a few to several nanowires per marker field.

3- **Location of the wires** with respect to the markers by using Atomic Force Microscope or Scanning Electron Microscope (for an example of a typical markers field, see Fig. C.1).

4- **Resist coating**: two different layers of polymethylmetacrylat (PMMA) resist were employed to obtain an undercut during the development step and therefore have an easier lift-off of the deposited metal at the end. While the thickness of the top layer remained unchanged for all the samples, that of the bottom layer was chosen depending on the thickness of the specific wire to contact and it was then calibrated every single time.

   - Bottom layer: For wires with diameter thinner than 60 nm, two droplets of PMMA 200k 3.5% (e-beam resist AR-P641.07 thinned to 3.5% solid contents using chlorobenzene as solvent). For thicker wires, 200k 3.5% (e-beam resist AR-P641.07 thinned to 7% solid contents using chlorobenzene as solvent).
   - Bake the resist for 10 minutes on the hot plate at 160° C.
   - Let the sample to cool down for at least 10 minutes.
   - Top layer: two droplets of PMMA 950k 1.5% (e-beam resist AR-P671 thinned to 1.5% solid contents using chlorobenzene as solvent).
   - Bake the resist for 10 minutes on the hot plate at 160° C.

5- **E-beam exposure** with eLine system (Raith), software version 4.0:

   - Acceleration voltage: 20 kV.
   - Aperture: 10 μm.
   - Working distance: 7.
   - z-position of the stage: 28 mm.
   - Detector: inLens.
   - Current: $\approx$ 0.045 nA.
   - Dose: 310 μC/m^2, or, for structures smaller than 100 nm, 330 μC/m^2.

- Basic step size: 2 nm.
- Area step size: 4 nm.

After unloading the samples from the eLine, the exposed resist is developed dipping for 1 min and 45 s in MIBK and rinsing afterwards in isopropanol for 1 min.

6- **Etching**: the removal of the PMMA resist residuals and the oxide covering the nanowires is a very critical step and several procedures have been tried. Finally, two procedures have been selected as equally effective and reliable:

- O_2 plasma to remove the PMMA residuals: $t = 10$ s, $p = 0.3$ Torr, and $P = 200$ W.
- Buffered HF to remove the oxide: dipping in bHF between 6 s and 10 s, or dipping for 10 seconds in a solution of 49% HF and deionized water, with a proportion 1:100.
- Rinsing in deionized water.

7- **Evaporation of the contacts**: depending on the sample, different metal combinations have been used:

- 10 nm Ti at a rate of of 4 Å/s, followed by 70 nm Al at a rate of 2 Å/s,
- 10 nm Cr at a rate of 2 Å/s, followed by 70 nm Au at a rate of 2 Å/s,
- 10 nm Cr at a rate of 1.5 to 2 Å/s, followed by 100 nm Au at a rate of 2 Å/s, or
- 110 nm Nickel at a rate of 2 Å/s.

8- **Lift-off** to remove the metal covering the undeveloped resist:

- 2 hours in NMP at 55° C with no ultrasounds,
- 2 minutes splashing with acetone,
- rinsing with isopropanol, and
- blow dry.

9- The chips with the finished samples are at end glued on a chip carrier using silver paint (so to access the backgate during measurements) and then wire bonded to the carrier using 17.5 μm gold wire.

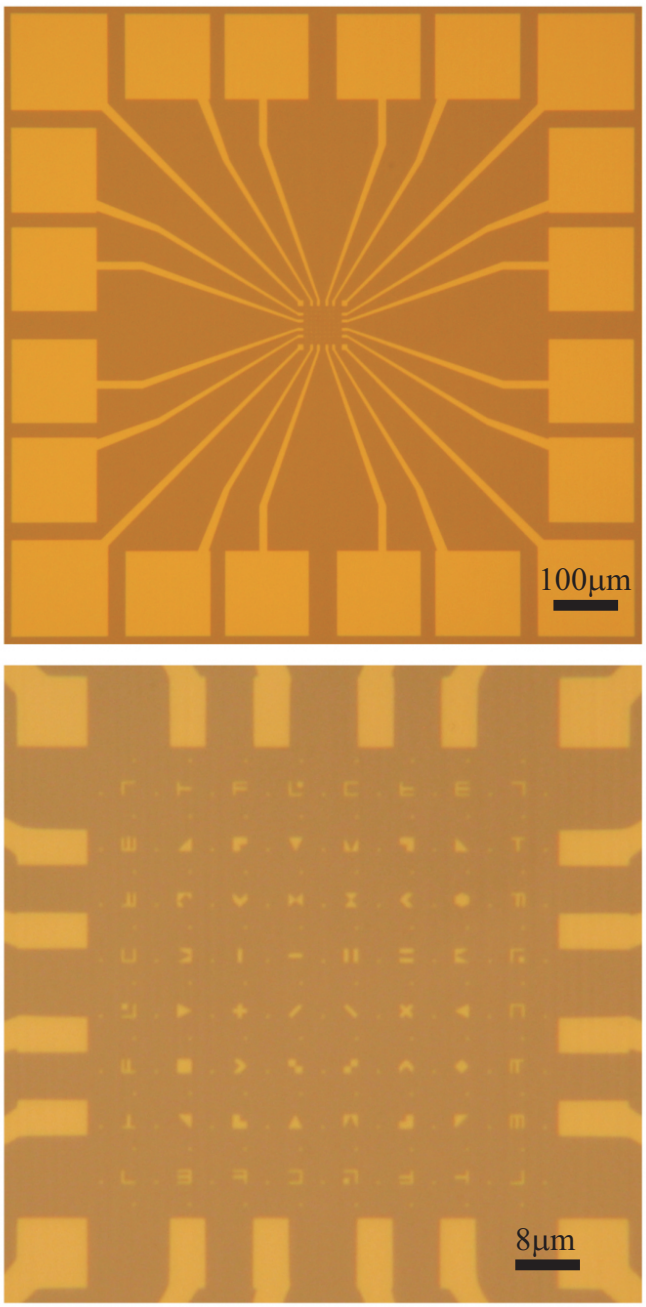

Figure C.1: Images from the optical microscope of a typical SiO_2 substrate with markers: on top, the outer bonding pads, and, at the bottom, a zoom in of the markers filed.

Appendix D

Additional measurements on Au-GaAs nanowire systems

In this Appendix, some additional measurements on Au induced Be doped GaAs nanowire systems are shown, to report the case for which transport become localized at low temperature. The values of the four-terminal resistance increases considerably during the cooling down process and, when sweeping the voltage applied to the backgate, Coulomb Blockade Oscillations arise from the measured current.

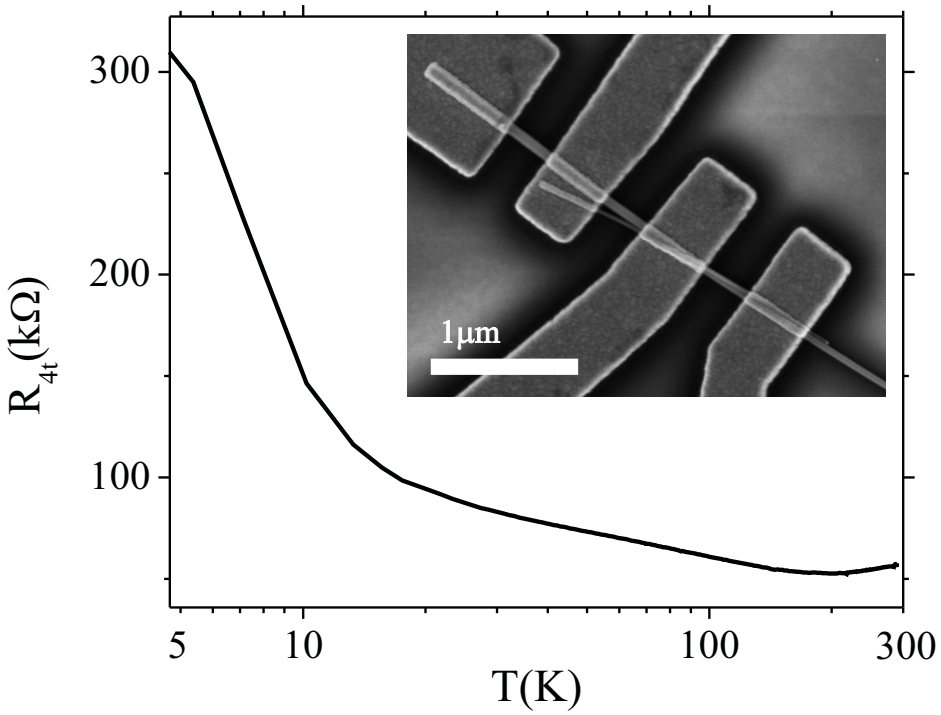

Figure D.1: Four-terminal resistance for a Be doped Au-GaAs NW system with Cr/Au contacts, plotted as a function of temperature. In the inset, Scanning Electron Microscope image of the measured system in a four-terminal configuration.

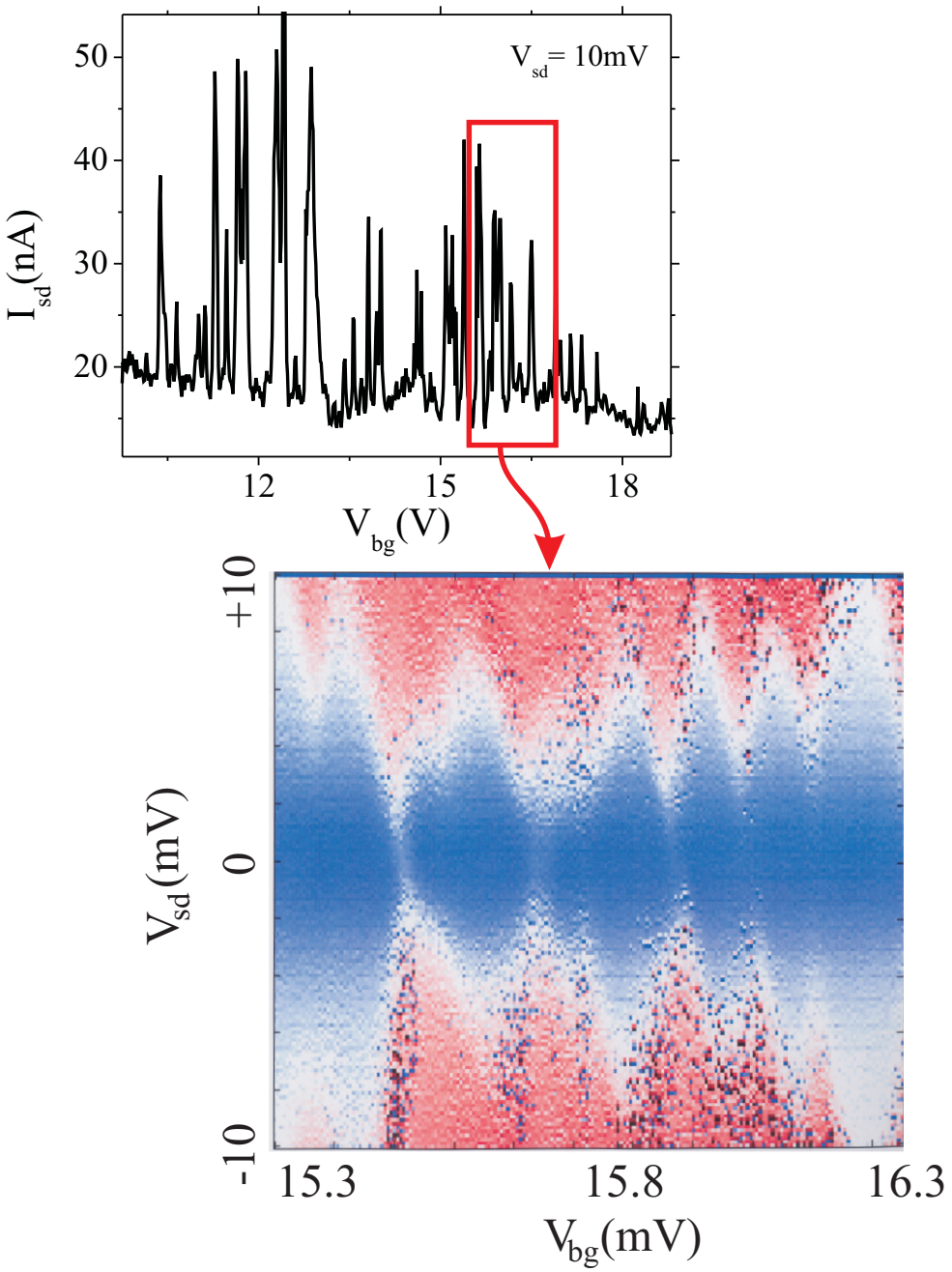

Figure D.2: Top: Current through the NW system of Fig. D.1 as a function of the voltage applied to the backgate: transport is characterized by Coulomb Blockade Oscillations. Bottom: Charge stability diagram referring to the CBOs trace enclosed in the box in the upper plot.

Bibliography

[1] M. Keller. *Der Kondo-Effekt in Quantendots bei hohen Magnetfeldern.* PhD thesis, Universität Stuttgart, Germany, 2001.

[2] K. v. Klitzing, G. Dorda, and M. Pepper. New Method for High-Accuracy Determination of the Fine-Structure Constant Based on Quantized Hall Resistance. *Phys. Rev. Lett.*, 45:494, 1980.

[3] K. v. Klitzing. The Quantized Hall Effect. In *Nobel Lectures, Physics 1981-1990.* Gösta Ekspong (World Scientific, Singapore, 1993).

[4] J. D. Schmid. *The Kondo Effect in Quantum Dots.* PhD thesis, Universität Stuttgart, Germany, 2000.

[5] A. Lorke, R. J. Luyken, A. O. Govorov, and J. P. Kotthaus. Spectroscopy of nanoscopic semiconductor rings. *Phys. Rev. Lett.*, 84:2223, 2000.

[6] S. J. Tans, M. H. Devoret, R. J. A. Groeneveld, and C. Dekker. Electron-electron correlations in carbon nanotubes. *Nature*, 394:761, 1998.

[7] L.P. Kouwenhoven, D. G. Austing, and S. Tarucha. Few-electron quantum dots. *Rep. Prog. Phys.*, 64:701, 2001.

[8] M. Ciorga, A. S. Sachrajda, P. Hawrylak, C. Gould, P. Zawadski, S. Julian, Y. Feng, and Z. Wasilewski. Addition spectrum of a lateral dot from Coulomb and spin-blockade spectroscopy. *Phys. Rev. B*, 61:16315, 2000.

[9] S. Datta. *Electronic transport in mesoscopic systems.* Cambridge University Press, 1995.

[10] C. W. J. Beenakker. Influence of Coulomb repulsion on the Aharanov-Bohm effect in a quantum dot. *Phys. Rev. B*, 44(4):1657, 1991.

[11] J. Weis. *Electrical Transport Through Quantum Dot Systems*. Habilitationsschrift, Universität Stuttgart, Germany, 2002.

[12] U. Wilhelm. *Präparation und elektrische Charakterisierung elektrostatisch gekoppelter Quantendotsysteme; eine Realisierung des Anderson-Störstellenmodells*. PhD thesis, Universität Stuttgart, Germany, 2000.

[13] De Franceschi S., and Sasaki, S. and Elzerman, J. M. and van der Wiel, W. G. and Tarucha, S. and Kouwenhoven, L. P. Electron Cotunneling in a Semiconductor Quantum Dot. *Phys. Rev. Lett.*, 86:878, 2001.

[14] W. G. van der Wiel, S. De Franceschi, T. Fujisawa, J. M. Elzerman, S. Tarucha, and L. P. Kouvenhoven. The Kondo effect in the unitary limit. *Science*, 289:2105, 2000.

[15] D. Goldhaber-Gordon, H. Shtrikman, D. Mahalu, D. Abush-Mahder, U. Meirav, and M. A. Kastner. Kondo effect in a single-electron transistor. *Nature*, 391:156, 1998.

[16] Anderson, P. W. Localized Magnetic States in Metals. *Phys. Rev.*, 124:41, 1961.

[17] Göres, J. and Goldhaber-Gordon, D. and Heemeyer, S. and Kastner, M. A. and Shtrikman, H. and Mahalu, D. and Meirav, U. Fano resonances in elecronic transport through a single-electron transistor. *Phys. Rev. B*, 62:2188, 2000.

[18] U. Fano. Effects of Configuration Interaction on Intensities and Phase Shifts. *Phys. Rev.*, 124:1866, 1961.

[19] K. Kobayashi, H. Aikawa, S. Katsumoto, and Y. Iye. Tuning the Fano Effect through a Quantum Dot in an Aharonov-Bohm Interferometer. *Phys. Rev. Lett.*, 88:256806, 2002.

[20] M. Sato, H. Aikawa, K. Kobayashi, S. Katsumoto, and Y. Iye. Observation of the Fano-Kondo Antiresonace in a Quantum Wire with a Side-Coupled Quantum Dot. *Phys. Rev. Lett.*, 95:066801, 2005.

[21] V. Fock. Bemerkung zur Quantelung des harmonischen Oszillators in Magnetfeld. *Z. Phys.*, 47:446, 1928.

[22] C. G. Darwin. The Diamagnetism of the Free Electron. *Proc. Cambridge Philos. Soc.*, 27:86, 1930.

[23] P. L. McEuen, E. B. Foxman, J. Kinaret, U. Meirav, M. A. Kastner, N. S. Wingreen, and S. J. Wind. Self-consistent addition spectrum of a Coulomb island in the quantum Hall regime. *Phys. Rev. B*, 45:11419, 1992.

[24] D. B. Chklovskii, B. I. Shklovskii, and L. I. Glazman. Electrostatics of edge channels. *Phys. Rev. B*, 46:4026, 1992.

[25] K. Lier and R. R. Gerhardts. Self-consistent calculations of edge channels in laterally confined two-dimensional electron system. *Phys. Rev. B*, 50(11):7757, 1994.

[26] J. Weis, Y. Y. Wei, and K. v. Klitzing. Single-electron transistor probes two-dimensional electron system in high magnetic fields. *Physica E*, 3:23–29, 1998.

[27] Heinzel, T. and Wharam, D. A. and Kotthaus, J. P. and Böhm, G. and Klein, W. and Tränkle, G. and Weiman, G. Periodic modulation of Coulomb-blockade oscillations in high magnetic fields. *Phys. Rev. B*, 50:15113, 1994.

[28] A. A. M. Staring, B. W. Alphenaar, H. van Houten, L. W. Molenkamp, O. J. A. Buyk, M. A. A. Mabesoone, and C. T. Foxon. Periodic envelope of Coulomb-blockade oscillations in the quantum Hall regime. *Phys. Rev. B*, 46:12869, 1992.

[29] J. Hüls, J. Weis, J. Smet, K. v. Klitzing, and Z. R. Wasilewski. Long time relaxation phenomena of a two-dimensional electron system within integer quantum Hall plateau regimes after magnetic field sweeps. *Phys. Rev. B*, 69:085319–1, 2004.

[30] M. Kataoka, C. J. B. Ford, M. Y. Simmons, and D. A. Ritchie. Selective spin-resolved edge-current injection into a quantum antidot. *Physica E*, 22:168, 2004.

[31] M. Kataoka, C. J. B. Ford, M. Y. Simmons, and D. A. Ritchie. Kondo effect in a Quantum Antidot. *Phys. Rev. Lett.*, 89:226803–1, 2002.

[32] J. H. Davies. *The physics of low-dimensional semiconductors: an introduction*. Cambridge University Press, 1998.

[33] P. Weitz. *Untersuchungen zum Verlauf der Hall-Spannung in einem zweidimensionalen Elektronensystem unter den Bedingungen des Quanten-Hall-Effekts mittels eines Raster-Kraft-Mikroskops*. PhD thesis, Universität Hamburg, Germany, 1999.

[34] E. Ahlswede. *Potential- und Stromverteilung beim Quanten-Hall-Effekt bestimmt mittels Rasterkraftmikroskopie*. PhD thesis, Universität Stuttgart, Germany, 2002.

[35] F. Dahlem. *Adiabatic transport in the quantum Hall regime: Comparison between transport and scanning force microscopy investigations*. PhD thesis, Universität Stuttgart, Germany, 2008.

[36] B. J. van Wees, L. P. Kouwenhovem, J. P. M. Harmans, J. G. Williamson, C. E. Timmering, M. E. I. Broekaart, C. T. Foxon, and J. J. Harris. Observation of Zero-Dimensional States in a One-Dimensional Electron Interferometer. *Phys. Rev. Lett.*, 62:2523, 1989.

[37] P. L. McEuen, E. B. Foxman, U. Meirav, M. A. Kastner, Yigal Meir, Ned S. Wingreen, and S. J. Wind. Transport Spectroscopy of a Coulomb Island in the Quantum Hall Regime. *Phys. Rev. Lett.*, 66:1926, 1991.

[38] A. T. Johnson, L. P. Kouwenhovem, W. de Jong, N. C. van der Vaart, C. J. P. M. Harmans, and C. T. Foxon. Zero-Dimensional States and Single Electron Charging in Quantum Dots. *Phys. Rev. Lett.*, 69:1592, 1992.

[39] B. W. Alphenaar, A. A. M. Staring, H van Houten, M. A. A. Mabesoone, O. J. A. Buyk, and C. T. Foxon. Influence of adiabatically transmitted edge channels on single-electron tunneling through a quantum dot. *Phys. Rev. B*, 46:7236, 1992.

[40] T. Heinzel, A. T. Johnson, D. A. Wharam, J. P. Kotthaus, G. Böhm, W. Klein, G. Tränkle, and G. Weimann. Coulomb-blockade oscillations in a quantum dot strongly coupled to leads. *Phys. Rev. B*, 52:16638, 1995.

[41] M. Keller. Quantum dot in high magnetic fields: Correlated tunnelling of electrons probes the spin configuration at the edge of the dot. *Phys. Rev. B*, 64:033302, 2001.

[42] R. S. Wagner and W. C. Ellis. Vapor-liquid.solid mechanism of single crystal growth. *Appl. Phys. Lett.*, 4:89, 1964.

[43] J. Johansson, B. A. Wacaser, K. A. Dick, and W. Seifert. Growth related aspects of epitaxial nanowires. *Nanotechnology*, 17:S355, 2006.

[44] M. Law, J. Goldberger, and P. Yang. Semiconductir Nanowires and Nanotubes. *Annu. Rev. Mater. Res.*, 34:83, 2004.

[45] W. Lu and C. M. Lieber. Semiconductor nanowires. *J. Phys. D: Appl. Phys.*, 39:R387, 2006.

[46] Seifert, W. and Borgström, M. and Deppert, K. and Dick, K. A. and Johansson, J. and Larsson, M. W. and Mårtensson, T. and Sköld, N. and Svensson, C. P. T. and Wacaser, B. A. and Wallenberg, L. R. and Samuelson, L. Growth of one-dimensional nanostructures in MOVPE. *J. Cryst. Growth*, 272:211, 2004.

[47] F. Martelli, S. Rubini, M. Piccin, G. Bais, F. Jabeen, S. De Franceschi, V. Grillo, E. Carlino, F. D'Acapito, F. Boscherini, S. Cabrini, M. Lazzarino, L. Businaro, F. Romanato, and A. Franciosi. Manganese-Induced Growth of GaAs Nanowires. *Nano Lett.*, 6:2130, 2006.

[48] M. Piccin, G. Bais, V. Grillo, F. Jabeen, S. De Franceschi, E. Carlino, M. Lazzarino, F. Romanato, L. Businaro, S. Rubini, F. Martelli, and A. Franciosi. Growth by molecular beam epitaxy and electrical characterization of GaAs nanowires. *Physica E*, 37:134, 2007.

[49] Begum, N. and Piccin, M. and Jabeen, F. and Bais, G. and Rubini, S. and Martelli, F. and Bhatti, A. S. Structural characterization of GaAs and InAs nanowires by means of Raman spectroscopy. *J. Appl. Phys.*, 104:104311, 2008.

[50] Björk, M. T. and Ohlsson, B. J. and Sass, T. and Persson, A. I. and Thelander, C. and Magnusson, M. H. and Deppert, K. and Wallenberg, L. R. and Samuelson, L. One-dimensional heterostructures in semiconductor nanowhiskers. *App. Phys. Lett.*, 80:1058, 2002.

[51] De Franceschi, S. and van Dam, J. A. and Bakkers, E. P. A. M. and Feiner, L. F. and Gurevich, L. and Kouwenhoven, L. P. Single-electron tunneling in InP nanowires. *App. Phys. Lett.*, 83:344, 2003.

[52] Ohlsson, B.J. and Björk, M.T.and Persson, A.I. and Thelander, C. and Wallenberg, L.R. and Magnusson, M.H. and Deppert, K. and Samuelson, L. Growth and characterization ofGaAs and InAs nano-whiskers and InAs=GaAs heterostructures. *Physica E*, 13:1126, 2002.

[53] Samuelson, L. and Thelander, C. and Björk, M. T. and Borgström, M. and Deppert, K. and Dick, K. A. and Hansen, A. E. and Mårtensson, T. and Panev, N. and Persson, A. I. and Seifert, W. and Sköld, N. and Larsson, M. W. and Wallenberg, L. R. Semiconductor nanowires for 0D and 1D physics and applications. *Physica E*, 25:313, 2004.

[54] Shorubalko, I. and Pfund, A. and Leturcq, R. and Borgström, M. T. and Gramm, F. and Müller, E. and Gini, E. and Ensslin, K. Tunable few-electron quantum dots in InAs nanowires. *Nanotechnology*, 18:044014, 2007.

[55] C. Fasth, A. Fuhrer, L. Samuelson, V. N. Golovach, and D. Loss. Direct Measurement of the Spin-Orbit Interaction in a Two-Electron InAs Nanowire Quantum Dot. *Phys. Rev. Lett.*, 98:266801, 2007.

[56] Žutić, I. and Fabian, J. and Das Sarma, S. Spintronic: Fundamentals and applications. *Rev. Mod. Phys.*, page 323, 2004.

[57] Field, M. and Smith, C. G. and Pepper, M. and Ritchie, D. A. and Frost, J. E. F. and Jones, G. A. C. and Hasko, D. G. Measurements of Coulomb BLockade with a Noninvasive Voltage Probe. *Phys. Rev. Lett.*, 70:1311, 1993.

[58] Hu, Y. and Churchill, H. O. H. and Reilly, D. J. and Xiang, J. and Lieber, C. M. anf Marcus, C. M. A Ge/Si heterostructure nanowire-based double quantum dot with integrated charge sensor. *Nature Nanotech.*, 2:622, 2007.

[59] Story, T. and Gałązka, R. R. and Frankel, R. B. and Wolff, P. A. Carrier-concentration induced ferromagnetism in PbSnMnTe. *Phys. Rev. Lett.*, 56:777, 1986.

[60] H. Ohno, H. Munekata, T. Penney, S. von Molnár, and L. L. Chang. Magnetotransport Properties of p-type (In,Mn)As Diluted Magnetic III-V Semiconductors. *Phys. Rev. Lett.*, 68:2664, 1992.

[61] F. Matsukura, H. Ohno, A. Shen, and Y. Sugawara. Transport properties and origin of ferromagnetism in (Ga,Mn)As. *Phys. Rev. B*, 57:R2037, 1998.

[62] A. H. MacDonald, P. Schffer, and N. Samarth. Ferromagnetic semiconductors: moving beyond (Ga,Mn)As. *Nature Materials*, 4:195, 2005.

[63] T. Jungwirth, J. Sinora, J. Masek, J. Kucera, and A. H. MacDonald. Theory of ferromagnetic (III,Mn)V semiconductors. *Rev. Mod. Phys.*, 78:809, 2006.

[64] Frustaglia, D. and König, J. and MacDonald, A. H. Theory of spin waves in diluted-magnetic-semiconductor quantum wells. *Phys. Rev. B*, 70:045205, 2004.

[65] Chiba, D. and Yamanouchi, M. and Matsukura, F. and Ohno, H. Electrical Manipulation of Magnetization Reversal in a Ferromagnetic Semiconductor. *Science*, 301:943, 2003.

[66] Weisheit, M. and Fähler, S. and Marty, A. Souche, Y. and Poinsignon, C. and Givord, D. Electric Field-Induced Modification of Magnetism in Thin-Film Ferromagnets. *Science*, 315:349, 2007.

[67] Capotondi, F. privat comunication.

[68] S. M. Sze. *Semiconductor Devices, Physics and Technology*. John Wiley & Sons, New York, 1979.

[69] N.W. Ashcroft and N.D. Mermin. *Solid State Physiscs*. Saunders College Publishers, 1976.

[70] Fal'ko, V. privat comunication.

[71] M. Cardona and P. Y. Yu. *Fundamentals of Semiconductors*. Springer, 1999.

[72] R. Winkler. *Spin-Orbit Coupling Effects in Two-Dimensional Electron and Hole systems*. Springer-Verlag, Berlin, 2003.

[73] Grbiċ, B. and Leturcq, R. and Ihn, T. and Ensslin, K. and Reuter, D. and Wieck, A. Strong spin-orbit interaction and weak anti-localization in carbon-doped p-type GaAs/Al_xGa_{1-x}As heterostructures. *Phys. Rev. B*, 77:125312, 2008.

[74] Meyer, J. S. and Fal'ko, V. and Altshuler, B. L. Quantum in-plane magnetoresistance in 2D electron systems. *Cond-mat.mes-hall*, page 0206024v1, 2002.

[75] Kurdak, Ç. and Chang, A. M. and Chin, A. and Chang, T. Y. Quantum interference effects and spin-orbit interaction in quasi-one-dimensional wires and rings. *Phys. Rev. B*, 46:6846, 1992.

[76] Wirthmann, A. and Gui, Y. S. and Zehnder, C. and Heitmann, D. and Hu, C.-M. and Kettemann, S. Weak antilocalization in InAs quantum wires. *Physica E*, 34:493, 2006.

[77] Kettemann, S. Dimensional Control of Antilocalization and Spin Relaxation in QuantumWires. *Phys. Rev. Lett.*, 98:176808, 2007.

Acknowledgments

I would like to take the opportunity here to thank all the people that made this work possible:

Klaus von Klitzing, who offered me the possibility to carry out my PhD within his group, providing a superb scientific infrastructure for all of us;

Jürgen Weis, who first introduced me into the mesoscopic physics topic during my university times and that followed my advancements till here;

Silvano De Franceschi, who gave me the possibility to follow my interest in the nanowire systems, and let me carry the concluding measurements within his group at the CEA facility;

Silvia Rubini and her group at the TASC National Lab, who grew all my nanowires and answered to all my questions as an outsider;

Alex Hübel and Armin Welker, who suffered together with me when dealing with all the measkern problems and with the running of the dilution refrigerator;

Jochen Weber, who spent many hours looking at my broken samples at the Cross Beam;

Johannes Nübler, who helped me with the German text;

Monika Riek, who taught me how to deal with many of the machines in the cleanroom and who was always there to help me;

(in random order) Serhat Sahakalkan, Viktor Siegle, Thomas Weitz, Cristina Gomez-Navarro, and many others, who took the time to teach me how to process nanowire systems and always answered to all my questions. They also provided all the substrates that I used in my samples preparation;

Giorgos Katsaros and Panayotis Spathis, my priceless lab-mates in Grenoble, who took the concept of "team work" to remarkable levels;

(in alphabetical order) Franck Dahlem, Dimitri Dini, Oktay Göktaş, Nebile Isik, Myrsini Lafkioti, Denis Maryenko, Frank Ospald, and Afif Siddiki, for a friendship that goes far beyond all our countless discussions about physics;

Mark Lynass, my amicable number, for his constant support, for being my first reference in all the MBE related issues and for proof-reading this thesis;

my parents, for far too many reasons.

Curriculum Vitae

Name	Eleonora Storace
Place, date of birth	Udine (Italy), April 1st, 1979
Nationality	Italian
Address	MPI for Solid State Research
	Heisenbergstr. 1, D-70569 Stuttgart
	Tel.: +49 (0)711 6891545
	Fax: +49 (0)711 6891572
	E-mail: `e.storace@fkf.mpg.de`

Education

November 2004
- present — Ph.D. student in Physics
Max Planck Institute for Solid State Research, Stuttgart
in the Department of Prof. Dr. K. von Klitzing

August 2003
- October 2004 — Tesi di Laurea (M.S.) in Physics
Università degli Studi dell'Insubria (Como, Italy)
Thesis: *Electrical transport through a quantum dot system at high magnetic fields*
Supervisor: Prof. Giancarlo Jug
Co-supervisor: Prof. Alessandro Sottocornola Spinelli
c/o: Max Planck Institute for Solid State Research,
Department of Prof. Dr. K. von Klitzing

November 1998
- October 2004 — Corso di Laurea in Fisica
Università degli Studi dell'Insubria (Como, Italy)
Facoltà di Scienze Chimiche, Fisiche e Matematiche
Fisica della Materia

July 1998 — Diploma di maturità classica
Liceo Ginnasio Statale *A. Volta* (Como, Italy)

Hiermit erkläre ich, dass ich diese Arbeit selbständig verfasst und keine anderen als die im Text angegebenen Hilfsmittel verwendet habe. Die Personen, von denen ich Ratschläge erhalten habe, sind in der Danksagung auf der nächsten Seite namentlich aufgeführt.